UNDERSTANDING MATERIALS BEHAVIOR FROM ATOMISTIC SIMULATIONS: CASE STUDY OF Al-CONTAINING HIGH ENTROPY ALLOYS AND THERMALLY GROWN ALUMINUM OXIDE

by

Yinkai Lei

Submitted to the Graduate Faculty of
the Swanson School of Engineering in partial fulfillment
of the requirements for the degree of
Doctor of Philosophy

University of Pittsburgh

2015

UNIVERSITY OF PITTSBURGH

SWANSON SCHOOL OF ENGINEERING

This dissertation was presented

by

Yinkai Lei

It was defended on

October 1, 2015

and approved by

Guofeng Wang, Ph.D., Associate Professor, Department of Mechanical Engineering and Materials Science

Brian M. Gleeson, Ph.D., Harry S. Track Chair Professor and Department Chair, Department of Mechanical Engineering and Materials Science

Jörg M. K. Wiezorek, Ph.D., Professor, Department of Mechanical Engineering and Materials Science

Scott X. Mao, Ph.D., Professor, Department of Mechanical Engineering and Materials Science

John A. Keith, Ph.D., Assistant Professor, Department of Chemical and Petroleum Engineering

Dissertation Director: **Guofeng Wang**, Ph.D., Associate Professor, Department of Mechanical Engineering and Materials Science

UNDERSTANDING MATERIALS BEHAVIOR FROM ATOMISTIC SIMULATIONS: CASE STUDY OF Al-CONTAINING HIGH ENTROPY ALLOYS AND THERMALLY GROWN ALUMINUM OXIDE

Yinkai Lei, PhD

University of Pittsburgh, 2015

Atomistic simulation refers to a set of simulation methods that model the materials on the atomistic scale. These simulation methods are faster and cheaper alternative approaches to investigate thermodynamics and kinetics of materials compared to experiments. In this dissertation, atomistic simulation methods have been used to study the thermodynamic and kinetic properties of two material systems, *i.e.* the entropy of Al-containing high entropy alloys (HEAs) and the vacancy migration energy of thermally grown aluminum oxide.

In the first case study of the dissertation, a computational scheme for evaluating the entropy of HEAs has been developed. Entropy is a key factor for the phase stability of HEAs. However, it has not been well understood yet. In this study, atomistic simulation methods have been used to quantify the configurational and vibrational entropy of HEAs for the first time. Modified embedded atom method was used to describe the interatomic interactions in HEAs. Monte Carlo simulation and thermodynamic integration method were used to calculate the thermodynamic properties such as entropy and free energy. This scheme has been tested on Al_xCoCrFeNi HEAs. The results show that a reasonable evaluation of the entropy of Al_xCoCrFeNi HEAs can be obtained by the developed scheme. The FCC to BCC phase transition in this alloy system has also been captured by the calculated free energy. Importantly, it is found that atomic vibrations have an important effect on the quantitative prediction of the compositional boundary of the FCC-BCC duplex region in the Al_xCoCrFeNi HEA system. The calculated entropy has been validated by comparing the atomic ordering in the simulated HEAs to the HEAs in experiments. The good agreement between the simulations and experiments indicates that the developed computational scheme captured the non-ideality in HEAs which is the key to understand the entropy of HEAs.

In the second case study of this dissertation, the charge effect on the vacancy diffusion in α-Al_2O_3 has been investigated. It has been known that the charge state has an effect on the formation energy of vacancies. However, the relation between the charge state and the migration energy of vacancies is unknown yet. In this study, density functional theory calculations have been used to investigate the charge effect on the vacancy migration energy. It is found that the vacancy migration energy depends strongly on the charge state of the vacancy. This dependency is explained by the shift of the defect levels associated with the vacancy and the electron occupancy on the defect levels. These findings for the first time built a link between the electronic structure and the migration of vacancy in metal oxides. This information indicates a novel approach to tune the diffusion kinetics by modifying the electronic structure of metal oxides.

Keywords: atomistic simulations, Monte Carlo, density functional theory, modified embedded atom method, thermodynamic integration, high entropy alloy, configurational entropy, vibrational entropy, α-Al_2O_3, vacancy migration energy, charge effect, defet level.

TABLE OF CONTENTS

LIST OF TABLES

LIST OF FIGURES

1.0 OVERVIEW

The ultimate goal of materials science is to develop materials that satisfy the needs of people. By controlling the chemical composition, crystal structure and microstructure of materials, material scientists produce materials with all kinds of properties. The thermodynamics and kinetics of materials are the two most important factors which tells us how to realize desirable compositions and structures of materials during processing. The former determines the processing conditions, while the latter determines the time table of processing. Traditionally, the thermodynamics and kinetics of materials are investigated by extensive experiments, which are usually time-consuming and costly. The fast development of computational materials science in the past two decades, however, provides us a faster and cheaper approach to explore the thermodynamics and kinetics of materials. In this dissertation, atomistic simulation methods have been used to investigate the thermodynamic and kinetic properties of materials. Two different material systems, *i.e.* high-entropy alloy (HEA) and aluminum oxide, were investigated separately. This chapter begins with a brief introduction of the research problems in these two case studies. Then the hypotheses, objectives and significances of these two case studies have been discussed.

1.1 INTRODUCTION

This dissertation is composed of two case studies, each one focusing on applying atomistic simulation methods to explore certain properties of a material system. The subject of the first case study is the entropy of HEAs. High entropy alloys (HEAs, also known as multi-principle element or compositionally complex alloys) refer to single phase alloys with five or more principle elements in equiatomic or near-equiatomic ratios [1]. The solid solution phase has been stabilized by the large mixing entropy of HEAs [2]. However, the only current model to calculate the mixing entropy of HEAs is the model of ideal solutions. This model is successful in predicting the mixing entropy of dilute solutions, but it fails for HEAs at near-equiatomic concentrations due to the complex interactions between different components. It has already been found that the model of ideal solutions overestimated the stability of the solid solution phase in HEAs [3]. Therefore, a new model to incorporate the non-ideality and non-configurational effects into the evaluation of the mixing entropy of HEAs needs to be developed. The first case study is focused on developing such a new model. In addition, the results of the developed model has been benchmarked on an experimentally well characterized HEA, *i.e.* Al_xCoCrFeNi alloy. Its FCC to BCC phase transition and atomic ordering have been investigated and compared to experimental results.

The subject of the second case study is the vacancy migration in α-Al_2O_3. α-Al_2O_3 is commonly used as a diffusion barrier on the surface of superalloys to prevent the internal alloy from being oxidized. Its performance is largely determined by the vacancy diffusivity in it. The vacancy diffusivity depends on the formation energy and the migration energy of a vacancy. Previous studies showed that the vacancy formation energy, hence the vacancy concentration, is sensitive to the charge state and the electronic structure of a vacancy [4, 5]. However, whether there is such a charge effect on the vacancy migration energy is still unknown. Moreover, current theoretical predictions of the activation energy for vacancy diffusion [6, 7] are inconsistent with experimental measurements [8]. In these simulations, only neutral vacancies have been investigated. But it is believed that the charged vacancies are the diffusion species in α-Al_2O_3. Therefore, the diffusion of the charged vacancies in α-Al_2O_3 should be investigated. The second case study focuses on the diffusion of charged vacancies in α-Al_2O_3. The charge effect on the vacancy migration energy and its relation with the electronic structure have been discussed.

1.2 HYPOTHESES OF THE STUDY

In the first case study of the entropy of HEAs, following hypotheses have been tested:

- *Al addition reduces the configurational entropy of Al_xCoCrFeNi alloys.* It has been found that the chemical long-range order is absent in CoCrFeNi alloy [9]. But in BCC Al_xCoCrFeNi alloy, the B2-type long-range order has been found [10, 11]. Therefore, Al addition enhanced the ordering effect, hence the non-ideality, in Al_xCoCrFeNi alloys. It is believed that the non-ideality in an alloy reduces its configurational entropy. So, it is hypothesized that Al addition will reduce the configurational entropy of Al_xCoCrFeNi alloys.
- *Considering the atomic vibration effect will improve the prediction of the compositional boundary of the FCC-BCC duplex region in the Al_xCoCrFeNi HEA system.* Current theoretical predictions [12, 13] of the upper compositional boundary of the FCC-BCC duplex region in the Al_xCoCrFeNi HEA system are all much greater than the experimental result [14]. Only configurational entropy has been considered in these works. It is suspected that non-configurational entropy may have an effect on the quantitative prediction of the compositional boundary of this FCC-BCC duplex region. Vibrational entropy, as an example of non-configurational entropy, has been found to be important to the FCC-BCC phase transition of pure metals [15, 16]. Therefore, it is hypothesized that considering the atomic vibration effect will improve the prediction of the compositional boundary of the FCC-BCC duplex region in the Al_xCoCrFeNi HEA system.

In the second case study of the vacancy diffusion in α-$\mathrm{Al_2O_3}$, following hypotheses have been tested:

- *The greater the charge of a vacancy in α-Al_2O_3, the lower its migration energy.* The formation energy and the migration energy of the neutral vacancies in α-$\mathrm{Al_2O_3}$ have been found to be extremely large [6, 7]. The calculated migration energy itself is comparable to the experimental activation energy which should be the sum of the formation energy and the migration energy. However, the charged vacancies are usually considered as the diffusion species in α-$\mathrm{Al_2O_3}$. It has been found that the charged vacancy has a lower migration energy than the neutral vacancy in GaN [17] and ZnO [18]. It is highly possible that such charge effect on the vacancy migration energy also exists in α-Al_2O_3. Therefore, it is hypothesized that the greater the charge of a vacancy in α-Al_2O_3, the lower its migration energy.

- *The greater the defect level shift during the vacancy migration, the greater the difference in the migration energy between the vacancies in different charge states.* Vacancies introduce defect levels in the band gap of metal oxides [19, 20, 21]. There are different numbers of electrons filled in these defect levels of the vacancies in different charge states. Due to the change in structure during the diffusion, these defect levels may shift. This shift will contribute to the vacancy migration energy if there are electrons in the defect levels. Therefore, it is hypothesized that the greater the defect level shift during the vacancy migration, the greater the difference in the migration energy between the vacancies in different charge states.

1.3 OBJECTIVES OF THE STUDY

The major objective of the first case study is to develop and test a computational scheme for evaluating the entropy of HEAs. To achieve such an objective, an empirical potential for energy calculation needs to be developed and the algorithm of thermodynamic integration needs to be implemented. The Al_xCoCrFeNi HEA system was chosen as the testing system. Its phase stability and the atomic ordering in it have been extensively investigated in experiments [10, 22, 23, 11, 24, 25]. Therefore, these two properties of Al_xCoCrFeNi HEAs were modelled for testing purpose. To test the two hypotheses of this case study, the configurational and vibrational entropy of Al_xCoCrFeNi HEAs have been calculated. The effect of Al addition on the configurational entropy has been investigated, and its relation to the atomic ordering effect in the alloys has been inspected. The compositional boundary of the FCC-BCC duplex region has been predicted by using only the configurational entropy and both the configurational and vibrational entropy. The results have been compared with each other to check the effect of the vibrational entropy.

For the second case study, the major objective is to build a link between the electronic structure and the diffusion kinetics of the vacancies in α-Al_2O_3. This objective requires the employment of atomistic simulation methods based on quantum mechanics which provide the information of electronic structures. It also requires identification of the possible charge states and the diffusive paths of the vacancies in α-Al_2O_3. Moreover, the impurity atom effect on the electronic structure of vacancies was investigated as a potential way to control the diffusion kinetics of point defects. To test the two hypotheses of this case study, the migration energy of the vacancies in different charge states has been calculated. The defect level shift during the diffusion has also been investigated by checking the density of states of electrons. The relation between the defect level shift and the migration energy of the vacancies in different charge states has been discussed.

1.4 SIGNIFICANCES OF THE STUDY

The study is significant in following ways:

1. The entropy evaluation scheme is the first attempt to quantify the mixing entropy of a non-ideal solid solution. Though mixing entropy is an important thermodynamic variable for alloy design, the only model before this study for mixing entropy evaluation is the ideal solution model. This study, however, emphasized on the effect of the non-ideality in alloys. It essentially challenged materials scientists to revisit the concept of mixing entropy.
2. HEAs such as Al_xCoCrFeNi alloy have an extremely large configurational space. The study on HEAs shows that Monte Carlo simulation is an efficient tool to sample such a large configurational space. It reveals that the thermodynamic properties of HEAs can be obtained by averaging over a manageable number of possible atomic configurations. The developed method is worth to be further extended to other HEAs and materials.
3. The study on the vacancy diffusion in alumina for the first time established a link between the electronic structure and the diffusion kinetics of the point defects in metal oxides. It is already known that the defect concentration can be tuned by adjusting the Fermi

energy of metal oxides [4]. But the link built in this study provides a new possibility to tune the point defect diffusivity by modifying the behavior of the electronic structure during the diffusion. This is a new degree of freedom for defect engineering that can be further explored.

4. Linking diffusion kinetics to defect electronic structure offers a new perspective to understand the reactive element effect which reduces the diffusivity of Al in alumina. Conventionally, the reactive element effect is explained by geometric blockage. However, this study shows that the reactive element effect could be partially a result of the electronic structure modification. This reveals the importance of the electronic structure to the properties of materials that are not electromagnetic properties.

2.0 LITERATURE REVIEW

2.1 ENTROPY OF HIGH ENTROPY ALLOYS

2.1.1 Entropy in alloys

In general, there are two types of entropy in an alloy system, namely, the configurational entropy and the non-configurational entropy. The configurational entropy originated from the mixing of different atoms. It is a measure of possible atomic arrangements in a certain lattice structure. Thus for pure metals or intermetallic compounds without defects, which have a unique arrangement of atoms, the configurational entropy is 0. Only solid solutions with many possible atomic arrangements have a positive configurational entropy. So, the configurational entropy is considered as the major driving force of solid solution formation in HEAs [1]. On the contrary, non-configurational entropy is non-zero for all the solids. Several aspects of the solid can contribute to the non-configurational entropy. For example, the thermal vibrations of atoms around its equilibrium position produces the vibrational entropy [26], while the different arrangements of local magnetic moment on the magnetic atoms in an alloys brings about the magnetic entropy [27]. Moreover, the partial occupancy of electrons on the electronic bands near the Fermi energy of an alloy introduces the electronic entropy [28]. Non-configurational entropies were ignored in most studies of HEAs. However, the vibrational entropy of disordered Ni_3Al alloy is found to be about 0.3 R greater than that of $L1_2$ phase [29]. This value is less than the 0.56 R of the configurational entropy but is large enough to affect the relative stability between the disordered and $L1_2$ Ni_3Al alloy.

Therefore, it is also important to evaluate the non-configurational entropy of HEAs. In this study, vibrational entropy is investigated in this work as an example of non-configurational entropy in HEAs.

Current model for evaluating the configurational entropy of HEAs is the model of ideal solution [12, 30, 31]. In the ideal solution model, the configurational entropy is calculated by

$$S_c = R \ln \Omega, \tag{2.1}$$

where R is the gas constant and Ω is the total number of possible atomic configurations for a given lattice structure. The underlying assumption of this model is that all the atomic arrangements has an equal probability to occur in the alloy. However, this assumption is hardly true in any real alloy, in which some atomic arrangements are usually more probable to occur than others [32, 33, 34, 35]. This, in some cases, are caused by the size mismatch between atoms of different element, which effect on the configuration entropy has been considered by Ye *et al* [36]. But, mostly, the different bonding energy between different element pairs is a more important factor than atomic size [37, 3]. Otto *et al* investigated the element effect on the mixing entropy by substituting elements in CoCrFeMnNi alloy, which is a single phase alloy in FCC structure [3]. By substituting one element in CoCrFeMnNi by another element with same crystal structure, similar size and similar electronegativity, five new quinary alloys have been synthesized. None of these new alloys were found to be in single phase of solid-solution as for CoCrFeMnNi. This shows clearly the importance of element effect. Therefore, a model that incorporates the interaction between different elements is needed for evaluating the entropy of HEAs, which, unfortunately, has not been developed yet.

The most commonly used method in vibrational entropy calculation is based on harmonic approximation of atomic vibrations. Under this approximation, atomic vibrations in the alloy can be decomposed into vibrations of $3N$ independent harmonic oscillators (phonons), where N is the number of atoms in an alloy. Knowing the vibrational frequency of these phonons, the vibrational entropy of the alloy is calculated by [38]

$$S_v = k_B \sum_{i}^{3N} \left\{ \frac{\hbar\nu_i}{2k_BT} \coth\left[\frac{\hbar\nu_i}{2k_BT}\right] - \ln\left[2\sinh\left(\frac{\hbar\nu_i}{2k_BT}\right)\right]\right\} \tag{2.2}$$

where k_B is the Boltzmann constant, $\hbar$ is the reduced Planck constant and ν_i is the vibrational frequency of the i-th phonon. This method can provide predictions of thermodynamic properties of alloys in good agreement with experimental results at low temperature [16, 39]. But it fails to capture the anharmonic vibrational effect which becomes important at high temperature [40, 41]. Moreover, current method for phonon frequency calculations relies on the crystal symmetry to reduce the essential numbers of calculations [42, 43]. But the absent long-range chemical ordering in HEAs makes this type of calculations intractable. Therefore, a method to evaluate the vibrational entropy in HEAs is also lacking just as that for configurational entropy.

In summary, the method to calculate the configurational and vibrational entropy of HEAs is needed to be developed. In this work, an entropy evaluating scheme to calculate both the configurational and vibrational entropy in HEAs has been developed. In this method, empirical potential was used as the energy calculator and a set of MC simulations was used to evaluate the thermodynamic properties of HEAs. The configurational and vibrational entropy of Al_xCoCrFeNi alloys were investigated by this method.

2.1.2 Ordering effect in alloys

The investigation of atomic ordering effect in alloys is an important tool to understand the thermodynamic properties of HEAs. The ordering effect in alloys often indicates an enthalpy effect which makes the alloy deviate from an ideal solution [44, 45, 46]. Therefore, it provides information on the origin of the non-ideality in HEAs, which explains the reduction of the entropy from the entropy of ideal solution. Moreover, the atomic ordering in alloys can be extracted from the experimental structure factor obtained by diffraction experiments using X-ray [9, 47], electron [48, 49] or neutron [50, 47]. Hence, the analysis of atomic ordering in HEAs can be used to connect the experiments with theoretical works, thus offering evidences to validate and improve current theory.

In general, three types of ordering effect can be found in an alloy, namely, long-range-order (LRO), short-range-order (SRO) and medium-range-order(MRO). LRO is the repetition of a certain pattern of atomic structure over a large distance compared to interatomic distance. It can be found in the ordered alloys such as Cu_3Au ($L1_2$ structure) [51], NiAl (B2 structure) [52] and NiPt ($L1_0$ structure) [53]. In these alloys, a group of atoms is arranged in a three dimensional (3D) lattice structure, which makes the atomistic structure of these alloys invariant under the translation by any integer linear combination of lattice vectors. Because of this 3D periodic arrangement, the structure factor of these alloys is also a 3D lattice in the reciprocal space. Thus, in the diffraction pattern of these alloys, a set of discrete peaks can be observed. It is commonly believed that the chemical LRO is absent in HEAs [9]. X-ray and neutron scattering investigation of CoCrFeNi HEA shows that, though the discrete peaks of FCC phase can be observed in the diffraction pattern, the superlattice peaks indicative of chemical ordering are lacking in CoCrFeNi HEA. This shows that the topological LRO of FCC lattice has been kept in this HEA but the chemical LRO is missing in it. However, the X-ray diffraction pattern of Al_xCoCrFeNi and Al_xCoCrCuFeNi alloy shows clear evidence of ordered B2 phase [10, 11, 37]. The atomic structure of this B2 phase is identified to be Al and small fraction of Fe in one sublattice while Ni and Co in another sublattice [37, 54]. Therefore, there could still be partial chemical LRO existed in HEAs.

Contrary to the LRO, SRO is the atomic ordering over the distance comparable to the interatomic distance. It has been found in amorphous alloys, *e.g.* $Zr_{62-x}Ti_xAl_{10}Cu_{20}Ni_8$ [55] and $Zr_{66.7}Ni_{33.3}$ [48] and disordered alloys, *e.g.* FeCr alloy [34]. In these alloys, a certain local structure, *e.g.* icosahedral cluster [32, 33] or typical occupancies in the first and second nearest neighbor of atoms of an element [34, 35], can be found to be dominant. But these structures are packed in a random way so that no LRO was detected. The structure factor of alloys with SRO usually has one or two peaks near the origin of the reciprocal space and a flat tail oscillating around unity [56, 57, 55]. Though there has been a lack of experiments, the SRO in $Al_{1.3}$CoCrCuFeNi alloy has been investigated by *ab initio* MD [37]. It is found that the bonds of Al-Ni, Fe-Cr and Cu-Cu are largely preferred in the alloy while Al-Al and Cr-Ni bonds are unfavored. Moreover, there are also evidences from both DFT calculations and MC simulations which show that Cr brings SRO in CoCrFeNi alloy [46, 58, 59]. These studies show that chemical SRO can cause non-ideality in HEA even if the chemical LRO is lacking.

MRO is the atomic ordering over the range between, roughly speaking, 5 Å and 20 Å [60]. It is related to SRO for that it usually depicts a certain packing method of the SRO clusters. For example, in $Ni_{81}B_{19}$, $Ni_{80}P_{20}$ and $Zr_{84}Pt_{16}$ alloys, the solute center SRO clusters are found to packed with icosahedral topological order due to the correlation between solute atoms [32]. Percolated network of fivefold SRO clusters has also been found in $Al_{75}Cu_{25}$ liquid alloys [61]. Experimentally, a prepeak in the structure factor is a typical feature of an alloy with MRO [56, 57, 62]. At present, the investigations of MRO in HEAs are still lacking. Studies, either experimental or theoretical, are needed to identify the existence of MRO in HEAs.

In summary, LRO, SRO and MRO can all exist in HEAs and may cause the reduction of entropy from that of ideal solutions. In this work, the atomic ordering effect in Al_xCoCrFeNi alloys were investigated. This information of atomic ordering provides a description of the non-ideality in Al_xCoCrFeNi, which can be validated by experiments.

2.1.3 Al Effect on the FCC-BCC phase transition in Al_xCoCrFeNi HEA system

It is known that Al stabilizes BCC phase in HEAs. Al has been found to stabilize the BCC phase in Al_xCoCrCuFeNi, Al_xCoCrFeNi, $Al_xCrFe_{1.5}MnNi_{0.5}$, Al_xCoCrFeNiTi, and $Al_xCrCuFeNi_2$ alloys [25]. With the addition of Al content, these alloys transit from FCC phase into BCC phase and B2 phase. In the binary phase diagram of Al-Ni [52], Al-Fe [63] and Al-Co [64], all alloys form intermetallic compound in B2 structure at equiatomic concentration. Therefore, it is not surprising that Al stabilizes BCC structure in HEA systems containing Ni, Fe and Co.

The interactions between Al and transition metals are different from the interactions between transition metals. Unlike transition metals the bonds between whom are usually *s*-*s* or *s*-*d* bonds, Al forms bonds with transition metals through *s*-*p* or *p*-*d* bonds. These *p*-orbital related bonds are usually stronger than bonds between transition metals and shows strong directionality. Therefore, Al usually forms intermetallic compounds, which stays in an ordered crystal structure such as BCC related B2 phase [52, 63, 64], with transition metals.

The BCC stabilizing effect of Al in Al_xCoCrFeNi alloys has been extensively explored in experiments. Kao *et al* [10] investigated the FCC to BCC transition in Al_xCoCrFeNi ($0 \leq x \leq 2$) alloys which have been annealed at 1373 K for 24 hours. The X-ray diffraction (XRD) pattern reveals that the FCC phase is stable when $x \leq 0.375$ while the BCC phase is stable when $x \geq 1.25$ for as-homogenized alloy. It is found that the BCC phase is composed of Ni-Al enriched B2 phase and Fe-Cr enriched BCC phase [24] and the phase transition is mainly caused by the precipitates of B2 phase [10]. The temperature effect on the phase stability of Al_xCoCrFeNi ($0 \leq x \leq 1.8$) has been studied by Wang *et al* [11] as well. It is found that when $x \leq 0.3$, the alloy was kept in FCC structure for the whole temperature range between room temperature and 1373 K. When $x \geq 1.5$, the alloy was in BCC structure in the whole temperature range but has a transition from disordered phase to ordered phase following temperature increases. Moreover, σ phase was found in the alloy when x is between 0.9 and 1.2 in the temperature range from 873 K to 1173 K. The existence of σ phase is not surprising for that it has been found in binary alloy of Fe-Cr and Co-Cr alloys, but a transition from disordered phase to ordered phase with increasing temperature is unusual, for that entropy has a larger effect at higher temperature, which favors the formation of disordered phase.

Other than experiments, theoretical method has also been used to predict the phase stability of Al_xCoCrFeNi alloys. Tian *et al* [12] investigated the FCC to BCC transition of Al_xCoCrFeNi by DFT calculations. The range of Al concentration when FCC and BCC coexisting was determined to be $0.597 \leq x \leq 1.229$ at 300 K. CALPHAD approach using the database of binary and ternary alloys was also used to build the phase diagram of Al_xCoCrFeNi alloys [13]. The FCC-BCC duplex region at 1100 °C is predicted to be between $x = 0.35$ and $x = 1.65$. Though the stabilization of BCC phase by Al addition has been captured, none of the methods provides a satisfied prediction of the boundary of the FCC-BCC duplex region as compared to the latest experimental range of $0.3 \leq x \leq 0.7$ [14]. The reason for this discrepancy may come from the ignorance of non-configurational entropy in these simulations. In this work, vibrational entropy has been evaluated as an example of non-configurational entropy. It is found that atomic vibration has an strong effect on the relative stability between the FCC and BCC phase.

2.2 VACANCY DIFFUSION IN α-Al_2O_3

2.2.1 Diffusion of Al and O in α-Al_2O_3

The diffusivity of oxygen anions and aluminum cations in α-Al_2O_3 have been extensively measured in experiments [65, 66, 67, 68, 69, 70, 71, 72, 73, 74, 75]. Oxygen diffusion in undoped α-Al_2O_3 single crystals and polycrystals have been measured by several research groups using either secondary ion mass spectroscopy (SIMS) or nuclear reaction analysis (NRA) techniques to determine the ^{18}O depth profiles following high temperature exchange with ^{18}O-enriched oxygen gas. From Arrhenius plots of diffusion coefficient data with respect to reciprocal temperature, the activation energy for O diffusion in α-Al_2O_3 could be obtained in these measurements. The currently available experimental results indicated that the activation energy for O lattice diffusion fell into the range between 531 kJ/mol (*i.e.*, 5.50 eV) [72] and 787 kJ/mol (i.e., 8.15 eV) [67] while the activation energy for O grain-boundary diffusion varied from 294 kJ/mol (*i.e.*, 3.05 eV) [69] to 896 kJ/mol (*i.e.*, 9.29 eV) [70]. It is notable above that the measured activation energy for O grain-boundary diffusion could be even higher than that for O lattice diffusion. Indeed, Prot *et al* found the activation energy for O lattice diffusion to be 636 kJ/mol (*i.e.*, 6.59 eV) while that for O grain-boundary diffusion to be 896 kJ/mol (i.e., 9.29 eV) in their measurement [70]. Moreover, Nakagawa *et al* reported their measured activation energy for O grain-boundary diffusion to be 627 kJ/mol (*i.e.*, 6.50 eV) [73] which was also higher than their own value (531 kJ/mol) [72] for O lattice diffusion. This finding in α-Al_2O_3 is contrary to what is normally found in metals. Furthermore, recent experimental data revealed that the O diffusion coefficients could vary up to 10^3 times along different grain boundaries (GBs) in α-Al_2O_3 and were closely related to the local arrangement of atoms on the GBs [75].

As compared to O diffusion, the experimental studies on Al diffusion in alumina are relatively scarce. So far, there are only two measurements of Al diffusion processes by analyzing the attained profiles of ^{26}Al tracers in undoped α-Al_2O_3 samples at elevated temperatures. It was found that the activation energy for Al diffusion was 477 kJ/mol (*i.e.*, 4.94 eV) [66] in polycrystal alumina and 510 kJ/mol (*i.e.*, 5.29 eV) [68] in single crystal alumina. These results suggested that the Al lattice diffusion (with activation energy of 5.29 eV) would be faster than the O lattice diffusion (with activation energy of at least 5.50 eV) in α-Al_2O_3. In addition, Ref. [68] reported that the Al grain-boundary diffusion could also have higher activation energy [850 kJ/mol (*i.e.*, 8.81 eV)] than the Al lattice diffusion in alumina.

Complementary to experimental measurements, computer simulation techniques have already been employed to elucidate the mechanism of diffusion processes in alumina at an atomistic scale [6, 76, 77, 7, 78]. Jacobs *et al* calculated the activation energy for O vacancy migration in α-Al_2O_3 lattice to be about 1 to 2.5 eV using both the semi-empirical model and pair-wise Buckingham empirical potentials [79]. As compared with experimental data (*i.e.*, 5.50 to 8.15 eV), these theoretical predictions were obviously too low. Achieving an improved agreement between theory and experiment, Aschauer et al extracted the activation energy for O lattice diffusion to be 510.83 kJ/mol (*i.e.*, 5.29 eV) from their empirical pair potential based metadynamics and the kinetic Monte Carlo simulations [7]. Both studies (Refs. [6] and [7]) pointed out that there were multiple elementary routes contributing to the overall O diffusion processes in alumina. Regarding the short-circuit diffusion mechanisms in alumina, Harding *et al* [76] calculated the activation energies for Al vacancy migration along various GBs using the same empirical pair potential employed in Ref. [7]. They found that not only the metal vacancy diffusion behavior varied greatly from one GB to another but also the individual hops within the same GB differed considerably. Relevantly, Milas *et al* investigated the diffusion of Al and O atoms on the (0001) surface of α-Al_2O_3 DFT calculations [78]. It was predicted that Al surface diffusion would be facile with activation energy of 0.73 eV but O surface diffusion would involve intermediate metastable state with an overall energy barrier of 1.67 eV.

The difference between the theoretical and experimental activation energy reveals that some aspects are missing in present theoretical models. Charge state of the vacancy could be the missing piece. It has been found that the migration energy of N in GaN can be changed by tuning the charge state of N vacancy [17]. Similar charge state dependence of vacancy migration energy has also been found in ZnO [18]. It is also known that the formation energy of vacancy in α-Al_2O_3 depends on the charge state [5]. Therefore, the charge state of vacancy is worth to be considered. A recent work by Yang *et al* [80] shows that the migration energy of O vacancy has a strong dependence on the charge state of it. However, whether the migration of Al vacancy has the same dependence is not explore. More importantly, no explanation of this charge effect has been provided yet. Therefore, it is interesting to investigate the dependence of migration energy on the charge state of vacancy in α-Al_2O_3.

2.2.2 Electronic structure of vacancies in insulating metal oxides

Most metal oxides are insulating [81]. For an ideal insulating metal oxides without defects, an energy gap exists in the band structure which separates the fully occupied valence band (VB) and the empty conduction band (CB). Usually, for binary metal oxides, the VB edge consists mostly of $2p$ orbital of oxygen while the CB edge is dominated by the empty valence orbitals of metal atoms [82, 83, 84]. When vacancies exist in metal oxides, however, defect energy levels will be introduced in the band gap or near the band edges [19, 20, 21]. These defect levels could be donors, acceptors or traps of electrons, which modify the electronic and optical properties of metal oxides, *e.g.* change the electric conductivity and the color of TiO_2 [85].

The physical reason for the formation of defect levels can be understood by a simple idea from the hydrogenic effective-mass theory [21, 20]. In a perfect crystal of metal oxides at 0 K, when an extra electron is introduced in, it will fill the CB edge for that the CB edge is the lowest available energy state. However, when an anion is removed from the lattice site, extra positive charges are introduced around the vacancy as compared to the perfect crystal. In this case, when an extra electron is added to metal oxides, it will be attracted to the anion vacancy and form a bounded state whose energy is lower than the CB edge. Only when more electrons are introduced in so that the positive charges near the anion vacancy are neutralized, the excess electrons will start to occupy the CB edge. Therefore, anion vacancies introduce defect levels, which can accommodate number of electrons equal to the positive charges of the vacancy, below the CB edge. For the cation vacancy, on the contrary, there are extra negative charges near it. So the electrons are repelled from and the holes are attracted to the vacancy. Therefore, bounded states of holes above the VB edge will be introduced by cation vacancies. These levels can accommodate holes with the same number as the negative charges of the vacancy.

These defect levels play an important role in controlling the properties of metal oxides. When the defect levels are close to the VB or CB edge, which means that the energy difference between the defect levels and the VB or CB edge is comparable to $k_B T$, electrons can be easily moved to or removed from the defect levels by thermal excitations. This allows the controlling of the electric conductivity of metal oxides [19]. On the contrary, when the defect levels are far away from the VB and CB edge, which means that the energy difference between the defect levels and the VB and CB edge is much greater than $k_B T$, electrons and holes are trapped in the defect levels so that they do not have much effect on the electric conductivity. However, these deep levels are recombination centers of electrons and holes that can change the adsorption and emission spectrum of metal oxides [86]. Moreover, the position of these defect levels also have an impact on the relative stability of the vacancies in different charge states [5].

Because of their importance, extensive simulation works have been done to investigate the defect levels of vacancy in metal oxides using DFT simulations [5, 19, 84, 87]. In these works, the relative stability of the vacancies in different charge states and the position of defect levels in the band gap of metal oxides have been studied. However, these works only focused on the relation between the electronic structure and the equilibrium state of vacancies. In this study, on the contrary, DFT calculations have been used to investigate the motion of defect levels during the vacancy migration. During the migration process, the charged vacancy moved from one site to another site. This must correspond to a charge redistribution near the vacancy which could lead to a shift of the defect levels. If there are electrons in the defect levels, this shift may have an effect on the vacancy migration energy. DFT calculation is known to underestimate the band gap of metal oxides. This prevents the accurate prediction of the defect level position. However, a qualitative inspection of the electronic structure change during the vacancy migration can still be obtained by DFT calculations. This information can be used as a starting point for future simulations using more advanced techniques such as quantum Monte Carlo method [88].

3.0 METHODOLOGY: ATOMISTIC SIMULATIONS

3.1 OVERVIEW

Atomistic simulations refer to a set of simulation methods that model the materials on the atomistic scale. Starting from the most basic ideal that materials are made of atoms, the properties of materials are calculated by applying fundamental physical laws such as Newton's second law, Schrödinger equation and statistic mechanics. Thus, atomistic simulation is considered to be a research method which is independent of experiments. Usually, it requires very few inputs from experimental data. This independence makes atomistic simulation a good complement to experiments in material science.

Atomistic simulations complement experiments in several ways. First, all conditions in atomistic simulation are controllable. Thus, by comparing experimental results to simulation results, whether there is any uncontrollable factor can be detected and how large these factors influence the experimental results can be determined. Traditionally, uncontrollable factor in experiments can only be ruled out by largely repeating of experiments. With the help of atomistic simulations, the number of repeated experiments can be reduced to a small number.

Second, atomistic simulations provide information of materials that are hard to, or sometimes cannot, be measured in experiments. Restricted by the spatial and temporal resolution of experimental equipment, certain information, such as vacancy concentration in materials, nucleation mechanism of dislocations and changing in electronic structure during diffusion, can rarely be measured in experiments. On the contrary, this information can be obtained by several runs of atomistic simulations. This detailed information offers better understanding of material behavior, sometimes can be used as guidance for developing of new materials [89].

Third, atomistic simulation can be used in researching material behavior under extreme conditions, *e.g.* high temperature, high pressure and/or under nuclear radiations. Experiments in these conditions are difficult either because of a lack of experimental equipment or simply because it is too dangerous. Atomistic simulations, however, can always be done for that these conditions are just numbers stored in computer memory. Properties of materials working in nuclear reactor have been long investigated by atomistic simulations. For instance, atomistic simulations has been done to investigate the defect production in collision cascade in Zr [90]. The primary damage due to α-decay self-radiation in UO_2 is also studied by atomistic simulations [91].

Atomistic simulation methods link the microscopic properties of atoms and the macroscopic properties of materials following the rules of statistic mechanics. Therefore, there are two levels of atomistic simulation methods, *i.e.* energy calculators which describe the interaction between atoms and modelling methods which model the behavior of a large number of atoms. Energy calculators can be based on quantum mechanics or empirical models. Modelling methods can be deterministic or stochastic.

The most commonly used energy calculator for solid-state system is the density functional theory (DFT) [92, 93] which originated from quantum mechanics. Compared to other quantum-mechanics-based energy calculators such as Hartree-Fock method [94] and Quantum Monte Carlo [88], DFT has the advantage of relatively low computational cost but still reasonable accuracy. Therefore, it has been widely used in calculating materials properties such as the formation energy of alloys [46, 95], the vacancy formation and migration energy in metal oxides [5, 77], and the electronic structure and magnetic properties of nanoparticles [96, 97]. Rooted in quantum mechanics, DFT requires almost no experimental data as input. So DFT calculation is sometimes also referred to as *ab initio* or first principle calculation in computational materials science.

Another commonly used energy calculator is the empirical potential, such as modified embedded atom method (MEAM) [98] and reaction force field [99]. Instead of simulating the interaction between atoms on the electronic structure level, empirical potentials describe the interatomic interactions by model functions. In these model functions, there are adjustable parameters which need to be determined for a specific material system. These parameters are usually fitted to materials properties from experimental measurements or DFT calculations. Compared to quantum-mechanics-based energy calculator such as DFT, the computational cost of empirical potentials is much lower. Therefore, they have been extensively used in large scale simulations with millions of atoms. However, one empirical potential cannot accurately reproduce all the properties of a material at the same time. The parameters may need to be tuned for each specific problem. Moreover, without the information of electrons, empirical potentials can only be used in simulations of mechanical and thermodynamic properties. Quantum-mechanics-based energy calculators are necessary for simulations of electronic, magnetic and optical properties of materials.

Molecular dynamic (MD) [100] simulation models the behavior of a group of atoms in a deterministic way. The ideal of MD simulation is considering atoms as mass points in classical mechanics, then solving the equations of motion for given initial and boundary conditions. The energies and forces used in the equations of motion need to be generated by an energy calculator either based on quantum mechanics or model functions. The deterministic trajectories of all the atoms are traced during the simulation. The macroscopic properties of materials can be calculated by the time average of the microscopic properties of atoms over the simulation process. The deterministic nature of MD simulation makes it a very good tool for investigations of the dynamic and kinetic processes in materials. Large amount of works have been done by MD simulations on the deformation mechanism of metals and alloys [101, 102], the diffusion of atoms in grain boundary and triple junction [103, 104], the motion of proteins [105, 106], *etc.*

Monte Carlo (MC) [107] simulation, on the contrary, models the behavior of a group of atoms in a stochastic way. It is a sampling method which generates configurations of atoms from a certain probability distribution. Then the macroscopic properties of materials can be calculated by averaging the microscopic properties of atoms over the sampled configurations. This stochasticity makes MC simulations efficient in evaluating the equilibrium properties of a material. Several varieties of MC simulations, *e.g.* Metropolis algorithm [108], Wang-Landau Sampling [109] and thermodynamic integration [110], have been developed for the purpose of evaluating equilibrium properties of materials. These methods have been used to investigate materials properties such as the equilibrium concentration on segregated surface [111], the free energy of alloys [112] and the equilibrium concentration of hydrogen adsorption [113].

Though they have been widely used in studies of materials properties, there are two common limitations of all atomistic simulation methods, *i.e.* the small spatial and temporal scales. Despite the rapid development of the computing power of modern supercomputers, usually no more than millions of atoms can be simulated by atomistic simulation methods. For three dimensional bulk materials, this corresponds to a grain with a diameter less than one micron. Moreover, the temporal scale that can be treated by atomistic simulations is at most several nanoseconds. Clearly the manageable spatial and temporal scale of atomistic simulations are way too small compared to that of real material systems. This usually leads to unrealistic conditions such as extremely large defect concentration, high strain rate and small correlation length in atomistic simulations. Moreover, the approximations used in energy calculators and modelling methods also introduce errors in the simulation results. In this sense, atomistic simulations should be considered more as tools for qualitative analyses than quantitative predictions. Cautions are needed when interpreting the meaning of simulation results. Detailed discussions of the limitations of each study in this dissertation are given in the corresponding chapters.

3.2 ENTROPY OF OF HIGH ENTROPY ALLOYS

In the developed computational scheme for entropy evaluation, modified embedded atom method potential [98, 114] has been used to describe the interatomic interactions in HEAs. Then Monte Carlo simulation with conventional Metropolis algorithm [108] has been used to calculate the equilibrium configuration and energy, and thermodynamic integration [110, 115] has been used to evaluate the free energy and entropy. When testing this scheme on Al_xCoCrFeNi alloys, several assumptions have been made during the simulations. First, the configurational and vibrational entropy were calculated separately for practical calculation issue, as discussed in section 3.2.3. It has been assumed that the cross effect between these two entropies is small and will not qualitatively change the whole picture of the FCC to BCC phase transition. Second, the BCC phase was treated as a whole despite that two phases, *i.e.* Ni-Al enriched B2 phase and Fe-Cr enriched BCC phase, were found in experiments. It has been assumed that the phase separation between these two phases could be captured in MC simulations. Third, only the FCC and BCC phase related structures were used to develop the MEAM potential of Al-Co-Cr-Fe-Ni alloy system. All the simulations are performed at 1373 K, at which temperature only FCC and BCC phase are found in Al_xCoCrFeNi alloys [11]. It has been assumed that the ignorance of other phases, such as σ phase, does not have large effect on the accuracy of the potential.

3.2.1 Modified-embedded-atom-method potential developing

Modified embedded atom method [98, 114] potential is the most successful empirical potential for metal and alloy systems. Within the frame of MEAM, the energy of an alloy system is expressed as

$$E = \sum_i \left[F\left(\bar{\rho}_i\right) + \frac{1}{2} \sum_{j \neq i} \phi\left(r_{ij}\right) \right] \tag{3.1}$$

where $\bar{\rho}_i$ is the electron density at the position of atom i, r_{ij} is the separation between two atoms i and j, $F(\rho)$ is the energy of an atom embedded in the electron background ρ at its site, and $\phi(r)$ is the pair potential between two atoms with a separation of length r. The formula of both the embedded function and the pair potential depends on a predefined reference crystal structure. In this work, the reference structure for the potential of the pure metals is chosen to be the most stable crystal structure of each element, *i.e.* FCC for Al and Ni, BCC for Cr and Fe, and HCP for Co. For the cross potentials between all pairs of elements, the reference structure was chosen to be B2 structure.

The embedding function is defined by

$$F(\bar{\rho}_i) = A_i E_i^c \left(\bar{\rho}_i\right) \ln\left(\bar{\rho}_i\right) \tag{3.2}$$

Here $\bar{\rho}_i$ is the electron density at the site of atom i, A_i is a parameter which needs to be fitted, and E_i^c is the cohesive energy of the reference structure of atom i. For each element, there is a unique set of A_i and E_i^c, which needs to be determined for the potential.

Four terms contributed to the electron density $\bar{\rho}_i$ in MEAM potential, *i.e.* a spherically symmetric partial electron density $\rho_i^{(0)}$ and the angular contributions $\rho_i^{(1)}$, $\rho_i^{(2)}$, and $\rho_i^{(3)}$. These electron densities are calculated from equations listed below:

$$(\rho_i^{(0)})^2 = \left[\sum_{j\neq i} \rho_j^{a(0)}(R_{ij})\right]^2, \tag{3.3}$$

$$(\rho_i^{(1)})^2 = \sum_{\alpha} \left[\sum_{j\neq i} \frac{R_{ij}^{\alpha}}{R_{ij}} \rho_j^{a(1)}(R_{ij})\right]^2, \tag{3.4}$$

$$(\rho_i^{(2)})^2 = \sum_{\alpha,\beta} \left[\sum_{j\neq i} \frac{R_{ij}^{\alpha} R_{ij}^{\beta}}{R_{ij}^2} \rho_j^{a(2)}(R_{ij})\right]^2 - \frac{1}{3}\left[\sum_{j\neq i} \rho_j^{a(2)}(R_{ij})\right]^2, \tag{3.5}$$

$$(\rho_i^{(3)})^2 = \sum_{\alpha,\beta,\gamma} \left[\sum_{j\neq i} \frac{R_{ij}^{\alpha} R_{ij}^{\beta} R_{ij}^{\gamma}}{R_{ij}^3} \rho_j^{a(3)}(R_{ij})\right]^2 - \frac{3}{5}\sum_{\alpha}\left[\sum_{j\neq i} \frac{R_{ij}^{\alpha}}{R_{ij}} \rho_j^{a(3)}(R_{ij})\right]^2. \tag{3.6}$$

Here, $\rho_j^{a(h)}(R_{ij})$ $(h = 0,\ 1,\ 2,\ 3)$ is the atomic electron density contributed by atom j at the position of atom i. R_{ij}^{α} and R_{ij} are the α $(\alpha = x, y, z)$ components and norm, respectively, of the vector pointing from atoms j to atom i. These electron densities are combined by the following equation:

$$\bar{\rho}_i = \rho_i^{(0)} \frac{2}{1+e^{-\Gamma_i}}, \tag{3.7}$$

where

$$\Gamma_i = \sum_{h=1}^{3} t_i^{(h)} \left[\frac{\rho_i^{(h)}}{\rho_i^{(0)}}\right]^2 \tag{3.8}$$

and $t_i^{(h)}$ $(h = 0,\ 1,\ 2,\ 3)$ are parameters that need to be fitted. The atomic electron density is given by

$$\rho_j^{a(h)}(R) = \bar{\rho}_j^0 e^{-\beta_j^{(h)}(\frac{R}{r_j^e}-1)}, \tag{3.9}$$

where $\beta_j^{(h)}$ $(h = 0,\ 1,\ 2,\ 3)$ are again adjustable parameters, r_j^e is the nearest-neighbor distance of the reference structure of atom j, and $\bar{\rho}_j^0$ is the density scaling factor of atom j. Similar to A_i and E_i^c , $t_i^{(h)}$, $\beta_j^{(h)}$, r_j^e and $\bar{\rho}_j^0$ are the parameters of the potential which has a unique value for each element.

Different from the embedded function, the pair potential $\phi(R_{ij})$ in MEAM is not explicitly defined. It is calculated from the embedding function and a universal equation of state proposed by Rose *et al* [116]. The Rose equation of state for a reference structure is a function of nearest-neighbor (NN) distance R, *i.e.*

$$E^u(R) = -E^c(1+a^*)e^{-a^*}, \tag{3.10}$$

where

$$a^* = \alpha(\frac{R}{r^e} - 1) \tag{3.11}$$

and

$$\alpha = \sqrt{\frac{9B\Omega}{E^c}} \tag{3.12}$$

Here, $E^u(R)$ is the energy per atom of the reference structure with a NN distance of R, E^c and r^e are the equilibrium cohesive energy and NN distance of the reference structure, and B and Ω are the bulk modulus and the equilibrium atomic volume of the reference structure.

In the original MEAM [98] potential, only interactions between the NN atoms are considered. In this case, the energy per atom of the reference structure with the NN distance of R is

$$E^u(R) = F[\bar{\rho}^0(R)] + \frac{Z}{2}\phi(R) \tag{3.13}$$

Here, Z is the number of NN atoms and $\bar{\rho}^0(R)$ is the background electron density for the reference structure when the NN distance is R, which is calculated by

$$\bar{\rho}^0(R) = \begin{cases} Z\rho^{a(0)}(R) & \text{for FCC and BCC} \\ Z\rho^{a(0)}(R)\sqrt{1 + \frac{t^{(3)}}{3Z^2}\left[\frac{\rho^{a(3)}(R)}{\rho^{a(0)}(R)}\right]^2} & \text{for HCP} \end{cases} \tag{3.14}$$

Then the pair potential for pure element is

$$\phi(R) = \frac{2}{Z}\left\{E^u(R) - F[\bar{\rho}^0(R)]\right\} \tag{3.15}$$

When interactions between the second nearest-neighbor (2NN) atoms are also considered, Eq. 3.15 is still valid. However, in 2NN MEAM, the background density $\bar{\rho}^0(R)$ becomes [114]

$$\bar{\rho}^0(R) = \begin{cases} Z\rho^{a(0)}(R) + Zb\rho^{a(0)}(aR) & \text{for FCC and BCC} \\ Z\rho^{a(0)}(R)\sqrt{1 + \frac{t^{(3)}}{3Z^2}\left[\frac{\rho^{a(3)}(R)}{\rho^{a(0)}(R)}\right]^2} + Zb\rho^{a(0)}(aR) & \text{for HCP} \end{cases} \tag{3.16}$$

where b is the ratio between the number of 2NN and NN atoms and a is the ratio between 2NN and NN distance in the reference structure.

In the cross potential, the pair potential $\phi_{AB}(R)$ takes a different form. In B2 structure, there are two atoms in a cubic unit cell, with element A occupies the corner and element B occupies the body center. Each atom has 8 NN atoms with different element type. Therefore, the energy per unit cell is

$$2E^u(R) = F\left[\bar{\rho}_A^0(R)\right] + F\left[\bar{\rho}_B^0(R)\right] + 8\phi_{AB}(R) \tag{3.17}$$

where

$$\bar{\rho}_A^0 = 8\rho_B^{a(0)}(R), \tag{3.18}$$
$$\bar{\rho}_B^0 = 8\rho_A^{a(0)}(R), \tag{3.19}$$
$$\tag{3.20}$$

Therefore, for B2 reference structure, the pair potential $\phi_{AB}(R)$ is

$$\phi_{AB}(R) = \frac{1}{8}\left\{2E^u(R) - F\left[\bar{\rho}_A^0(R)\right] - F\left[\bar{\rho}_B^0(R)\right]\right\} \tag{3.21}$$

In current form of MEAM potential, only the pair interactions up to 2NN are considered. However, in the electron density calculations, the density contributions from farther atoms are also counted in. Therefore, a screen function is introduced to eliminate these contributions. The many-body screen function S_{ij} between two atom i and j is defined by [98, 114]

$$S_{ij} = \prod_{k\neq i,j} S_{ikj} \tag{3.22}$$

where S_{ikj} is the screening factor of atom k to the interaction between atom i and j. The screen factor S_{ikj} is calculated by

$$S_{ikj} = f_c\left(\frac{C - C_{min}}{C_{max} - C_{min}}\right) \tag{3.23}$$

where C_{max} and C_{min} are adjustable parameters, $f_c(x)$ is a smooth function, which is given by

$$f_c(x) = \begin{cases} 1 & x \geq 1 \\ \left[1-(1-x)^2\right]^2 & 0 < x < 1 \\ 0 & x \leq 0 \end{cases} \tag{3.24}$$

and C is calculated by

$$C = \frac{2(X_{ik} + X_{kj}) - (X_{ik} - X_{kj})^2 - 1}{1 - (X_{ik} - X_{kj})^2} \tag{3.25}$$

where $X_{ik} = (R_{ik}/R_{ij})^2$ and $X_{kj} = (R_{kj}/R_{ij})^2$ with R_{ij} the separation between atom i and j.

Figure 3.1: The unit cell of (a) NiCo (B2), (b) AlCr ($L1_0$) and (c) Al_3Fe ($L1_2$), which are used in potential developing.

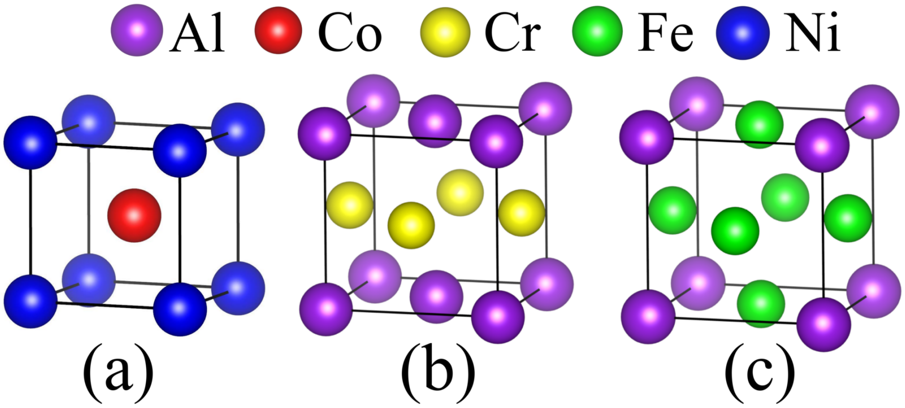

In this work, the parameters of the MEAM potential for Al, Co, Cr, Fe and Ni were obtained from literature [117, 118, 119, 120], while the cross potentials for each element pair were developed by fitting the MEAM predictions of physical properties to DFT calculation results. All the DFT calculations were carried out using Vienna *Ab initio* Simulation Package (VASP) [121, 122]. In all DFT calculations, the projector augmented wave [123] method and Perdew-Burke-Ernzerhof (PBE) [124] exchange-correlation functional were used. The energy cutoff was set to 600 eV, and the density of Monkhorst-Pack k-point mesh [125] was $11 \times 11 \times 11$. The physical properties that has been used in the fitting process were the lattice parameters and formation enthalpy of ordered AB (B2 structure as shown in Figure 3.1(a)), AB ($L1_0$ structure as shown in Figure 3.1(b)), A_3B ($L1_2$ structure as shown in Figure 3.1(c)) and AB_3 ($L1_2$ structure) phases for all element pairs.

3.2.2 Monte Carlo simulation method

In order to evaluate the thermodynamic properties and to obtain the equilibrium atomic structure of HEAs, Metropolis-type MC simulations algorithm [108] was used to sample the possible atomic configurations. In a system with constant number of atoms, volume and temperature, the probability of finding the system stay in an atomic configuration is the canonical distribution, *i.e.*

$$p(E) = \exp\left(-\frac{E}{k_B T}\right) \tag{3.26}$$

where E is the energy of the configuration, T is the temperature and k_B is the Boltzmann constant. The macroscopic property of the system is the average of the microscopic physical quantity over all atomic configurations weighted by this probability distribution. Using Metropolis algorithm, a sample of atomic configurations can be generated from the desired probability distribution. Then the average properties of these sample configurations can used be an approximation of the properties of an alloy.

To model the equilibrium Al_xCoCrFeNi alloys by MC simulations, a $8 \times 8 \times 8$ supercell of FCC crystal structure (2048 lattice points) and a $10 \times 10 \times 10$ supercell of BCC crystal structure (2000 lattice points) were built at first. In each model, Al atoms were filled in the lattice points randomly with a mole ratio of $x/(x+4)$. Then Co, Cr, Fe and Ni atoms were filled in the rest lattice points randomly with equimolar concentrations. Starting from this random structure, one of two trial motions were chosen to be done in each MC iterations. The first one is swapping two atoms with different element type. This swapping can happen between any two atoms regardless of the distance between them, once they have different element types. Therefore, every swapping generates a new configuration. The second one is displacing an atom by a small amount. This trial motion kicks the atom away from the equilibrium position thus induced the effect of vibration into the simulations. At every MC iteration, the energy difference ΔE of the alloy after and before the trial motion was calculated, and the new configuration was retained with a probability of

$$p = \min\left[1, \exp\left(-\frac{\Delta E}{k_B T}\right)\right] \tag{3.27}$$

After several MC iterations, the models of Al$_x$CoCrFeNi evolved into a state in which the energy of the system was oscillating around a constant value. This state is the equilibrium state and the alloy properties can be extracted from the atomic configurations in this state.

In this work, two types of MC simulations have been done for the purpose of separating the configurational and vibrational entropy. In the simulations of configurational entropy, only swapping of atoms was performed at each iterations. It has been found that the models entered the equilibrium state in 100 thousands MC iterations. Therefore, 2 million iterations in total were used in this MC simulations and the thermodynamic and structural properties of the alloy were obtained by averaging the corresponding properties over the configurations generated every 1000 MC iterations in the last 1 million iterations. In the simulations of vibrational entropy, only displacing of atoms was performed. In this case, the system needs 2 million iterations to reach equilibrium. Hence, 5 million iterations were used and the properties of the alloy were averaged over the configurations generated very 1000 iterations in the last 2 million iterations. The simulation temperature was set to 1373 K, which is the experimental annealing temperature of Al$_x$CoCrFeNi alloys [10]. Periodic boundary condition was assumed in all MC simulations.

3.2.3 Free energy and entropy evaluation method

In this study, thermodynamic integration (TI) [110, 115] was used to evaluate the free energy of HEAs. TI starts from the observation that the free energy difference of two systems can be evaluated by an adiabatic integration. Suppose there are two systems, 0 and 1, with same number of atoms, whose potential energy are V_0 and V_1 respectively. Then the Hamiltonian of these two systems are $H_0 = T + V_0$ and $H_1 = T + V_1$ respectively, where T is the kinetic energy of the system. Considering a system whose Hamiltonian is

$$H(\lambda) = T + \lambda V_1 + (1 - \lambda) V_0 \tag{3.28}$$

the free energy of this system is

$$F(\lambda) = -k_B T \ln \left[\int \exp \left(-\frac{H(\lambda)}{k_B T} \right) d\vec{p} d\vec{q} \right] \tag{3.29}$$

where $\vec{p}$ and $\vec{q}$ are the momentums and the positions of all the atoms. Using the identity

$$F(1) - F(0) = \int_0^1 \frac{\partial F}{\partial \lambda} d\lambda, \tag{3.30}$$

and noticing that $F(1)$ and $F(0)$ are the free energy of system 1 and 0 respectively, one can obtain a formula to calculate the free energy difference of these two systems, *i.e.*

$$\Delta F = F(1) - F(0) = \int \langle V_0 - V_1 \rangle_\lambda \, d\lambda, \tag{3.31}$$

where $\langle V_0 - V_1 \rangle_\lambda$ is the equilibrium ensemble average of the potential difference at a certain value of λ. Thus, if the free energy of one system is known, the free energy of the other system can be obtained.

However, to calculate the free energy difference by Eq. 3.31, one has to do MC or MD simulations at different λ to obtain the ensemble average of the potential difference. This can be very time consuming for that a large number of different λs are needed to get an accurate integration result. This problem can be solved by employing a time dependent λ [115]. Using a continuous function changing from 0 to 1, the free energy difference can be calculated by

$$\Delta F = \int_{t_0}^{t_1} [V_0(\lambda(t)) - V_1(\lambda(t))] \frac{\partial \lambda(t)}{\partial t} dt. \tag{3.32}$$

This formula allows the calculation of the free energy difference in one simulation without large error once the time step dt is small enough.

In order to use TI to calculate the free energy of HEA, a reference state with already known free energy is needed. If only configurational entropy is considered, it is natural to use the ideal solid solution whose potential energy is a constant

$$V = \sum_i^N E_i \tag{3.33}$$

and free energy is

$$F = \sum_i^N E_i - TS_{ideal} \tag{3.34}$$

where N is the number of atoms, E_i is the energy of each atom in their standard state, *e.g.* energy of Ni atom in FCC lattice, and S_{ideal} is the entropy of ideal solution, which is calculated by

$$S_{ideal} = -k_B \sum_i x_i \ln x_i \tag{3.35}$$

If vibrational configuration is also considered, an Einstein crystal [126] of ideal solution can be used as the reference state. The potential and free energy of this system are

$$V = \sum_i^N E_i + \frac{1}{2} K \sum_i^{3N} (\Delta x_i)^2 \tag{3.36}$$

$$F = \sum_i^N E_i - T S_{ideal} + \frac{3N\hbar\nu}{2} + 3N k_B T \ln \left[1 - \exp\left(-\frac{\hbar\nu}{k_B T} \right) \right] \tag{3.37}$$

where, K and ν are the stiffness and vibrational frequency of all oscillators, which are related by

$$\nu = \sqrt{\frac{K}{\bar{m}}} \tag{3.38}$$

Here, $\bar{m}$ is the average mass weighted by the mole fraction of each element. Once the free energy of a system is obtained, the entropy of the system can be calculated by

$$S = \frac{F - U}{T} \tag{3.39}$$

where U is the internal energy of the alloy, which can be evaluated by an independent Metropolis MC simulation.

Ideally, the total free energy and entropy including both configurational and vibrational contribution can be obtained in one TI simulation. Practically, however, the required number for MC iterations to achieve a converged estimation of free energy and entropy is too large, if the configurational and vibrational effect are considered together. Moreover, to understand the individual effect of configurational and vibrational entropy respectively, it is better to evaluate them separately. Fortunately, the cross effect between the configurational and vibrational effect on the free energy is small, for that the difference in the vibrational free energy calculated on 10 different atomic configurations of the same alloy has been found to be less than 0.1%. Therefore, two types of TI simulations were performed to evaluate the configurational and vibrational free energy separately. In the simulation of configurational entropy, the vibrations of atoms were switched off. 2 million MC iterations was used in this type of simulations, which is long enough to obtain a converged estimation of the free energy. For the vibrational entropy simulations, the atom swapping was turned off. This type of simulations requires 10 million MC iterations to get a converged value of free energy. The stiffness constant K of the Einstein crystal was set to 2 eV/Å^2 for all simulations. Periodic boundary condition was assumed in all MC simulations.

3.3 VACANCY DIFFUSION IN α-Al$_2$O$_3$

3.3.1 Density functional theory simulations

Density functional theory [92, 93] is a modelling method which is used to investigate the ground state properties of a many electron system. Using electron density as the variable which uniquely determines the energy of the system, Kohn *et al* [92, 93] prove that a many-electron Schrödinger equation can be reduce to a set of effective single-electron equations, *i.e.* the famous Kohn-Sham equations,

$$\left\{-\frac{\hbar^2}{2m}\nabla^2 + v_{\text{ext}}(\vec{r}) + e^2\int\frac{n(\vec{r}')}{|\vec{r}-\vec{r}'|}d\vec{r}' + v_{\text{XC}}[n(\vec{r})]\right\}\phi_i(\vec{r}) = \varepsilon_i\phi_i(\vec{r}) \tag{3.40}$$

with

$$n(\vec{r}) = \sum_i |\phi_i(\vec{r})|^2 \tag{3.41}$$

where $\phi_i(\vec{r})$ is the effective single-electron wave function of the i-th electron, $n(\vec{r})$ is the electron density, $v_{\text{ext}}(\vec{r})$ is the external potential, *e.g.* Coulomb potential between nuclei and electrons, at position $\vec{r}$, and $v_{\text{XC}}[n(\vec{r})] = \delta E_{\text{XC}}[n(\vec{r})]/\delta n(\vec{r})$ is the exchange-correlation potential, which describes the exchange energy of electrons caused by the Pauli exclusion principle and the energy difference, *i.e.* the correlation energy, between a set of interacting and non-interacting electrons. It is noteworthy that the term $e^2\int\frac{n(\vec{r}')}{|\vec{r}-\vec{r}'|}d\vec{r}'$, which describes the interaction between electrons, is also implicitly depends on the effective single-electron wave functions. Therefore, these equations have to be solved in a self-consistent way.

To solve Kohn-Sham equation numerically, it is necessary to discretize it into a matrix equation. This is done by choosing a set of basis functions so that the wave function and the Hamiltonian are represented by vectors and matrices in the linear space spanned by these basis functions. There are three types of basis functions commonly used in DFT simulations [127], namely, localized orbitals, plane waves and augmented functions. For crystals, which are translationally invariant, plane waves are the natural choice. Using plane-wave basis-set, all the components of the wave function and Hamiltonian can be easily calculated by fast Fourier transformation. Then the Kohn-Sham equation is solved in the Fourier space. In most plane-wave basis-set DFT codes, the number of plane waves used in one calculation is determined by an energy cutoff $E_{\text{cut}} = \frac{\hbar^2 G_{cut}^2}{2m}$, where m is the mass of electron and G_{cut} is the length of the largest wave vector of the plane wave. This energy cutoff needs to be large enough to obtain accurate results of energy and wave functions. With an appropriate energy cutoff, the ground state energy of a many-electron system can be calculated once the external potential and the exchange-correlation potential are known.

The most trivial form of the external potential is simply the summation of Coulomb potential centered on each nucleus. In this case all electrons in the system were treated explicitly. However, most properties of materials are determined by the valence electrons, while the core electrons are in most cases chemically inert. Therefore, it is reasonable to approximate the nucleus together with the core electrons of an atom as an ionic core and use an effective potential (pseudopotential) to describe the interaction between the core and valence electrons. In this way, the number of single-electron wave function that needs to be solved in a system can be largely reduced. Moreover, the orthonormality between the wave functions of core and valence electrons causes wiggles in the wave function of valence electrons near the core region. Using pseudopotential smooths out the wiggles and reduces the number of plane waves required to expand the wave function. Therefore, pseudopotentials are largely used in plane-wave basis-set DFT codes to accelerate the calculations. Three types of pseudopotentials were commonly used in plane-wave basis-set DFT calculations, *i.e.* norm-conserving pseudopotential (NCPP) [128, 129], ultrasoft pseudopotential (USPP) [130, 131, 132] and projector augmented wave method (PAW) [133, 134]. Both three pseudopotentials can provide accurate predictions of materials properties once they have been carefully tuned [134, 135]. However, USPP are the fastest for that its energy cutoff is only a third to a half of the energy cutoff of other pseudopotentials, while PAW method provide the most accurate predictions in systems with strong magnetic moments or large difference in electronegativity. So a suitable pseudopotential needs to be chosen to balance the computational cost and accuracy.

The only term that is unknown in the Kohn-Sham equation is the exchange-correlation potential. Though the exact exchange energy between the electrons can be calculated from the exchange term in Hartree-Fock theory, *i.e.*

$$E_X[n] = -\frac{1}{2}\sum_{i,j}\int \frac{\phi_i^*(\vec{r})\phi_j^*(\vec{r}')\phi_j(\vec{r})\phi_i(\vec{r}')}{|\vec{r}-\vec{r}'|}d\vec{r}d\vec{r}' \tag{3.42}$$

the exact form of correlation energy remains unknown. Even for the exchange energy in Eq. 3.42, the form of its variation with respect to the electron density n is too complicated to be implemented in an efficient way. Therefore, several approximations have been proposed to provide a simple but reasonably accurate description of the exchange-correlation energy. The first level approximation is the local density approximation (LDA), which approximates the exchange energy by

$$E_X^{LDA}[n] = -\frac{3}{4}\left(\frac{3}{\pi}\right)^{\frac{1}{3}}\int n(\vec{r}^{\frac{4}{3}})d\vec{r} \tag{3.43}$$

and parametrizes the correlation energy from quantum Monte Carlo simulations [136]. Being a rough approximation, the cohesive energy of molecules and crystals are usually overestimated by 10%-20% in LDA. However, LDA provides surprisingly accurate prediction of lattice parameters and bond lengths (within 1%) [137]. The generalized gradient approximation (GGA) take one step further to add the dependence of the gradient of electron density into the exchange-correlation functional. Several forms of GGA has been proposed such as Becke-Lee-Yang-Parr (BLYP) [138, 139], Perdew-Wang 1991 (PW91) [140] and Perdew-Burke-Ernzerhof (PBE) [124]. These exchange-correlation functionals provide more accurate predictions of cohesive energy compared to LDA. However, the lattice parameters are usually overestimated by GGA [141]. Moreover, both LDA and GGA severely underestimates the band gap of semiconductors and insulators. This band gap problem in DFT calculations is largely due to the self-interaction error (SIE) [19, 142, 143] which arises from the factor that the Coulomb interaction of an electron with itself is not totally cancelled by the approximated exchange-correlation energy in the Kohn-Sham Hamiltonian. There is no universal scheme to completely correct SIE in DFT currently. However, it is found that SIE in Hartree-Fock exchange energy and LDA/GGA exchange-correlation energy have opposite behaviors [142]. Therefore it is expected that the band gap prediction from DFT can be improved due to the SIE cancellation if Hartree-Fock exchange energy and LDA/GGA exchange-correlation energy are mixed. This leads to the hybrid functional such as PBE0 [144] and Heyd-Scuseria-Ernzerhof (HSE) [145]. In these functionals, the mixing coefficients are either predefined or fitted to experimental results. Hybrid functionals can partially improve the prediction of band gap [146], but are much more expensive than calculations using LDA and GGA. Therefore, just like pseudopotentials, a trade off between computational cost and accuracy has to be made when choosing exchange-correlation functional.

In this work, the plane-wave basis-set pseudopotential DFT calculations have been performed on VASP [121, 122] to investigate the charge effect on the vacancy migration energy in α-Al_2O_3. The PAW method [123] and PBE exchange-correlation functional were used in all calculations. The energy cutoff was set to 500 eV and the Monkhorst-Pack k-point mesh [125] with a density of $3 \times 3 \times 2$ was used for k-space integration. All the crystal structures were optimized under constant-volume restriction until the Hellman-Feynman force exerted on each ion is less than 0.01 eV/Å.

3.3.2 Evaluation of vacancy formation energy

The vacancy formation energy ΔE_f is calculated by

$$\Delta E_f = E_v^q - E_{perf} + \mu_i + q\mu_e \tag{3.44}$$

where E_v^q and E_{perf} are the energies of the simulation cell with and without a vacancy whose charge is q, μ_i (i=Al or O) is the chemical potential of Al or O and μ_e is the chemical potential of electrons. μ_e can be defined as a Fermi level ϵ_F relative to the valence-band maximum (VBM) of the perfect crystal, *i.e.* $\mu_e = E_{VBM}^{perf} + \epsilon_F$. According to this definition, the type of majority charge carriers in Al_2O_3 can be characterized by ϵ_F. If ϵ_F is close to zero, then Al_2O_3 is p-type. On the contrary, if ϵ_F is close to the conduction-band minimum (CBM), then Al_2O_3 is n-type .

The vacancies investigated in this work are oxygen vacancies with a charge of 0 (V_{O}^{0}), +1 (V_{O}^{1+}) and +2 (V_{O}^{2+}) and aluminum vacancies with a charge of 0 (V_{Al}^{0}), −1 (V_{Al}^{1-}), −2 (V_{Al}^{2-}) and −3 (V_{Al}^{3-}). These vacancies in different charge states were modelled by changing the total number of electrons in the simulation cell. The calculations of charged defects with periodic boundary condition introduces a spurious interaction between the defect and its periodic copies. Hence a correction of the defect-defect interaction is needed. Here, this spurious interaction has been corrected by using the scheme proposed by Makov and Payne [147] and Neugebauer *et al* [148]. The finite size errors estimated in this study are 0.72 eV for V_{O}^{2+} and 1.63 eV for V_{Al}^{3-}. These values are found to be within the 0.2 eV uncertainty range, as compared to the predictions from improved fitting method for finite size corrections. In the hexagonal structure, the dielectric constant of alumina varies in the direction perpendicular (9.5) and parallel (11.6) to c axis [149]. Therefore, an average value of 10.6 is used to estimate the correction.

The chemical potential of Al and O has been determined following the method suggested by Finnis *et al* [150]. The chemical potential of oxygen μ_{O} at temperature T and oxygen partial pressure p_{O_2} is

$$\mu_{\mathrm{O}} = \mu_{\mathrm{O}}^{0} + \Delta\mu_{\mathrm{O}}(T) + \frac{k_B T}{2} \ln \frac{p_{\mathrm{O}_2}}{p^0} \tag{3.45}$$

where μ_{O}^{0} is the chemical potential of oxygen at a standard state with temperature T^0=298.15 K and pressure p^0=1 atm. and $\Delta\mu_{\mathrm{O}}(T)$ is the chemical potential difference of oxygen between temperature T and T^0 at the standard pressure p^0. The latter can be obtained from thermodynamic tables [151], while the former can be determined by a combination of DFT and experimental results. For the reaction $2\mathrm{Al} + \frac{3}{2}\mathrm{O}_2 = \mathrm{Al}_2\mathrm{O}_3$, the standard Gibbs free energy change is

$$\Delta G^{0}_{\mathrm{Al_2O_3}} = \mu^{0}_{\mathrm{Al_2O_3}} - 2\mu^{0}_{\mathrm{Al}} - 3\mu^{0}_{\mathrm{O}} \tag{3.46}$$

where $\mu^{0}_{\mathrm{Al_2O_3}}$ and μ^{0}_{Al} are the chemical potential of Al_2O_3 and Al at standard state respectively. For a solid, the Gibbs free energy change is small between 0 K and 298.15 K [150]. Therefore, $\mu^{0}_{\mathrm{Al_2O_3}}$ and μ^{0}_{Al} can be approximated by the energy at 0 K from DFT calculations.

Meanwhile, $\Delta G^0_{\mathrm{Al_2O_3}}$ can be obtained from thermodynamic tables [151]. So the chemical potential of oxygen at standard state is calculated by

$$\mu^0_{\mathrm{O}} = \frac{1}{3}\left(E_{\mathrm{Al_2O_3}} - 2E_{\mathrm{Al}} - \Delta G^0_{\mathrm{Al_2O_3}}\right) \tag{3.47}$$

where $E_{\mathrm{Al_2O_3}}$ and E_{Al} are the energy of $\mathrm{Al_2O_3}$ and Al which are again from DFT calculations. With Eq. 3.46 and 3.47, the chemical potential of oxygen can be determined. Then at equilibrium condition, the chemical potential of aluminum is calculated by $\mu_{\mathrm{Al}} = \frac{1}{2}(\mu_{\mathrm{Al_2O_3}} - 3\mu_{\mathrm{O}})$ with $\mu_{\mathrm{Al_2O_3}}$ approximated by $E_{\mathrm{Al_2O_3}}$.

The Fermi energy ϵ_F of intrinsic $\mathrm{Al_2O_3}$ can be determined by enforcing the charge of the whole crystal to be zero. For a certain ϵ_F, the formation energy of each vacancy can be determined by Eq. 3.44. Then the net charge introduced by all the vacancies is

$$Q_{\mathrm{vac}}(\epsilon_F) = \sum_i q_i N_i \exp\left(-\frac{\Delta E^i_f(\epsilon_F)}{k_B T}\right) \tag{3.48}$$

where q_i and N_i are the charge and number of possible sites of defect i (i=V^0_{O}, V^{1+}_{O}, V^{2+}_{O}, V^0_{Al}, V^{1-}_{Al}, V^{2-}_{Al}, V^{3-}_{Al}). Meanwhile, ϵ_F also determines the number of electrons in conduction band and holes in valence band. The net charge of electrons and holes is calculated by

$$Q_{\mathrm{eh}}(\epsilon_F) = \int_{-\infty}^{\epsilon_F} [1 - f(E;\epsilon_F,T)]g(E)dE - \int_{\epsilon_F}^{\infty} f(E;\epsilon_F,T)g(E)dE \tag{3.49}$$

where $f(E;\epsilon_F,T) = 1/\left[1 + \exp\left(-\frac{E-\epsilon_F}{T}\right)\right]$ is the Fermi-Dirac distribution and $g(E)$ is the density of states of electrons in $\mathrm{Al_2O_3}$. Then the total charge in $\mathrm{Al_2O_3}$ can be determined at a specific ϵ_F by $Q_{\mathrm{tot}}(\epsilon_F) = Q_{\mathrm{vac}}(\epsilon_F) + Q_{\mathrm{eh}}(\epsilon_F)$. The intrinsic crystal should be electrically neutral, so the Fermi energy ϵ_F is determined by solving the equation $Q_{\mathrm{tot}}(\epsilon_F) = 0$.

3.3.3 Calculations of vacancy migration energy

The migration energy of vacancies was calculated using the nudged elastic band (NEB) method [152]. The ideal of NEB method is based on the concept of potential energy surface (PES). PES is a hypersurface in $3N$-dimensional space (N is the number of atoms) defined by $y = E(\vec{R})$. Here $\vec{R}$ is a vector in the $3N$-dimensional whose components are the coordinates of atoms. On the PES, each stable structure corresponds to a local minimum, and the path from local minimum A to local minimum B with the lowest energy is called the minimum energy path (MEP) between A and B. The point with the highest energy on a MEP is called the saddle point. The structure corresponds to the saddle point is the transition state, which determines the rate for the system transiting between A and B. NEB method is designed to find the MEP between two fixed local minima. At first step, several images are created to represent an initial guess of the MEP. Linear interpolation is commonly used to generate these images. Then, the force defined by $\vec{F} = -\nabla_{\vec{R}} E(\vec{R})$ was calculated for each image. Next, the force is decomposed into two components, *i.e.* one parallel $\vec{F}_{\parallel}$ and the other perpendicular $\vec{F}_{\perp}$ to the tangent direction $\vec{\tau}_i$ defined by

$$\vec{\tau}_i = \frac{\vec{R}_i - \vec{R}_{i-1}}{\left|\vec{R}_i - \vec{R}_{i-1}\right|} + \frac{\vec{R}_{i+1} - \vec{R}_i}{\left|\vec{R}_{i+1} - \vec{R}_i\right|}, \tag{3.50}$$

where $\vec{R}_i$ is the position of the i-th image. After this, the force exerted on the i-th image is replaced by

$$\vec{F}_{\text{NEB}} = \vec{F}_{\perp} + k\left(\left|\vec{R}_{i+1} - \vec{R}_i\right| - \left|\vec{R}_i - \vec{R}_{i-1}\right|\right)\vec{\tau}_i \tag{3.51}$$

The second term on the right hand side is a spring force with stiffness k which tries to keep the distances between any two neighboring images equal. This force prevents all the images from falling into one of the two local minima. Then the MEP is obtained by minimizing $\vec{F}_{\text{NEB}}$ for each image.

The original NEB method provides an efficient way to calculate the MEP. However, a rigorous convergence to a transition state cannot be obtained for that there is no guarantee that one of the images will fall onto the saddle point. This can be solved by a simple modification called climb image NEB (CI-NEB) [152]. In CI-NEB, the NEB force $\vec{F}_{\text{NEB}}$ was ignored on the image with the highest energy after several iterations. Instead, the parallel component $\vec{F}_{\parallel}$ was inverted in direction and minimized so that the image climbs to the saddle point. With this modification, both the MEP and transition state between two structures can be obtained at the same time.

In this work, CI-NEB method with 5 images (including two local minima) was used to search for MEP and transition state of vacancy migration in α-Al_2O_3. The force exerted on each image is minimized to be less than 0.05 eV/Å. The migration energy is calculated by the energy difference between the transition state and the vacancy state.

4.0 RESULTS AND DISCUSSIONS: ENTROPY OF HIGH ENTROPY ALLOYS

4.1 MEAM POTENTIAL FOR Al-Co-Cr-Fe-Ni ALLOY SYSTEM

The parameters of the MEAM potential for Al-Co-Cr-Fe-Ni alloy system used in this work are given in the appendix. The comparison between the MEAM and DFT predictions of the formation enthalpy and lattice parameter of ordered AB (B2) alloy for all element pairs are given in Table 4.1 as an example. The same comparison for AB ($L1_0$), AB_3 ($L1_2$) and A_3B ($L1_2$) phase are shown in the appendix. The difference in enthalpy of formation predicted by MEAM and DFT are in most cases less than 0.03 eV/atom. More importantly, the sign of the formation enthalpy, which indicates the stability of B2 phase, was correctly predict in all cases. In addition, the discrepancies in the predicted lattice parameter between MEAM and DFT are all less than 3%. This consistency between MEAM and DFT predictions shows that this potential can provide reasonable description of the properties of binary alloys.

Table 4.1: The formation enthalpy ΔH and lattice parameter a of ordered AB (B2) alloy predicted by MEAM potential and DFT calculations.

		AlCo	AlCr	AlFe	AlNi	CoCr
ΔH (eV/atom)	MEAM	-0.602	-0.035	-0.387	-0.644	0.180
	DFT	-0.603	-0.035	-0.330	-0.664	0.180
a (Å)	MEAM	2.853	3.037	2.977	2.916	2.846
	DFT	2.853	3.037	2.882	2.893	2.846
		CoFe	CoNi	CrFe	CrNi	FeNi
ΔH (eV/atom)	MEAM	-0.054	0.134	0.091	0.267	0.179
	DFT	-0.054	0.157	0.198	0.264	0.073
a (Å)	MEAM	2.843	2.878	2.834	2.956	2.882
	DFT	2.843	2.881	2.823	2.896	2.846

This potential was also tested on quaternary alloys. The formation enthalpies of ordered AlCoCrFe, AlCoCrNi, AlCoFeNi, AlCrFeNi and CoCrFeNi alloy in both FCC (as shown in Figure 4.1(a)) and BCC (as shown in Figure 4.1(b)) structure were calculated and compared to the prediction of DFT calculations. The results are given in Table 4.2. For FCC structure, the MEAM and DFT results match well with each other. For BCC structure, MEAM predictions is in general higher than DFT predictions. But the difference is less than 0.1 eV with only one exception. In addition, two method gave the same prediction of the relative stability between the BCC and FCC structure. In general, this potential provides a reasonable description of Al-Co-Cr-Fe-Ni alloy system as compared to DFT calculations but with a much shorter simulation time. Therefore, it can be utilized as energy calculator in large-scale atomic simulation, *e.g.* MC and TI simulations, whose spatial and temporal scale are too large to use DFT.

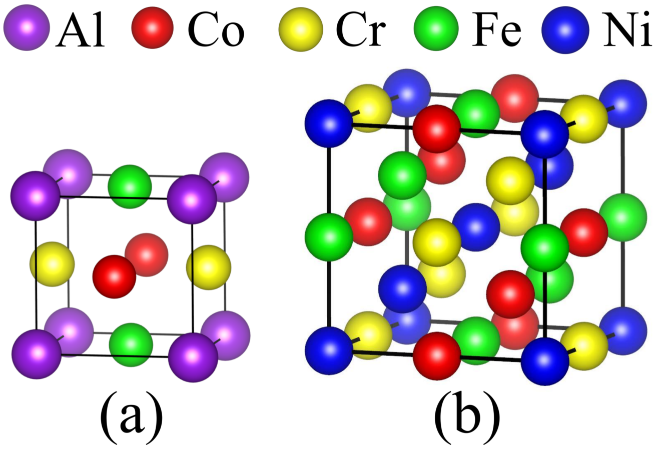

Figure 4.1: (a) The unit cell of FCC AlCoCrFe alloy and (b) the $2 \times 2 \times 2$ spuercell of BCC CoCrFeNi alloy with ordered arrangement of atoms used for potential developing.

Table 4.2: The formation enthalpy (in eV/atom) of ordered AlCoCrFe, AlCoCrNi, AlCoFeNi, AlCrFeNi and CoCrFeNi alloy in both BCC and FCC structure predicted by MEAM potential and DFT calculations.

		AlCoCrFe	AlCoCrNi	AlCoFeNi	AlCrFeNi	CoCrFeNi
FCC	MEAM	−0.088	−0.168	−0.227	−0.053	−0.011
	DFT	−0.016	−0.122	−0.256	−0.063	0.066
BCC	MEAM	0.100	0.064	−0.112	0.148	0.205
	DFT	0.001	−0.018	−0.147	−0.019	0.156

4.2 ENTROPY AND ENTHALPY OF Al$_X$CoCrFeNi ALLOYS

The entropy and enthalpy of Al$_x$CoCrFeNi alloys were evaluated by the combination of MC and TI simulations. The lattice parameter of Al$_x$CoCrFeNi alloys was determined at each x by enforcing the averaged pressure of the modelled alloy to be zero. In this case, the enthalpy and the Gibbs free energy are equal to the internal energy and the free energy of the alloy respectively. The sampled values of x and the equilibrium lattice parameters were given in Table 4.3. It shows that the Al addition increased the lattice parameter of FCC phase by 5.4%, but has a much smaller effect on the lattice parameter of BCC phase, *i.e.* less than 1.3%.

Table 4.3: The lattice parameter (in Å) of Al$_x$CoCrFeNi alloys in both FCC and BCC phase. The mole fraction of Al is calculated by $c_{Al} = x/(x+4)$.

x	0.000	0.100	0.200	0.300	0.400	0.500	1.000	1.200
c_{Al}	0.000	0.024	0.048	0.070	0.091	0.111	0.200	0.231
FCC	3.621	3.621	3.622	3.632	3.633	3.639	3.661	3.665
BCC	2.916	2.913	2.908	2.904	2.889	2.892	2.893	2.896
x	1.300	1.400	1.500	1.600	1.700	2.000	2.500	4.000
c_{Al}	0.245	0.259	0.273	0.286	0.298	0.333	0.385	0.500
FCC	3.675	3.678	3.688	3.689	3.699	3.726	3.760	3.830
BCC	2.897	2.899	2.900	2.901	2.902	2.906	2.913	2.956

The configurational and vibrational entropy are given in Figure 4.2(a) and 4.2(b) separately. The configurational entropy of all the alloys is always less than the entropy of ideal solution. So none of the Al$_x$CoCrFeNi alloys is an ideal solution. The configurational entropy of CoCrFeNi alloy in FCC phase is 1.301 R, which is only slightly lower than the 1.386 R of the ideal solution. This indicates that the FCC CoCrFeNi alloy is a near ideal solution, which is consistent with the experiments finding that chemical LRO is absent in this alloy [9]. However, with the addition of Al, the configurational entropy of FCC phase decreased from $\sim 1.3\ R$ to $\sim 1.0\ R$ and the configurational entropy of BCC phase decreased from $\sim 0.85\ R$ to $\sim 0.65\ R$. It shows clearly that Al addition introduced chemical orderings in Al$_x$CoCrFeNi alloys.

The calculated vibrational entropies are in the range of $5 \sim 8\ R$, which are comparable to vibrational entropy of 3d transition metals measured in experiments [153]. Unlike the configurational entropy, the vibrational entropy of FCC and BCC phase show different dependences on Al content. For the FCC phase, the vibrational entropy first decreased then increased as Al content increased. But for BCC phase, the vibrational entropy decreased monotonically as Al content increased. The different behavior in vibrational entropy shows different effect of Al addition on atomic vibrations in FCC and BCC structure. It can be proved that the harmonic vibrational entropy defined in Eq. 2.2 is negatively correlated to each vibrational frequency ν_i. Therefore, the decrease in vibrational entropy of BCC phase indicates that Al increased the vibrational frequency, *i.e.* stiffened the bonds between atoms. However, in FCC phase, this stiffening effect is only valid when $c_{Al} < 0.2$ ($x < 1.0$). Further addition in Al softened the bonds in Al$_x$CoCrFeNi instead of stiffening them.

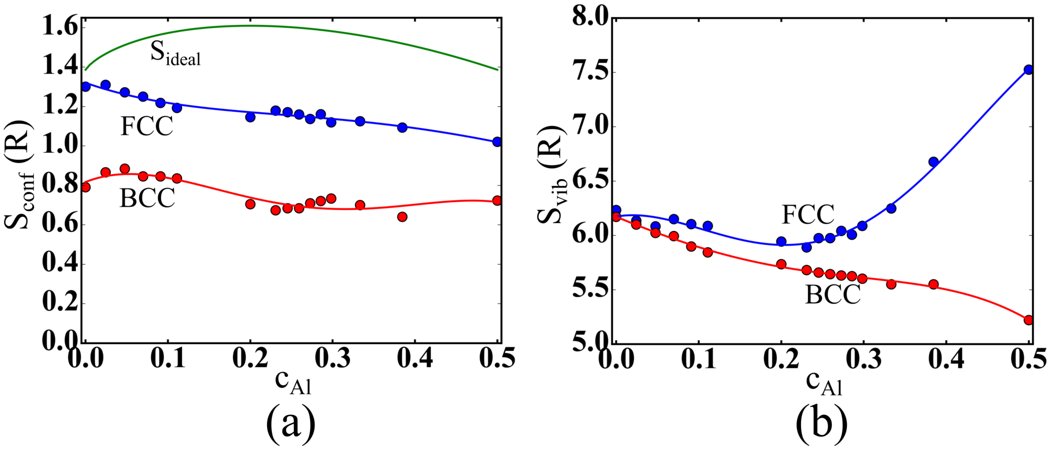

Figure 4.2: The (a) configurational and (b) vibrational entropy of Al$_x$CoCrFeNi alloys. The mole fraction of Al is calculated by $c_{Al} = x/(x+4)$.

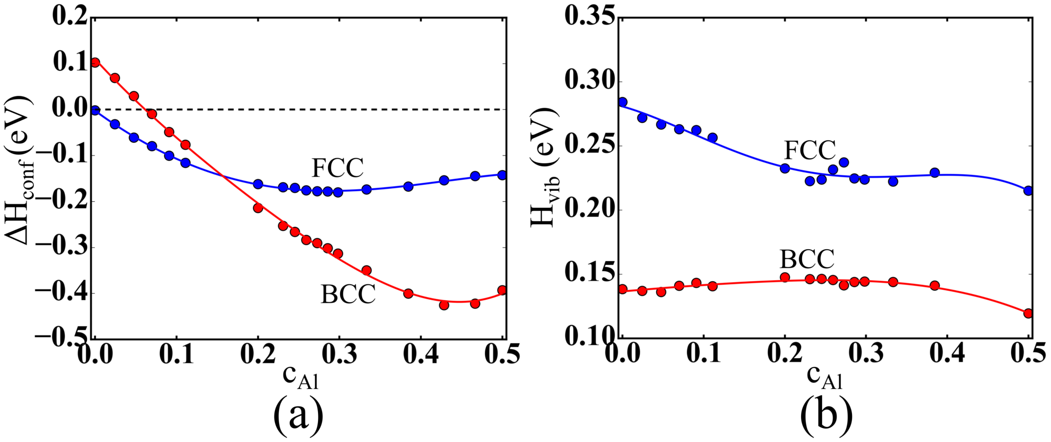

Figure 4.3: (a) The configurational enthalpy of mixing and (b) the vibrational enthalpy of Al_xCoCrFeNi alloys. The mole fraction of Al is calculated by $c_{Al} = x/(x + 4)$.

Both the configurational and vibrational entropy of FCC phase are greater than that of BCC phase. Thus the entropy of Al_xCoCrFeNi alloys tends to stabilize the FCC phase. The enthalpy, however, has a different effect. Figure 4.3 shows that the configurational enthalpy of mixing and the vibrational enthalpy of Al_xCoCrFeNi alloys. The configurational enthalpy of mixing reduced as Al content increased. The reducing effect is much stronger in BCC phase so that the BCC phase is stabilized at Al-rich end. For the vibrational part, the enthalpy of BCC phase is always lower than that of FCC phase by ~ 0.1 eV. It seems that the thermal motion of atoms destabilizes a close-packed structure, such as FCC structure, more than an open structure, such as BCC structure.

4.3 FCC TO BCC PHASE TRANSITION OF $\mathbf{Al_X}$CoCrFeNi ALLOYS

With the calculated enthalpy and entropy, the FCC to BCC phase transition in Al_xCoCrFeNi alloys has been investigated. An excess free energy of Al_xCoCrFeNi alloys was defined as suggested in Ref. [12], *i.e.*

$$\Delta G = G(c_{Al}) - (1 - 2c_{Al})G^{\mathrm{FCC}}(0) - 2c_{Al}G^{\mathrm{BCC}}(0.5) \tag{4.1}$$

where c_{Al} is the mole fraction of Al, and $G^{\mathrm{FCC}}(0)$ and $G^{\mathrm{BCC}}(0.5)$ are the free energy of FCC CoCrFeNi alloy and BCC $\mathrm{Al}_{4.0}$CoCrFeNi alloy respectively. The curve of this excess free energy for Al_xCoCrFeNi alloys in both BCC and FCC phases were plotted in Figure 4.4, and the common tangent was used to determine the boundary of the FCC-BCC duplex region in which FCC and BCC are in equilibrium with each other. In the case shown in Figure 4.4(a), only the configurational effect was considered. The FCC-BCC duplex region was found to be between $x = 0.36$ and $x = 2.11$. This range is similar to what has been found in DFT [12] and CALPHAD [13] calculations, whose lower bound is close to, but the upper bound is much higher than the experimental value [14]. However, in the case shown in Figure 4.4(b), the vibrational effect has been added in. The boundary of the FCC-BCC duplex region becomes $x = 0.21$ and $x = 1.08$. The upper boundary is largely reduced and is much closer to the experimental value of 0.7. This shows that the vibrational effect is important to determining the relative phase stability of Al_xCoCrFeNi and cannot be ignored.

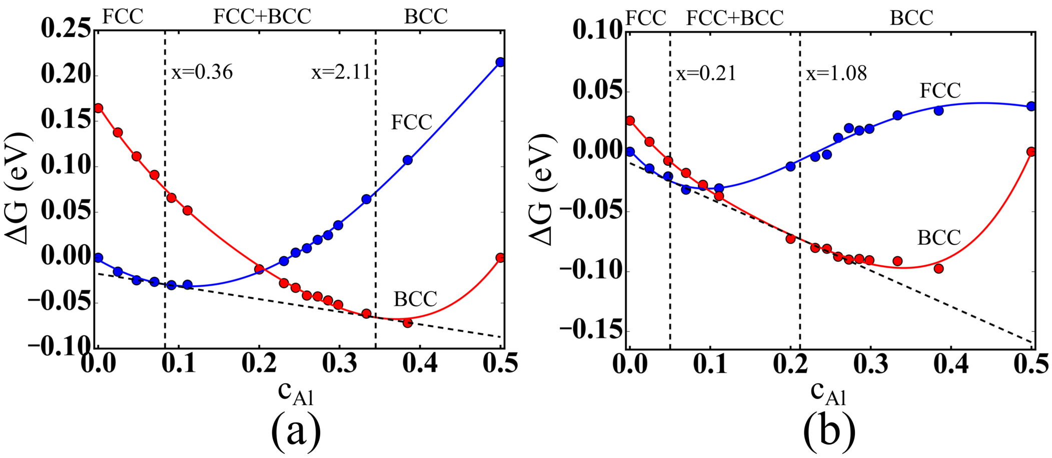

Figure 4.4: The excess free energy (a) with configurational effect and (b) with both configurational and vibrational effect of Al_xCoCrFeNi alloys. The mole fraction of Al is calculated by $c_{Al} = x/(x+4)$.

This dramatic change in the upper boundary of the FCC-BCC duplex region is a result of the destabilization of FCC phase caused by the atomic vibration. As discussed in section 4.2, FCC phase is stabilized by the vibrational entropy but destabilized by the vibrational enthalpy. In the interested FCC-BCC duplex region ($0 < x < 2$), the vibrational entropy of FCC phase is in general greater than that of BCC phase by ~ 0.3 R. At 1373 K, this difference downshifted the free energy curve of FCC phase by ~ 0.03 eV. However, the vibrational enthalpy of FCC is in general greater than that of BCC phase by ~ 0.1 eV. Therefore, the net effect of vibration is to upshift the free energy curve of FCC phase by ~ 0.06 eV, which moves the upper boundary from $x = 2.11$ to $x = 1.08$.

It has been mentioned in section 4.1 that the prediction of quaternary BCC alloys from the MEAM potential is higher than the prediction from DFT calculations. Moreover, two phases have been found in the BCC model as discussed in section 4.4. The interface between these two phases may not be fully relaxed due to the limited size of the simulation cell. Therefore, it is expected that the free energy of real BCC alloys should be lower than the value presented in Figure 4.4, which may further decrease the upper boundary of the FCC-BCC duplex region. These errors will quantitatively change the compositional boundary of the FCC-BCC duplex region. However, the qualitative picture that FCC is stable at low Al concentration, and BCC is stable at high Al concentration will not be changed. These results show that the FCC to BCC phase transition caused by Al addition is mainly controlled by the configurational enthalpy and entropy. But the non-configurational enthalpy and entropy also have an important effect on the compositional boundary of the FCC-BCC duplex region.

4.4 ORDERING EFFECT IN $\mathbf{Al_X}$CoCrFeNi ALLOYS

As mentioned in section 2.1.2, atomic ordering can be used to validate the entropy evaluation scheme developed in this study. Therefore, the atomic ordering effect in Al_xCoCrFeNi alloys has been investigated and compared them to experiments. The ordering effects in four example alloys have been investigated, namely, FCC $Al_{0.1}$CoCrFeNi alloy for FCC region, BCC $Al_{2.0}$CoCrFeNi alloy for BCC region, and FCC $Al_{0.3}$CoCrFeNi and BCC $Al_{1.0}$CoCrFeNi alloy for the FCC-BCC duplex region. These four alloys can all be found in experiments. The simulated XRD pattern of these four alloys are given in Figure 4.5. These patterns are calculated by assuming the atomic structure of the alloys to be the periodic repetition of the equilibrium supercell obtained by MC simulations. The full width at half maximum was set to 0.1° for each peak. The XRD pattern of Ni, Cr and ordered $AlNi_3$ ($L1_2$) and AlCo (B2) alloy are given as references. It is clear that no $L1_2$ type LRO can be detected in FCC alloys of $Al_{0.1}$CoCrFeNi and $Al_{0.3}$CoCrFeNi, while a B2 type ordering exists in BCC alloys of $Al_{1.0}$CoCrFeNi and $Al_{2.0}$CoCrFeNi. This is consistent with experiments that Al_xCoCrFeNi alloys in FCC phase are solid solutions while AlNi enriched B2 precipitates are found in BCC phase [10, 24, 11]. In addition, the equilibrium atomic structure of FCC $Al_{0.1}$CoCrFeNi and BCC $Al_{1.0}$CoCrFeNi alloy are given in Figure 4.6. Similar to the XRD pattern, no LRO can be seen in the atomic structure of FCC $Al_{0.1}$CoCrFeNi alloy. However, the ordered B2 structure with Al and Fe on one sublattice and Ni and Co on the other is dominating in the atomic structure of BCC $Al_{1.0}$CoCrFeNi alloy. Besides, a Cr and Fe enriched phase can also be seen in Figure 4.6(b), which is also consistent with experiments [24, 37].

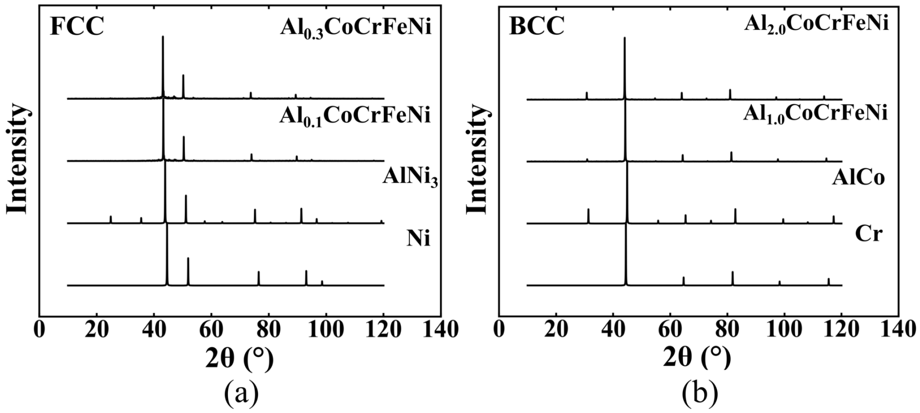

Figure 4.5: The simulated XRD pattern of FCC $Al_{0.1}CoCrFeNi$, FCC $Al_{0.3}CoCrFeNi$, BCC $Al_{1.0}CoCrFeNi$ and BCC $Al_{2.0}CoCrFeNi$ alloy. The simulated XRD pattern of Ni, Cr, $AlNi_3$ ($L1_2$) and AlCo (B2) are given as references.

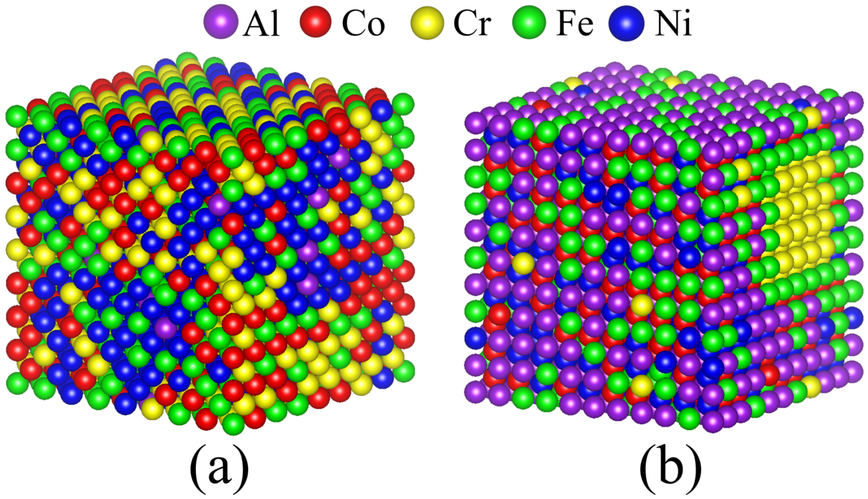

Figure 4.6: The equilibrium atomic structure of (a) FCC $Al_{0.1}CoCrFeNi$ and (b) BCC $Al_{1.0}CoCrFeNi$ alloy. For the visualization purpose, the structures without thermal motion are given here.

The B2 phase in stable BCC $Al_xCoCrFeNi$ ($x \geq 1.0$) alloy was investigated by checking the element distribution in the 1NN and 2NN sites of Al. Figure 4.7 shows the average occupation possibility of each element in the 1NN sites of Al as a function of Al content. It shows that the 1NN sites of Al in $Al_{1.0}CoCrFeNi$ alloy were occupied by Ni ($\sim 55\%$) and Co ($\sim 45\%$), while the 2NN sites were occupied by Al ($\sim 60\%$) and Fe ($\sim 40\%$). This agrees with the experimental finding that the atomic structure of this B2 phase is that Al and Fe on one sublattice and Ni and Co on the other. [37, 54] Clearly, this partially ordered structure explains the low configurational entropy of BCC $Al_xCoCrFeNi$ alloys. With the increasing of Al content, Fe moved from the 2NN site to the 1NN site of Al. Then in $Al_{4.0}CoCrFeNi$ alloy, the Cr-Fe enriched phase was absorbed into the B2 phase, and a B2 type structure with Al on one sublattice and Co, Cr, Fe and Ni on the other is formed. This trend is consistent with the phase diagram and calculated enthalpy of formation of B2 phase for Al-containing binary alloys. B2 phase can be found in the phase diagram of Al-Ni [52], Al-Co [64] and Al-Fe [63], while equiatomic Al-Cr alloy separates into Al_8Cr_5 intermetallic compound and BCC Cr-Al solid solution at 1373 K [154]. In addition, Table 4.1 shows that the B2 phase of AlNi and AlCo has large negative enthalpy of formation, while the enthalpy of formation of AlFe in B2 phase is about a half of that of AlNi and AlCo. On the contrary, the enthalpy of formation of AlCr alloy in B2 phase is close to 0. Thus when Al added to CoCrFeNi alloy, Ni and Co were first attracted by Al to form B2 phase, while the left Fe and Cr form BCC solid solution. With the addition of Al content, all the Ni and Co atoms formed B2 phase with Al. Then Fe start to form B2 phase with excess Al atoms. Finally, when all the Fe atoms formed B2 phase with Al, the excess Al atoms start to form bonds with Cr atoms. A pseudo binary B2 compound is formed between Al and (Co, Cr, Fe, Ni).

Similar Al-induced ordering has also been found in the stable FCC $Al_xCoCrFeNi$ ($x \leq 0.3$) alloy. Figure 4.8 shows the average possibility of a first-nearest-neighboring lattice site of an atom occupied by a specified element in CoCrFeNi and $Al_{0.3}CoCrFeNi$ alloy in their equilibrium state. For CoCrFeNi alloy, the near 25% occupancy probability for each element pair is an indication of near-ideal solution. Meanwhile, the formation of excess Co-Cr and Ni-Fe nearest-neighboring pairs were also found in Figure 4.8(a), which explains the 0.085 R discrepancy in configurational entropy between CoCrFeNi alloy and ideal solution. This

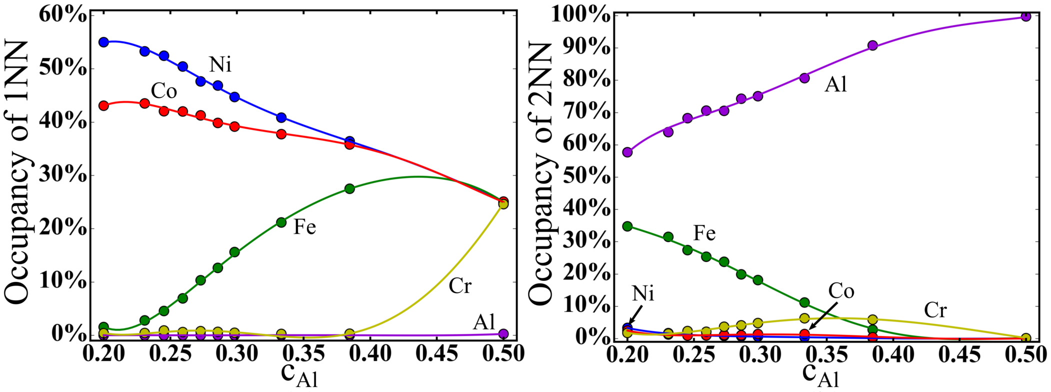

(a) (b)

Figure 4.7: The average occupation possibility of Al, Co, Cr, Fe and Ni at the first-nearest-neighboring sites of Al in $Al_xCoCrFeNi$ ($x \geq 1.0$) alloys. The mole fraction of Al is calculated by $c_{Al} = x/(x+4)$.

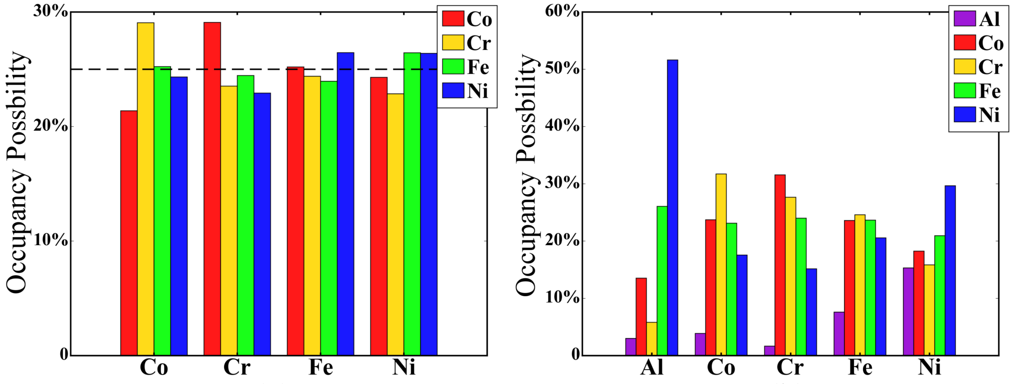

(a) (b)

Figure 4.8: The average possibility of a first-nearest-neighboring lattice site of an atom occupied by a specified element in the equilibrium CoCrFeNi and $Al_{0.3}CoCrFeNi$ alloy in FCC phase.

discrepancy becomes greater when Al was added into the alloy. Large number of Ni atoms was attracted to Al in $Al_{0.3}$CoCrFeNi alloy as shown in Figure 4.8(b), which can be viewed as a precursor for nucleating Al-Ni enriched phase.

Furthermore, the lattice mismatch in Al_xCoCrFeNi alloys was studied by calculating the average bond length between each element pair. In FCC CoCrFeNi alloy, the shortest and longest bond were found to be the Co-Fe and Co-Cr bond, which have an average length of 2.448 Å and 2.547 Å respectively. When Al is added in, *e.g.* in $Al_{0.3}$CoCrFeNi, the shortest bond was found to be still the Co-Fe bond with the same bond length. But the longest bond became the Al-Co bond with an average bond length of 2.617 Å. This corresponds to an enhancement of the lattice mismatch from 4.0% to 6.9%. In BCC phase, however, Al addition reduced the lattice mismatch from 7.4% of $Al_{1.0}$CoCrFeNi to 2.8% of $Al_{4.0}$CoCrFeNi alloy. This is because that the shortest bond length increased from 2.467 Å of the Fe-Cr bond in $Al_{1.0}$CoCrFeNi alloy to 2.543 Å of the Al-Fe bond in $Al_{4.0}$CoCrFeNi alloy. Therefore, the formation of B2 type structure not only lowered the configurational entropy, but also reduced the lattice mismatch by minimizing the Al-Al bond and the bonds between transition metals.

5.0 RESULTS AND DISCUSSIONS: VACANCY DIFFUSION IN α-Al_2O_3

5.1 CRYSTAL STRUCTURE OF α-Al_2O_3

In α-Al_2O_3, as shown Figure 5.1, O atoms are arranged in a HCP lattice while Al atoms occupy 2/3 of the possible octahedral sites. The DFT calculations gave the optimized lattice parameters for the hexagonal unit cell of α-Al_2O_3 to be a=4.81 Å and c=13.31 Å, the optimized internal parameter of Al atoms to be u=0.352, and the optimized internal parameter of O atoms to be v=0.306. These results are consistent with previous theoretical predictions [155] and experimental measurements [156].

It has been well-recognized that the energetics of atomic diffusion processes is closely related to local atomic structures. So the local atomic structures of bulk alumina crystal has been examined. In bulk α-Al_2O_3 (shown in Figure 5.2), the O atom lies at the center of a tetrahedron whose four vertices are Al atoms and the Al atom lies at the center of an octahedron whose six vertices are occupied by O atoms. It notes that the distance between the central O (or Al) atoms to their neighboring Al (or O) atoms are not always equal in alumina crystal. The DFT calculations showed that the half of the Al-O bonds have bond length of 1.87 Å and the other half have slightly longer bond length of 1.99 Å in α-Al_2O_3. Moreover, the adjacent Al-O bonds form an angle of about 110° around the O atom and form an angle of about 90° around the Al atom.

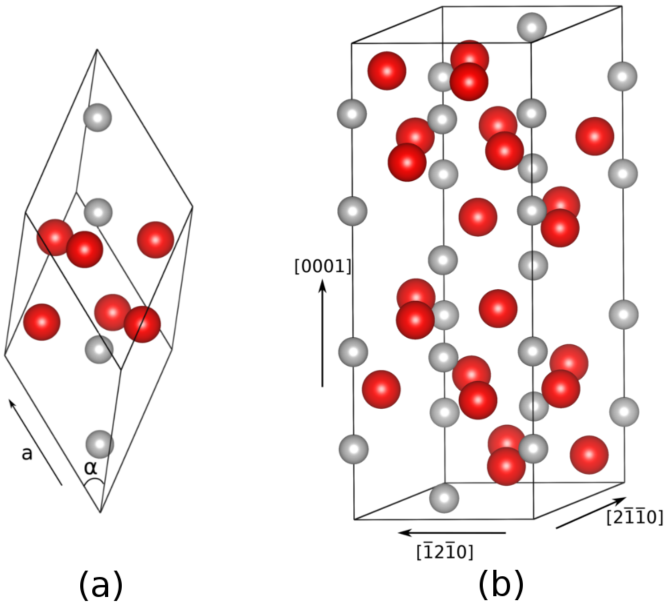

Figure 5.1: (a) Primitive unit cell and (b) conventional hexagonal unit cell of the crystal structure of α-Al_2O_3. In the figure, gray balls represent Al atoms and red balls represent O atoms.

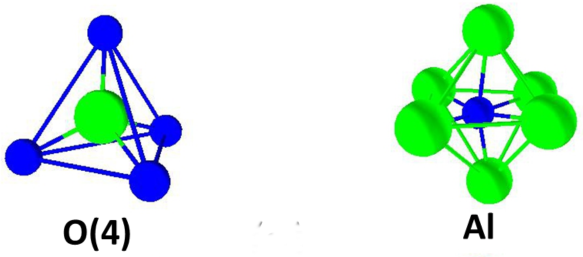

Figure 5.2: Local atomic structures showing the relative positions of the central O (or Al) lattice site and its nearest-neighboring Al (or O) lattice sites in the relaxed bulk α-Al_2O_3. Blue balls represent Al lattice sites and green balls represent O lattice sites.

5.2 VACANCY FORMATION ENERGY IN BULK ALUMINA

The formation energy of all the vacancies is presented in Table 5.1. The dependence of the formation energy on the Fermi energy and the chemical potential change of oxygen is given explicitly. It shows that the vacancy formation energy is a linear function of $\Delta\mu_{\mathrm{O}}$ since only mono-vacancies are considered here. It is suggested that the partial pressure of oxygen through out the protective alumina scale changed from 0.2 atm at the gas-oxide interface to 10^{-31} atm at the oxide-metal interface [157]. This corresponds to a change of about -3.9 eV in $\Delta\mu_{\mathrm{O}}$. Therefore, the concentration of O vacancy is much greater near the oxide-metal interface than the gas-oxide interface while the concentration of Al vacancy has an opposite trend. It is anticipated that the O diffusion is dominating near the oxide-metal interface while Al diffusion is dominating near the gas-oxide interface. So the dominating diffusion mechanism must have switched somewhere in the middle of the alumina scale, at which the partial pressure of oxygen has an intermediate value.

Table 5.1: Calculated formation energy (in eV) of the vacancies in different charge states. The dependence on the chemical potential change of oxygen $\Delta\mu_O$ and the Fermi energy ϵ_F is given explicitly. $\Delta\mu_O$ is calculated by $\frac{1}{2}\left[\Delta\mu_{\mathrm{O_2(g)}}(T) + k_BT\ln\frac{p_{\mathrm{O_2}}}{p^0}\right]$ and ϵ_F is taken VBM as zero.

O vacancy		Al vacancy	
Charge	$\Delta E_f(eV)$	Charge	$\Delta E_f(eV)$
0	$7.33 + \Delta\mu_{\mathrm{O}}$	0	$7.33 - 1.5\Delta\mu_{\mathrm{O}}$
+1	$4.88 + \Delta\mu_{\mathrm{O}} + \epsilon_F$	−1	$4.00 - 1.5\Delta\mu_{\mathrm{O}} - \epsilon_F$
+2	$2.19 + \Delta\mu_{\mathrm{O}} + 2\epsilon_F$	−2	$4.82 - 1.5\Delta\mu_{\mathrm{O}} - 2\epsilon_F$
		−3	$6.31 - 1.5\Delta\mu_{\mathrm{O}} - 3\epsilon_F$

Table 5.1 also shows that the vacancy formation energy is linearly dependent on the Fermi energy ϵ_F with the slope equal to the charge of the vacancy. Figure 5.3 shows the most stable charge state of vacancies when ϵ_F changes from VBM to CBM. Here the chemical

potential of oxygen is set to -5.69 eV, which corresponds to $T = 1300$ K and $p_{O_2} = 0.2$ atm. For O vacancies, V_{O}^{0} and V_{O}^{2+} are stable when ϵ_F is greater and less than 2.58 eV respectively. V_{Al}^{0}, V_{Al}^{1-}, V_{Al}^{2-} and V_{Al}^{3-} are stable when ϵ_F is from 0.0 eV (*i.e* VBM) to 0.25 eV, from 0.25 eV to 0.82 eV, from 0.82 eV to 1.49 eV, and greater than 1.49 eV, respectively. The dependence of the vacancy formation energy on ϵ_F reflects the influence of the charge carrier type in alumina on the charge state of the vacancies. If electrons are the majority charge carrier, V_{O}^{0} and V_{Al}^{3-} are the most favored vacancies. Otherwise, if holes are dominating, V_{Al}^{2-}, V_{Al}^{0} and V_{Al}^{1-} are more likely to occur.

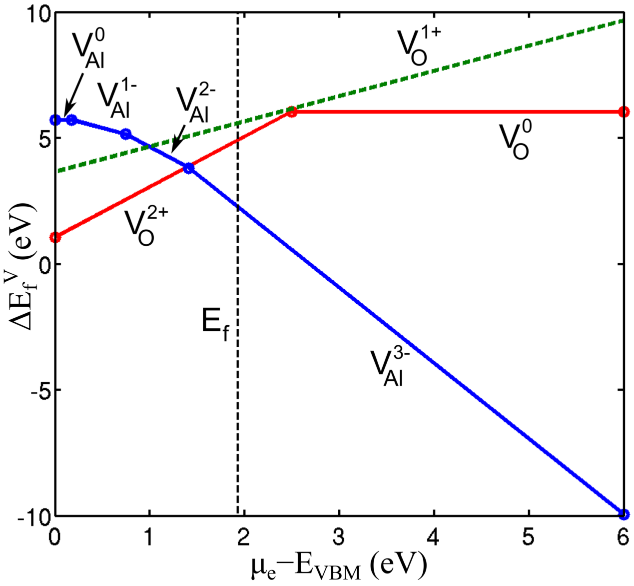

Figure 5.3: Formation energy of the most stable vacancy as a function of chemical potential of electron, μ_e. The dashed green line shows the formation energy of the unstable V_{O}^{1+}. The chemical potential of oxygen is chosen to be -5.69 eV, which corresponds to $T = 1300$ K and $p_{O_2} = 0.2$ atm. The vertical line denotes the Fermi energy of intrinsic α-Al_2O_3 at this condition.

It should be pointed out that the calculated stable range for each vacancy has only qualitative meaning. Because of the SIE in DFT calculations, the predicted band gap of α-Al_2O_3 (~ 6 eV) is much smaller than the experimental range ($8.5 \sim 10$ eV) [158, 159, 160].

This large band gap error leads to an underestimation of the position of the defect levels locating in the band gap. Therefore, the formation energy of V_{O}^{0}, V_{O}^{1+}, V_{Al}^{1-}, V_{Al}^{2-} and V_{Al}^{3-} is underestimated for that there are electrons filled in the defect levels of these vacancies (see section 5.3). It is anticipated that V_{O}^{2+} is stable in a wider range of ϵ_F while the stable range of V_{Al}^{3-} is narrower than the reported value.

As mentioned in section 3.3.2, the Fermi energy of intrinsic α-Al_2O_3 can be determined at a certain temperature and oxygen partial pressure. At an example condition of T=1300 K and p_{O_2}=0.2 atm, the Fermi energy is determined to be 1.93 eV above VBM. Under this condition, V_{Al}^{3-} is the most stable Al vacancy with a formation energy of 2.24 eV while the most stable O vacancy is V_{O}^{2+} with a formation energy of 4.91 eV.

5.3 MIGRATION ENERGY FOR VACANCY DIFFUSION IN BULK ALUMINA

Referencing to the equilibrium structure of α-Al_2O_3 crystal (show in Figure 5.1), Multiple elementary diffusive jumps have been identified for O and Al atoms to diffuse in bulk alumina through vacancy-atom exchange mechanism. As shown in Figure 5.4(a), there are two types of O elementary diffusive jumps (jump O_1-O_2 and jump O_3-O_4) in the (0001) plane and two types of elementary diffusive jumps (jump O_1-O_3 and jump O_1-O_4) connecting the two (0001) planes (*i.e.* along [0001] direction). All the other long-range diffusive paths for O atom in alumina can be attained by combining these four elementary jumps. In Figure 5.4(b)-(e), the minimum energy path (marked in arrows) and transition state (denoted with a red ball) of O lattice diffusion along the four elementary diffusive jumps were plotted, respectively. In all the starting and ending positions of the four jumps, the O atom has four nearest neighboring Al atoms and thus be four-fold coordinated. However, the migrating O atom would be four-fold coordinated in the transition state of jump O_1-O_2, three-fold coordinated in the transition state of jump O_1-O_3, and two-fold coordinated in the transition state of jump O_1-O_4 and O_3-O_4. Compared to the migration energy in Table 5.2, it appears that

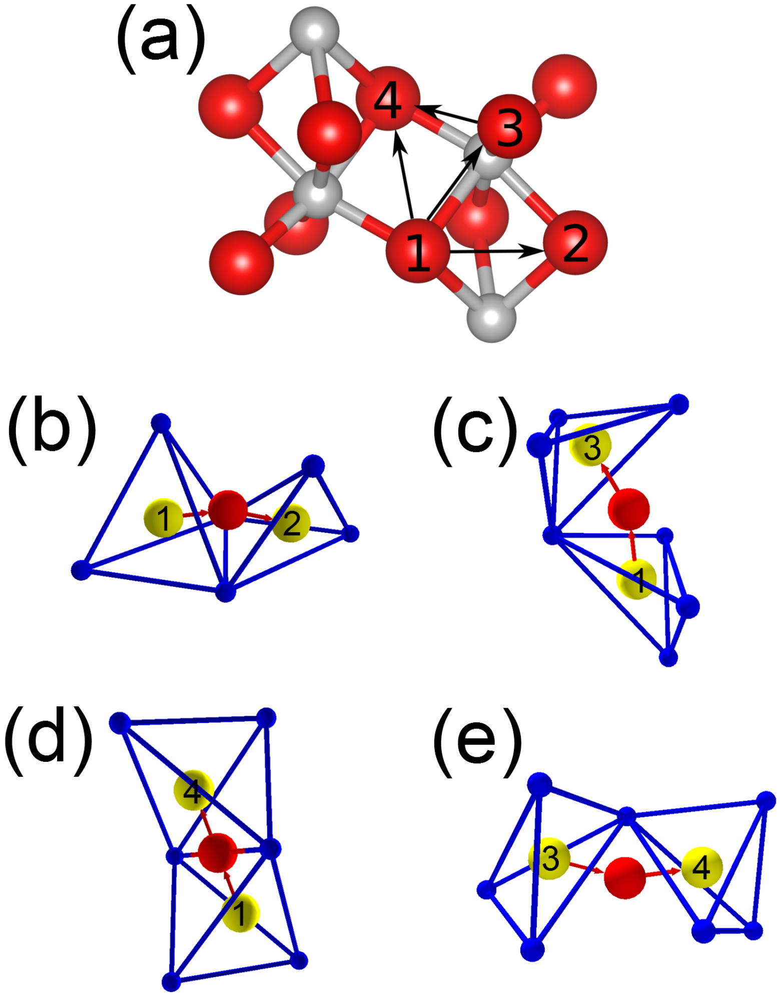

Figure 5.4: (a) Schematics of four elementary O diffusive jumps in bulk α-Al_2O_3 on the $(1\bar{2}10)$ projection of the crystal lattice. Gray balls represent Al atoms, red balls represent O atoms, and black arrows delineate various vacancy-O atom exchange. Local atomic structures of the migrating O atom are depicted in (b) for jump O_1-O_2, in (c) for jump O_1-O_3, in (d) for jump O_1-O_4 and in (e) for jump O_3-O_4. In (b)-(e), yellow balls are used to mark the initial and final positions of the migrating O atom, red balls mark the location of the migrating O atom in the transition states, red arrows indicate the direction of the diffusive jumps, and blue balls represent surrounding Al lattice sites.

the coordination number of the migrating O atom in the transition state is correlated with the calculated migration energy of the diffusive jumps. Namely, the higher the coordination number of O in the transition state, the lower the migration energy of the diffusive jump.

Table 5.2: Calculated migration energy (in eV) for charged O and Al vacancy diffusion in α-Al_2O_3 lattice. For the Al_2-Al_4 and Al_3-Al_4 diffusion paths, the migration energies for two diffusion segments are present separately.

O vacancies	O_1-O_2	O_1-O_3	O_1-O_4		O_3-O_4	
V_{O}^{0}	3.58	4.11	4.67		5.03	
V_{O}^{1+}	2.07	2.82	3.07		3.66	
V_{O}^{2+}	0.90	1.81	1.73		2.65	
Al vacancies	Al_1-Al_2	Al_1-Al_3	Al_2-Al_4		Al_3-Al_4	
			Step 1	Step 2	Step 1	Step 2
V_{Al}^{0}	1.80	2.05	1.56	1.61	1.93	0.32
V_{Al}^{1-}	1.73	2.04	1.49	1.65	1.87	0.31
V_{Al}^{2-}	1.66	1.96	1.30	1.68	1.74	0.27
V_{Al}^{3-}	1.55	1.76	1.02	1.77	1.56	0.25

For Al lattice diffusion in α-Al_2O_3, there are also four elementary diffusive jumps as shown in Figure 5.5(a): jump Al_1-Al_2 is a jump between the two Al atoms locating in the two neighboring (0001) layers; jump Al_1-Al_3 is a jump along [0001] direction between the two Al atoms locating in the (0001) layers separated by one O layer; jump Al_3-Al_4 is a jump tilted away from [0001] direction and between the two Al atoms locating in the (0001) layers separated by one O layer; and jump Al_2-Al_4 is a jump along [0001] direction between the two Al atoms locating in the (0001) layers separated by two O layers. The minimum energy pathway of these four Al elementary diffusive jumps is presented in Figure 5.5(b)-(e). DFT calculations indicated that both Al_1-Al_2 and Al_1-Al_3 diffusive jumps could be completed with one simple jump of Al atom from the starting position to the final position. However, jumps Al_2-Al_4 and Al_3-Al_4 involved an intermediate stable position and two simple jumps. It could

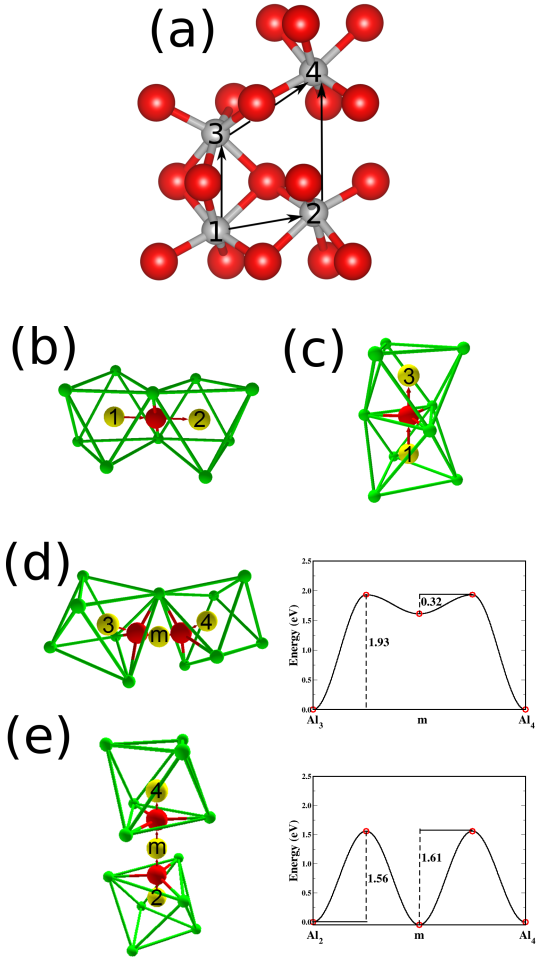

Figure 5.5: (a) Schematics of four elementary Al diffusive jumps in bulk α-Al_2O_3 on the $(1\bar{2}10)$ projection of the crystal lattice. In the figure, gray balls represent Al atoms, red balls represent O atoms, and black arrows delineate various vacancy-Al atom exchange paths. Local atomic structures of the migrating Al atom are depicted in (b) for jump Al_1-Al_2, in (c) for jump Al_1-Al_3, in (d) for jump Al_3-Al_4, and in (e) for jump Al_2-Al_4. In (b)-(e), yellow balls are used to mark the initial, intermediate (marked with symbol m), and final positions of the migrating Al atom, red balls mark the location of the migrating Al atom in the transition states, and red arrows indicate the direction of the diffusive jumps, green balls represent surrounding O lattice sites. Also, in (d) and (e), the calculated minimum energy path for the Al atom diffusion through jumps Al_3-Al_4 and Al_2-Al_4 have been plotted, respectively.

be seen in Figure 5.5(d) and 5.5(e) that there was a locally minimum-energy position (marked as m) between the two facing triangular facets of the two O octahedrons for the migrating Al atom to stay. Consequently, it involved two simple jumps (Al_3-m (or Al_2-m) and m-Al_4), whose transition state was the migrating Al atom lying at the center of the triangular facet of the O octahedron, to complete these two jumps. The coordination number of the transition state of jump Al_1-Al_2 is two, while for all the other jumps, the moving Al atom in transition state is three-fold coordinated. Unlike O vacancies, the migration energy of Al vacancies in Table 5.2 shows no dependence on the coordination number of Al in the transition state.

It is worth noting that the migration energy in Table 5.2 shows a clear dependence on the charge state of vacancies. For the four diffusive paths studied, the average migration energy for diffusion of V_{O}^{0} was computed to be 4.35 eV as compared to 1.77 eV for diffusion V_{O}^{2+}. Consequently, a significant enhancement (average diffusion migration energy reduced by 2.58 eV) has been predicted in O vacancy mobility when the charge of the O vacancy changes from 0 to +2 . The variation of the diffusion migration energy with the charge of the Al vacancy was found to be relatively small. Compared to the value of 1.55 eV for V_{Al}^{0}, the average diffusion migration energy was predicted to decrease by 0.03 eV for V_{Al}^{1-}, 0.11 eV for V_{Al}^{2-}, and 0.23 eV for V_{Al}^{3-}. Nevertheless, the vacancy diffusion in alumina crystal is strongly depends on the charge state of the vacancy involved.

This charge dependency can be explained by checking the electronic structure of α-Al_2O_3. The valence band of perfect alumina is just the O $2p$ band near the VBM whereas the conduction band is mainly composed of Al $3s$ and $3p$ bands. When vacancies are introduced to alumina, extra defect states could be observed inside the band gap. The defect state associated to O vacancy was located at 2.41 eV above VBM and composed of the 3s and 3p orbitals from the nearest-neighboring Al atoms (illustrated in Figure 5.6(a)-(b)). The defect state associated to Al vacancy was found to posit at 0.58 eV above VBM and composed of the 2p orbitals from the nearest-neighboring O atoms (illustrated in Figure 5.7(a)-(b)). Comparing the electronic structures of the O vacancy at its relaxed state (Figure 5.6(a)-(b)) and its transition state of jump O_1-O_2 (Figure 5.6(c)-(d)), it is noticed that the energy level of the defect state shifted up by 1.51 eV at the transition state accompanying to the spreading of defect electron density from one local Al tetrahedron to the two neighboring Al

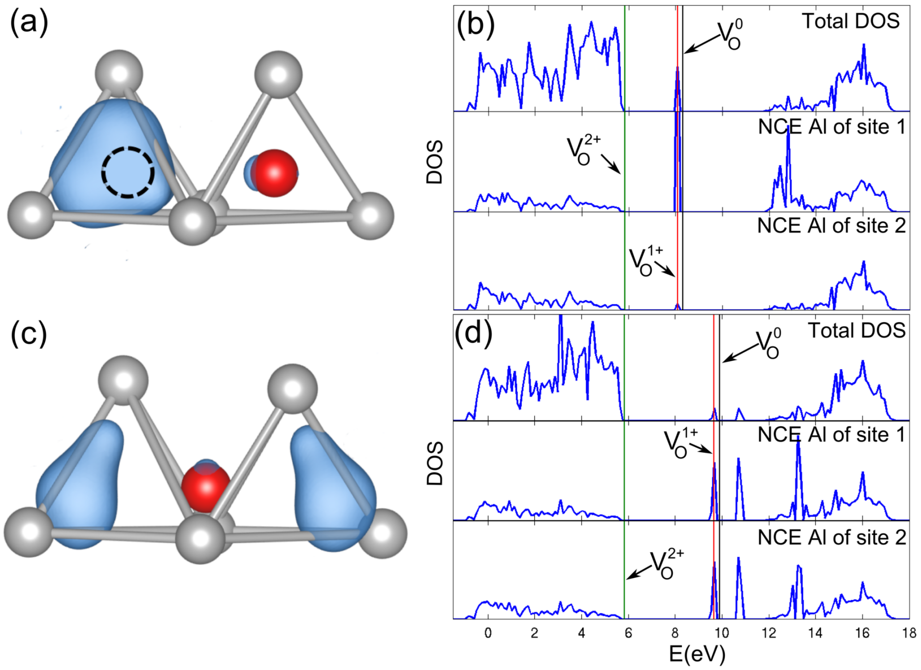

Figure 5.6: Isosurface (isovalue of 0.015) of electron density and calculated densities of states (DOS) associated to the defect state of O vacancy in α-Al_2O_3 at (a), (b) the relaxed state and (c), (d) the transition state of diffusive path O_1-O_2. The DOSs of Al, Al_I, and Al_{II} are those from all the six surrounding Al atoms, the two Al atoms adjacent to the relaxed O vacancy, and the two Al atoms farther away from the relaxed O vacancy.

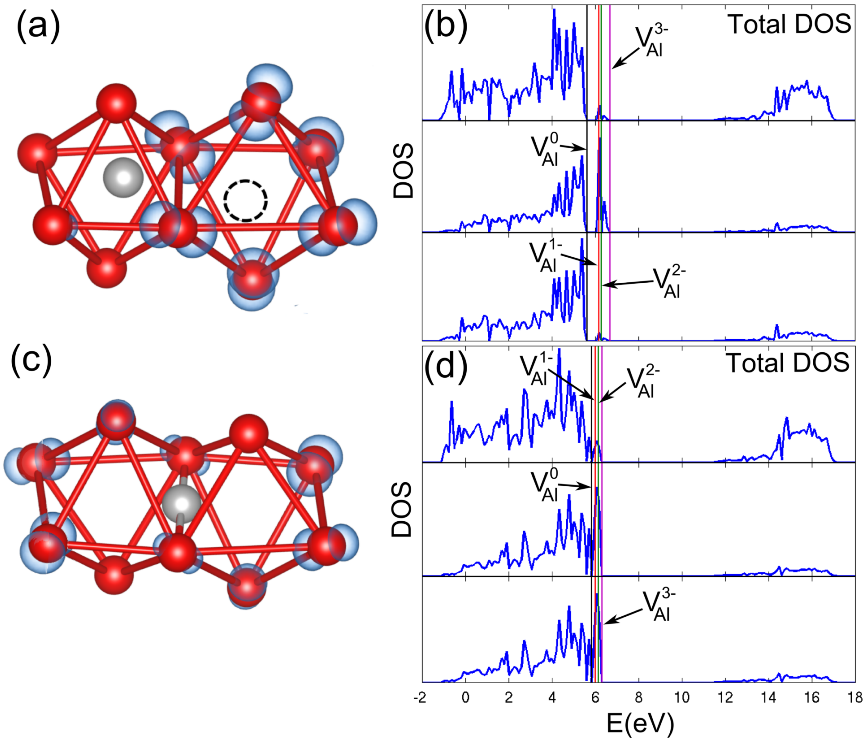

Figure 5.7: Isosurface (isovalue of 0.05) of electron density and calculated densities of states (DOS) associated to the defect state of Al vacancy in α-Al_2O_3 at (a), (b) the relaxed state and (c), (d) the transition state of diffusive path Al_1-Al_2. The DOSs of Al, O_I, and O_{II} are those from all the ten surrounding O atoms, the four O atoms adjacent to the relaxed Al vacancy, and the four O atoms farther away from the relaxed Al vacancy.

tetrahedrons. Examination of the other O vacancy diffusion paths yields similar results. It is apparent that the O vacancy diffusion through alumina crystal involves an upshift of the energy level of the defect state (composted of Al 3*s* and 3*p* bands) toward the conduction band of the crystal. Regarding to Al vacancy diffusion in α-Al_2O_3, Figure 5.7 shows that the energy level of the defect state (composted of O 2*p* band) actually shift down toward the valence band of the crystal at the transition state in which the defect electron density is evenly distributed between the two neighboring O octahedrons.

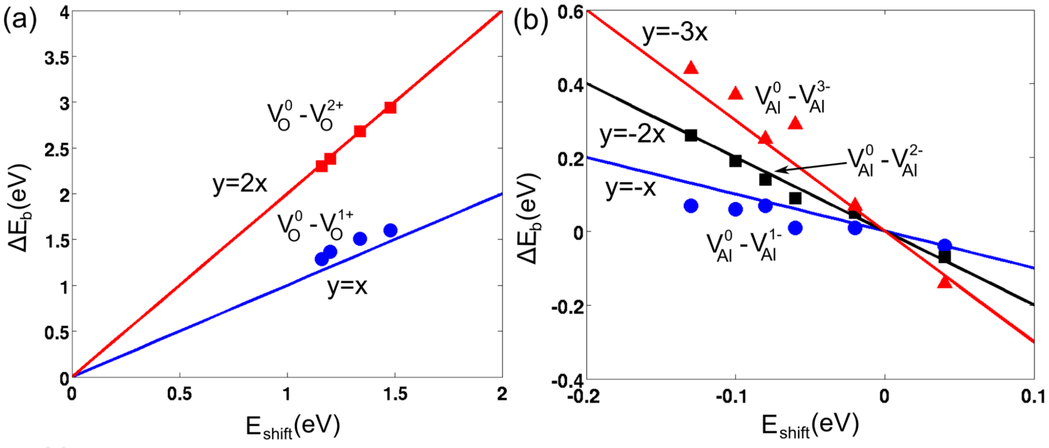

Figure 5.8: The calculated difference in migration energy for (a) O vacancies and (b) Al vacancies with different charges as a function of the energy shift (ΔE_{V}) of the defect state (with a single electron occupancy) for the corresponding diffusive paths. The dashed lines shows the theoretical prediction of the migration energy difference calculated by the product of the electron occupancy difference and the energy shift.

The migration energy for vacancy diffusion can be considered as the sum of the energy changes of the electrons occupying the valence band of the crystal and those of the electrons occupying the vacancy defect states in the diffusion process. For O vacancy, the charge induced relaxation happened mainly on nearest neighbor Al atoms, hence has limited effect on the valence band which is mainly contributed by O atoms. For Al vacancy, this relaxation is found to be small. Both of these imply that the energy change related to valence electrons of the crystal could be small. However, the electron occupancy on defect states would vary greatly with variations of the vacancy charge. For the O vacancy in alumina, the defect state is unoccupied for V_{O}^{2+}, singly occupied for V_{O}^{1+} and doubly occupied for V_{O}^{0} (as marked in Figure 5.6 (b),(d)). For the Al vacancy in alumina, the defect state contains no electron for V_{Al}^{0}, one electron for V_{Al}^{1-}, two electrons for V_{Al}^{2-}, and three electrons for V_{Al}^{3-} (as marked in Figure 5.7(b),(d)). Hence, the calculated migration energy difference between the vacancies with different charges should be approximately equal to a product of the electron occupancy difference in the defect state and the energy shift of the defect state for the same diffusive path. In Figure 5.8, the change in diffusion migration energy due the vacancy charge against the change in defect state energy level during the vacancy diffusion has been plotted. The dashed lines are the theoretical prediction of the migration energy difference calculated by the product of the electron occupancy difference and the energy shift. It shows that these two sets of data agree well with each other. Therefore, it has been uncovered in this study that the energy shift in the electronic defect state during diffusion is responsible for the observed charge-dependent vacancy migration energy in alumina.

Just as in the vacancy formation energy, SIE in DFT calculations also causes an error in the vacancy migration energy. However, this error has not been well understood yet. Indeed, the position of defect levels in the band gap has been underestimated. But this underestimation occurs both in the electronic structure of the transition state and the vacancy state. Therefore, it is expected that the error in the vacancy migration energy and the defect level shift is partially cancelled. In addition, there is another error in the evaluation of the defect level shift. This error is caused by the artificial dispersion of the defect levels which is a result of the limited size of the simulation cell [19]. The dispersion causes a trouble in locating the exact position of the defect levels. This dispersion effect is strong in the defect levels of Al vacancy. It could partially be the reason of the discrepancy between the calculated migration energy difference of the Al vacancies in different charge states and the theoretical prediction in Figure 5.8(b).

However, none of these errors would qualitatively change the picture of that, for most cases, the migration energy of the charged vacancy is lower than that of the neutral vacancy. This is because that the energy shift is a result of the charge redistribution around the vacancy site. As discussed in section 2.2.2, defect levels are introduced by the localized charges which distributed around the vacancy. When vacancy diffuses from one site to another, these extra charges redistributed. It can be seen in Figure 5.6 and 5.7 that these extra charges equally distributed near the original site and the destiny site at the transition state. This will cause a reduction in the depth of the potential well which is localized near the vacancy site. Therefore, it is anticipated that the defect level of oxygen vacancies moves up toward CB and the defect levels of aluminum vacancies move down toward VB during the migration. That is what has been found in most cases. However, this analysis is only valid if two vacancy sites of a diffusive path are located next to each other. When an intermediate state exists in the diffusive path such as Al_2-Al_4 and Al_3-Al_4, these extra charges near the vacancy are localized around neither the original site nor the destiny site in both the intermediate state and the transition state. Therefore, to which band edge the defect levels will shift during the vacancy migration from the intermediate state to the transition state is unknown. This explains the exception occurs in the second segment of the diffusive path Al_2-Al_4.

5.4 KINETIC MONTE CARLO SIMULATION OF DIFFUSIVITY

With the migration energy of individual diffusion paths, the diffusivity of O and Al in Al_2O_3 has been determined by performing Kinetic Monte Carlo (KMC) simulations [161]. Vibrational frequencies of both the vacancies and the transition states were used to provide the rates of each diffusion path. The rate of one diffusion path is determined by the harmonic approximation, *i.e.*

$$r = \frac{\prod_i \nu_i}{\prod_i \nu_i'} \exp\left(-\frac{\Delta E}{k_B T}\right) \tag{5.1}$$

where ν_i and ν_i' are the vibration frequencies of vacancies and transition states respectively, while ΔE is the migration energy of one single jump. As mentioned in section 5.3, there are two diffusion paths of Al vacancies, *i.e.* Al_2-Al_4 and Al_3-Al_4, in which an intermediate stable state exists. An effective diffusion rate was defined for these paths, *i.e.*

$$\frac{1}{r_{eff}} = \frac{1}{r_1} + \frac{1}{r_2} \tag{5.2}$$

where r_1 and r_2 are the diffusion rate of the first and the second segment of the diffusion path. The mean square displacements of atoms are used to evaluate the diffusivity in KMC simulations and this diffusivity is scaled by the equilibrium vacancy concentration to get the real diffusivity. The diffusivity of O and Al atoms through exchanging with charged vacancies in Al_2O_3 crystal in the temperature range of 1300 K to 1800 K were calculated. Then the relation between the diffusivity and the temperature was fitted to the Arrhenius' law to obtain the activation energy of diffusion. The activation energy for the O diffusion through exchanges with V_{O}^{0}, V_{O}^{1+} and V_{O}^{2+} were predicted to be 11.91 eV, 9.49 eV, and 7.21 eV, respectively. The activation energy for the Al diffusion through exchanges with V_{Al}^{0}, V_{Al}^{1-}, V_{Al}^{2-} and V_{Al}^{3-} were determined to be 4.76 eV, 3.57 eV, 2.98 eV, and 2.99 eV, respectively. In addition, the results indicated that the prefactor of the O diffusion through V_{O}^{2+} had a smaller value than through other possible charged O vacancies whereas the prefactor of the Al diffusion through V_{Al}^{3-} had the largest value among all the possible charged Al vacancies. In summary, it has been found that V_{O}^{+2} and V_{Al}^{3-} vacancies respectively led to the fastest diffusion of O and Al in alumina. In particular, our predicted activation energy (7.21 eV) and prefactor (3.27×10^{-4} m^2/s) for O diffusion through V_{O}^{2+} fall well into the range of experimental values summarized in Ref. [8]

5.5 Hf EFFECT ON Al VACANCY DIFFUSION IN BULK

The charge-dependent vacancy migration energy discussed in section 5.3 shows that the diffusivity of vacancies in α-Al$_2$O$_3$ can be tuned by changing the charge state of vacancy. However, the band gap of α-Al$_2$O$_3$ is very large, which makes it hard to change the charge state of a vacancy. Fortunately, there is another possible way to tune the migration energy of vacancies, that is, modifying the defect level shift during the vacancy migration.

The interaction between Al vacancy and substitution Hf atoms in bulk has also been investigated. As Hf is doped in Al$_2$O$_3$, V_{Al}^{3-} will be introduced to keep the charge neutrality by following equation [162]

$$2\mathrm{HfO}_2 + 4\mathrm{Al}_{\mathrm{Al}}^{0} \leftrightarrow 3\mathrm{Hf}_{\mathrm{Al}}^{1+} + V_{\mathrm{Al}}^{3-} + \mathrm{Al}_2\mathrm{O}_3 \tag{5.3}$$

Therefore, the number of $\mathrm{Hf}_{\mathrm{Al}}^{1+}$ is about 3 times of V_{Al}^{3-}. So one V_{Al}^{3-} has been put at the nearest neighbor site of $\mathrm{Hf}_{\mathrm{Al}}^{1+}$. It is found that the Al vacancy next to $\mathrm{Hf}_{\mathrm{Al}}^{1+}$ is still V_{Al}^{3-} and the binding energy is -1.70 eV, which indicates a strong binding between these two point defects. The binding energy is calculated by

$$\Delta E_b = E_{\mathrm{Hf}_{\mathrm{Al}}^{1+}+V_{\mathrm{Al}}^{3-}} + E_{perf} - E_{\mathrm{Hf}_{\mathrm{Al}}^{1+}} - E_{V_{\mathrm{Al}}^{3-}} \tag{5.4}$$

where $E_{\mathrm{Hf}_{\mathrm{Al}}^{1+}+V_{\mathrm{Al}}^{3-}}$, $E_{\mathrm{Hf}_{\mathrm{Al}}^{1+}}$ and $E_{V_{\mathrm{Al}}^{3-}}$ are the energy of the model contains the defect pair, single $\mathrm{Hf}_{\mathrm{Al}}^{1+}$, and single V_{Al}^{3-}, respectively, and E_{perf} is the energy of the model without any defect. Moreover, the migration energy of diffuse away from along the path Al$_1$-Al$_2$ is calculated. The migration energy is 1.93 eV comparing to the 1.55 eV without Hf. A detailed analysis of DOS shows that the energy shift of the defect states of the Hf doped model is 0.04 eV less than the energy shift without Hf. Since the energy shift of the defect states of Al vacancy is downward, this corresponds to an increasing in migration energy by 0.12 eV, which is 32%

of the total increasing in migration energy. Therefore, Hf not only modified the diffusion path of V_{Al}^{3-} geometrically, but also changed the electronic structure to make V_{Al}^{3-} harder to diffuse away. It is possible that this electronic structure modification also happens at the grain boundary of α-$\mathrm{Al_2O_3}$ which slows down the diffusion of Al.

5.6 STRUCTURE OF NEAR Σ11 GRAIN BOUNDARY OF α-$\mathrm{Al_2O_3}$

The Al vacancy diffusion in the near Σ11 grain boundary (GB) was investigated. This GB was modelled by Kenway model [163, 164, 165] with 180 atoms. In the Kenway model, the $(10\bar{1}\bar{1})$ plane of one grain is parallel to the $(10\bar{1}1)$ plane of the other. Therefore, the two axes of the surface supercell have been chosen to be along $[\bar{1}2\bar{1}0]$ and $[2\bar{1}\bar{1}1]$ direction for one grain and along $[\bar{1}2\bar{1}0]$ and $[2\bar{1}\bar{1}\bar{1}]$ direction for the other. With $[2\bar{1}\bar{1}1]$ direction of the former grain parallel to $[2\bar{1}\bar{1}\bar{1}]$ direction of the later grain, the GB model can be built without lattice mismatch. In the direction perpendicular to the GB plane, each grain has a thickness of 11.9 Å, which results in 90 atoms for each grain. The out most 12 atoms for each grain were kept in bulk structure during the relaxation and a vacuum layer of around 10 Å was added into the supercell to eliminate the interaction between the periodic images of the slab. The density of the k-point mesh used in all the GB calculations is $5 \times 5 \times 1$.

Though crystal orientation between two grains has been defined, there are still several internal degrees of freedom to be determined in the model. First is the possible termination of the $(10\bar{1}\bar{1})$ and $(10\bar{1}1)$ plane. Here, the most stable termination of these two surfaces reported in Ref. [165] has been used. The surface energy is calculated to be 2.10 $\mathrm{J/m^2}$ for $(10\bar{1}\bar{1})$ plane and 2.02 $\mathrm{J/m^2}$ for $(10\bar{1}1)$ plane. The former is very close to the 2.08 $\mathrm{J/m^2}$ reported in Ref. [165], but the later is greater than the reported 1.81 $\mathrm{J/m^2}$ by 0.21 $\mathrm{J/m^2}$, which is a result of the different energy cutoff used in two calculations.

The second internal degree of freedom is the relative displacement between two grains in the GB plane. To determine the relative displacement corresponding to the most stable structure, The energy of the GB with the relative displacement satisfying $\vec{R} = x\vec{a} + y\vec{b}$ has been calculated, where $\vec{a}$ and $\vec{b}$ are the two axes (along $[\bar{1}2\bar{1}0]$ and $[2\bar{1}\bar{1}1]$/$[2\bar{1}\bar{1}\bar{1}]$ direction respectively) of the supercell in the GB plane and x and y are running through 0, 0.25, 0.5 and 0.75. During the calculations, the atoms are only allowed to move in the normal direction of the GB plane. The resulting energy surface is given in Figure 5.9. By interpolating within

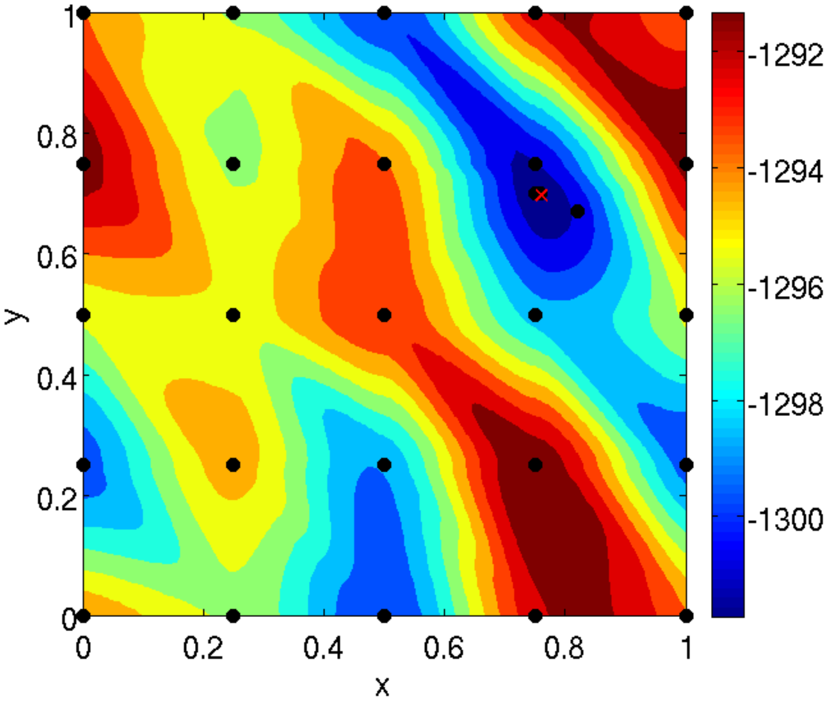

Figure 5.9: The energy of the GB as a function of the relative displacement between two grains. The distance between the two grains in the normal direction of the GB plane is 1 Å. The data points are marked by black dot and the global minimum was marked by the red cross.

these data points, the global minimum of this energy surface can be obtained. Then the energy of the global minimum can be used as new data point to refine the energy surface. The most stable structure was obtained when the global minimum determined by the new data set is the same as the one determined by the old data set. In this way, the displacement corresponding to the most stable structure was found at $x = 0.7$ and $y = 0.76$.

The third internal degree of freedom is the distance between the two grains in the normal direction of the GB plane. It has been found that the energy surface of relative displacement in the GB plane is insensitive to the distance between the two grains. Therefore, the equilibrium distance is determined by sampling different distances at the fixed displacement in the GB plane, *i.e.* $0.7\vec{a}+0.76\vec{b}$. In these calculations, the atoms are allowed to move in all directions and the equilibrium distance is found to be 0.86 Å between the two grains.

The most stable structure of the near $\Sigma 11$ GB is given in Figure 5.10. The formation energy of GB is calculated by

$$\Delta E_f^{\mathrm{GB}} = \frac{E_{\mathrm{GB}} - nE_{\mathrm{bulk}}}{A} - \sigma_{10\bar{1}\bar{1}}^{unrel} - \sigma_{10\bar{1}1}^{unrel} \tag{5.5}$$

where E_{GB} is the total energy of the GB slab, n is the number of atoms in the GB slab, *i.e.* 180, E_{bulk} is the energy per atom in bulk α-$\mathrm{Al_2O_3}$, A is the area of GB and $\sigma_{10\bar{1}\bar{1}}^{unrel}$ and $\sigma_{10\bar{1}1}^{unrel}$ are the surface energy of the unrelaxed $(10\bar{1}\bar{1})$ and $(10\bar{1}1)$ surface respectively. The formation energy of the most stable structure of the near $\Sigma 11$ GB is calculated to be 2.13 J/m^2. This formation energy is 0.58 J/m^2 lower than the GB formation energy reported in Ref. [165] calculated in the same sense.

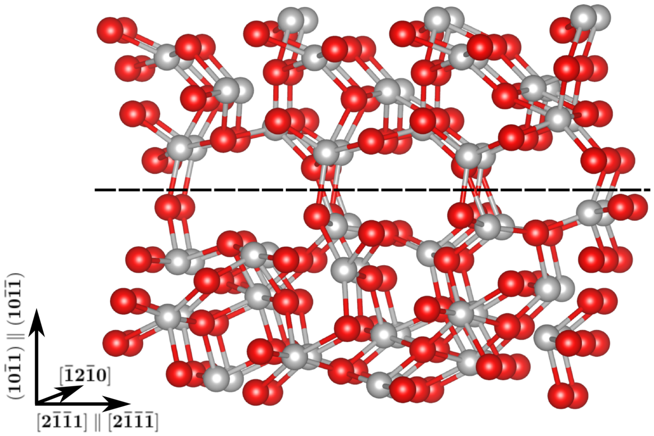

Figure 5.10: The equilibrium structure of the near $\Sigma 11$ GB. The Al and O atoms are represented by the gray and red balls respectively.

5.7 Hf EFFECT ON Al VACANCY DIFFUSION IN GRAIN BOUNDARY OF α-Al$_2$O$_3$

With the stable structure, the vacancy formation energy at the near Σ11 GB of α-Al$_2$O$_3$ has been investigated. 12 Al atoms has been identified near the GB plane, as shown in Figure 5.11. These Al atoms were removed one by one and the formation energy of the vacancy was calculated by

$$\Delta E_f = E_v - E_{\text{slab}} + \mu_{\text{Al}} \tag{5.6}$$

where E_v and E_{slab} is the energy of the GB model with and without an Al vacancy and μ_{Al} is the chemical potential of Al. Here, only the formation energy of neutral vacancy was considered for that the energy of charged slab is divergent respect to the vacuum thickness [1]. The formation energy of neutral Al vacancy at the example condition of $T = 1300$ K and $p_{O_2} = 0.2$ atm is given in Table 5.3. It shows that the most stable site of neutral Al vacancy is site 4.

Site 4 has two nearest GB sites, *i.e.* site 3 (2.99 Å) and 5 (2.96 Å). The segregation energy of Hf, which was calculated by the energy difference between the models with Hf at GB site and bulk site as denoted in Figure 5.11, was determined to be 0.11 eV and −0.16 eV for site 3 and 5 respectively. This shows that Hf tends to segregate to site 5 rather than site 3. Therefore, the migration energy of neutral Al vacancy from site 4 to site 3 was studied with and without Hf segregated to site 5.

The migration energy of neutral Al vacancy between site 4 and 3 was calculated to be 1.17 eV and 1.05 eV for forward (4 to 3) and backward (3 to 4) diffusion respectively. With Hf segregation, the migration energy for the forward and backward diffusion becomes 1.08 eV and 1.30 eV. Thus, when Al vacancy diffuse away from Hf, the migration energy is lowered by 0.09 eV. But when Al vacancy diffuse toward Hf, the migration energy is risen by 0.25 eV. This is a result of destabilizing of Al vacancy near Hf. With Hf occupying site 5, the energy difference between the vacancy at site 3 and site 4 changed from 0.12 eV to −0.22 eV. Therefore, unlike in the bulk where Al vacancies are attracted to Hf atoms, Al vacancies in GB are repelled from Hf atoms.

---

[1] VASP manual : http://cms.mpi.univie.ac.at/vasp/vasp/vasp.html

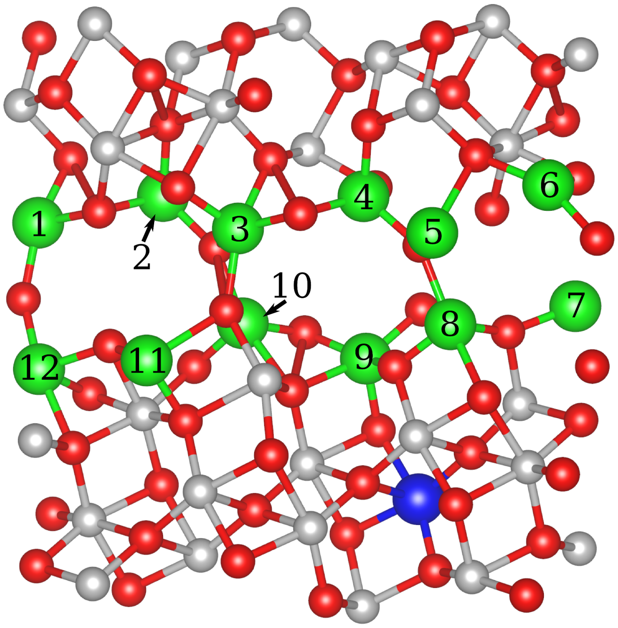

Figure 5.11: The 12 GB sites (green balls) used in vacancy calculations. The blue ball marks the bulk site used in calculations of Hf segregation.

Table 5.3: The formation energy (in eV) of Al vacancy to the 12 GB sites shown in Figure 5.11. The chemical potential of Al is chosen to be −4.30 eV at the example condition of $T = 1300$ K and $p_{O_2} = 0.2$ atm.

Site	1	2	3	4	5	6
ΔE_f	9.91	8.75	9.33	7.87	8.29	9.17
Site	7	8	9	10	11	12
ΔE_f	10.01	9.65	9.20	9.58	9.12	11.08

However, these results are valid for the neutral vacancy only. For intrinsic α-Al_2O_3, V_{Al}^{3-} is more likely to be the diffusion species. Though the charged slab cannot be handled by VASP, the correlation between the defect level shift and migration energy difference can be used to evaluate the migration energy of V_{Al}^{3-}. By defining the position of the defect levels to be the energy to which the integration of the density of states from the highest occupied energy is half of the total number of states in the defect levels, the level shift was determined to be −0.08 eV and −0.01 eV for the forward and backward vacancy diffusion without Hf segregation. With Hf segregation, the defect level shift was −0.04 eV (forward) and 0.03 eV (backward). For the vacancy diffusion without Hf, the defect levels were empty. But when Hf is added in, the defect levels were occupied by one electron for that Hf is tetravalent. Therefore, when the Al vacancy is V_{Al}^{3-}, the forward and backward migration energy become 0.93 eV and 1.02 eV without Hf segregation and 1.00 eV and 1.36 eV with Hf segregation. This indicate that Hf in GB can tune the defect level shift during the diffusion of V_{Al}^{3-}, which slows down the Al diffusion in α-Al_2O_3.

Again, the SIE and the dispersion error mentioned in section 5.3 could be important to the evaluation of the defect level shift during the vacancy migration. Moreover, there are *d*-electrons in Hf, whose behavior is not accurately described in DFT-GGA calculations [19]. Therefore, the Hf effect on the migration energy and the defect level shift of the bulk and grain boundary diffusion of Al vacancy still need more investigations. Nevertheless, these results show that doping in α-Al_2O_3 may change the diffusivity of Al vacancies through modifying the electronic structure during the vacancy migration.

6.0 CONCLUDING REMARKS

6.1 CONCLUSIONS

In this dissertation, atomistic simulation methods have been used to investigate the properties of two material systems, *i.e.* $Al_xCoCrFeNi$ HEAs and α-Al_2O_3. These two case studies demonstrated that atomistic simulation methods are efficient tools for materials researches. They can provide information, such as configurational and vibrational entropy, short range order in alloys and defect level shift during vacancy migration, that are hard to be measured in experiments. This information complements experimental results and improves our understanding in materials systems.

The specific conclusions of each case study are given below:

In the first case study, an atomistic simulation method has been developed for calculating the configurational and vibrational entropy of HEAs. This method combines the power of MEAM potential, MC simulation and TI method to calculate the thermodynamic properties of HEAs. For the testing purpose, the thermodynamic properties of $Al_xCoCrFeNi$ HEAs have been investigated. The results show that the developed method provides a reasonable estimation of the entropy in this quinary alloy system. The calculated free energy captured the FCC to BCC phase transition caused by Al addition in $Al_xCoCrFeNi$ HEAs. Particularly, it has been found that the FCC-BCC duplex region lies between $x = 0.36$ and $x = 2.11$ when only configurational entropy is considered. But with atomic vibrations included in, the region becomes between $x = 0.21$ and $x = 1.08$, which is much closer to the experimental range of $0.3 < x < 0.7$ [14]. This reveals that the configurational enthalpy and entropy determine the overall picture of the FCC to BCC transition caused by Al addition in $Al_xCoCrFeNi$ HEA system. But the vibrational enthalpy and entropy are also important to the quantitative prediction of the compositional boundary of the FCC-BCC duplex region. This effect of atomic vibrations may not be important at low temperature for that the vibrational entropy is small compared to the configurational entropy in this case. However, it is significant and cannot be ignored at high temperature such as 1373 K. In addition, there is still a gap in the upper boundary of the FCC-BCC duplex region between the improved theoretical prediction and the experimental result. This indicates that other non-configurational entropy, such as magnetic entropy, may also contribute to the quantitative prediction of the compositional boundary of the FCC-BCC duplex region.

Moreover, the ordering effect in Al_xCoCrFeNi alloys has been investigated to validate the calculated configurational entropy. The LRO of the simulated atomic structure of Al_xCoCrFeNi alloys agrees well with experiments, which supported the developed scheme for entropy evaluation. Specifically, it has been found that the FCC CoCrFeNi alloy is a near-ideal solution, with a configurational entropy of 1.301 R. The discrepancy between the calculated value and the prediction of the ideal solution model (1.386 R) is a result of the formation of Co-Cr and Ni-Fe nearest neighboring pairs. It has also been found that Al addition enhanced the ordering effect in Al_xCoCrFeNi alloys. In FCC phase, SRO was enhanced by the enrichment of Ni around Al. In BCC phase, LRO was introduced by the formation of the Al-Ni enriched B2 phase and the Fe-Cr enriched BCC phase. The structure of the B2 phase was found to be that Al and Fe on one sublattice while Co and Ni on the other. This B2 phase not only lowered the configurational entropy but also reduced the lattice mismatch in Al_xCoCrFeNi alloys.

The two hypotheses mentioned in section 1.2 have been tested. It has been found that Al enhanced the atomic ordering effect by forming Al-Ni bonds in FCC phase and the B2 type ordering in BCC phase. These ordering effects reduced the configurational entropy of Al_xCoCrFeNi alloy in both FCC and BCC phase. Therefore, the hypothesis that *Al addition reduces the configurational entropy of Al_xCoCrFeNi alloys* is valid. It has also been found that the vibrational effect destabilized FCC phase and improved the prediction of the compositional boundary of the FCC-BCC duplex region in Al_xCoCrFeNi HEA system. This destabilization is mainly contributed by the vibrational enthalpy. Therefore, the hypothesis that *considering the atomic vibration effect will improve the prediction of the compositional boundary of the FCC-BCC duplex region in the* $Al_xCoCrFeNi$ *HEA system* is valid.

In the second case study, the vacancy migration in α-Al_2O_3 has been investigated using DFT calculations. It has been found that the migration energy of vacancies in α-Al_2O_3 has a strong dependence on the charge state of the vacancy. It has also been found that the observed charge-dependent vacancy migration energy is the result of the defect level shift during the migration and the different electron occupancies on the defect levels of the vacancies in different charge states. These findings for the first time build the link between the electronic structure and the vacancy migration energy. It suggests a novel route for engineering the diffusion kinetics by changing the charge state of vacancy or tuning the defect level shift during vacancy migration. Moreover, the calculations of Hf effect on Al vacancy diffusion in bulk and near $\Sigma 11$ grain boundary of α-Al_2O_3 show that Hf doping can tune the defect level shift, which slows down the Al vacancy diffusion in α-Al_2O_3. It provides a new perspective of the reactive element effect in α-Al_2O_3, that is, the reduced diffusivity of Al could be partially attributed to the modification in the defect levels of Al vacancy caused by reactive elements.

The two hypotheses mentioned in section 1.2 have also been tested. The results in Table 5.2 show that in most cases, the greater the charge of a vacancy, the lower its migration energy. However, there is one exception, *i.e.* the second segment of Al_2-Al_4 diffusive path. This is because that the vacancy migration energy is not only determined by the charge state of the vacancy but also determined by the defect level shift during the vacancy migration. Therefore, the hypothesis that *the greater the charge of a vacancy in* α-Al_2O_3*, the lower its migration energy* is invalid. However, the data points in Figure 5.8 show that the migration energy difference between two vacancies in different charge states increased as the defect level shift increased. Therefore, the second hypothesis that *the greater the defect level shift during the vacancy migration, the greater the difference in the migration energy between the vacancies in different charge states* is valid.

6.2 REMAINING PROBLEMS

Despite these findings, there are several problems remaining in this study which should be investigated in future works:

1. The configurational and vibrational free energy are treated separately in this study. One needs to bear in mind that the cross effect between these two free energies can be important. Because of the size mismatch between the atoms, the equilibrium position of each atom may not be exactly on the lattice site. This may lead to a reduction in configurational entropy for that the local strain of each atom is no longer the same. Thus, the configurational entropy may still be overestimated in this study. This cross effect needs to be investigated in future works.
2. The empirical potential used in this study is fitted to mostly the properties of binary alloys. Though tested on five ordered quaternary alloys, there are still many parameters in the potential that have not been fine tuned. Hence the interactions between the atoms in Al_xCoCrFeNi HEAs may not be described as accurately as in binary alloys. The interactions between Al and transition metals are qualitatively different from the interactions between transition metals. So the results related to the Al induced phase transition and atomic ordering should be reliable. But the SRO formed between transition metals needs further investigation.
3. Magnetic interactions between transition metals are not fully included in the framework of MEAM potential. Despite that they may not qualitatively change the general picture at high temperature such as 1373 K, their effect on the enthalpy and entropy of Al_xCoCrFeNi HEAs could quantitatively change the SRO and phase stability of this alloy system. Therefore, future works need to be done to incorporate the magnetic interactions, *e.g.* using micromagnetic model, into the computational scheme.
4. The Al induced phase transition in Al_xCoCrFeNi HEAs is treated as a two-phase equilibrium in this study. However, BCC phase is composed of the Ni-Al enriched B2 phase and the Fe-Cr enriched solid solution. Therefore, there should be a three-phase equilibrium

in the FCC-BCC duplex region. The phase equilibrium between FCC and B2 phase, FCC and BCC phase and B2 and BCC phase should be investigated in future works to provide a complete description of the phase transition in Al_xCoCrFeNi HEA system.

5. It has been found that the defect levels of Al vacancy is very close to the VBM. Therefore there are not much room left for them to shift during the vacancy migration. However, the self-interaction error in DFT calculations tends to underestimate the position of energy levels in the band gap. Therefore, the real position of the Al vacancy associated defect levels could be deeper in the band gap than what has been found in this study. So the migration energy difference between the Al vacancies in different charge states could be greater than the reported values. It is interesting to investigate the position of the Al vacancy associated defect levels and their shift during the vacancy migration by more accurate methods, *e.g.* quantum Monte Carlo method, which may provide better estimation of the migration energy difference.
6. The charged vacancy in the GB of alumina has not been directly simulated in this work. Because of the uncertainty in evaluating the position of the defect levels, the evaluated migration energy of V_{Al}^{3-} may not be reliable. The simulation of the charged system with periodic boundary conditions has been long a problem for computational materials science. Other DFT code with different implementations of charge correction, *e.g.* SeqQuest [1], should be tested and compared to VASP. New method for the calculation of charged systems may need to be developed.
7. Only vacancies have been considered in this study. However, interstitials can also play an important role in the atomic diffusion in metal oxides. Similar study should be conducted to investigate the formation and migration energy of interstitials in α-Al_2O_3. Combining the study of interstitials and vacancies will provide a complete picture of intrinsic point defects which is invaluable to the defect engineering in α-Al_2O_3.
8. The DFT results show that the diffusivity of vacancy in α-Al_2O_3 can be tuned by changing the charge state of vacancies. It is hard to be done in alumina due to the large band gap. However, this dependence of the migration energy on the charge state of a vacancy is not unique in α-Al_2O_3. It has been found in ZnO [18] and GaN [17] as well. Thus it

---

[1] http://dft.sandia.gov/Quest/

could be expected that this charge effect on vacancy migration energy can also exist in other metal oxides or even nitrides. It is interesting to check the charge dependence of the vacancy migration energy in the metal oxide which has a much narrower band gap. In these systems, changing the charge state of vacancy may be a promising way to tune the diffusivity of vacancies.

APPENDIX

MEAM POTENTIAL FOR Al-Co-Cr-Fe-Ni ALLOY SYSTEM

All the fitted parameters of the MEAM potential for Al-Co-Cr-Fe-Ni alloy are given in Table A1, A2 and A3. The comparison between MEAM and DFT predictions of the formation enthalpy and lattice parameters of AB ($L1_0$), AB_3 ($L1_2$) and A_3B ($L1_2$) phase are given in Table A4

Table A1: Parameters of the MEAM potentials for pure metals, *i.e.* the cohesive energy E^c (eV), the equilibrium NN distance r^e (Å), the decaying exponential factor of the universal energy α, the scaling factor of the embedded function A, four decaying exponential factors of the atomic charge density $\beta^{(i)}$, four weighting factors of the atomic charge density $t^{(i)}$ ($t^{(0)}$ is always 1), the screening parameters C_{min} (C_{max} is 2.80 for all element), and the scaling factor of the atomic charge density $\bar{\rho}^0$.

	Al	Co	Cr	Fe	Ni
E^c	3.353	4.410	4.100	4.290	4.450
r^e	2.864	2.500	2.495	2.480	2.490
α	4.640	5.120	5.820	5.067	4.990
A	1.040	1.050	0.420	0.560	1.100
$\beta^{(0)}$	2.040	2.100	6.810	4.150	2.450
$\beta^{(1)}$	1.500	0.000	1.000	1.000	1.500
$\beta^{(2)}$	6.000	1.000	1.000	1.000	6.000
$\beta^{(3)}$	1.500	6.000	1.000	1.000	1.500
$t^{(1)}$	4.000	9.000	0.300	2.600	5.790
$t^{(2)}$	-2.300	-1.000	5.900	1.800	1.600
$t^{(3)}$	8.010	-1.000	-10.400	-7.200	3.700
C_{min}	0.800	0.8000	0.780	0.360	0.800
$\bar{\rho}^0$	1.000	1.0000	1.000	1.1000	1.000

Table A2: Parameters of the MEAM cross potentials for element pairs, *i.e.* the cohesive energy E^c (eV), the equilibrium NN distance r^e (Å), the decaying exponential factor of the universal energy α, and the screening parameters C_{max} and C_{min}.

X	Al	Al	Al	Al	Co	Co	Co	Cr	Cr	Fe
Y	Co	Cr	Fe	Ni	Cr	Fe	Ni	Fe	Ni	Ni
E^c	4.485	3.762	4.152	4.566	4.075	4.404	4.273	3.997	4.011	4.297
r^e	2.471	2.630	2.496	2.525	2.465	2.462	2.495	2.448	2.508	2.465
α	4.000	5.000	4.280	4.600	5.950	5.370	5.000	5.370	5.160	5.000
C_{min}^{XYX}	1.680	1.800	1.000	1.550	1.800	1.800	1.210	1.000	1.200	1.600
C_{min}^{YXY}	1.630	2.330	2.000	1.360	2.000	1.800	1.420	1.000	0.000	1.170
C_{min}^{XXY}	1.780	1.810	2.000	1.940	1.900	2.000	1.590	0.000	0.800	1.800
C_{min}^{XYY}	1.900	0.200	0.600	1.380	0.700	2.000	1.620	0.000	1.900	1.110
C_{max}^{XYX}	3.530	4.200	2.000	3.590	3.800	3.800	3.510	4.200	4.000	4.000
C_{max}^{YXY}	3.300	4.060	4.000	3.270	4.000	3.800	3.560	4.200	2.000	2.500
C_{max}^{XXY}	4.100	4.140	4.000	4.000	3.900	4.000	4.140	5.000	2.800	4.000
C_{max}^{XYY}	4.210	3.300	2.800	3.460	2.800	4.000	4.150	5.200	3.800	2.470

Table A3: The screen parameters C_{max} and C_{min} of MEAM potential for ternary system.

X	Al	Al	Al	Al	Al	Al	Co	Co	Co	Cr
Y	Co	Co	Co	Cr	Cr	Fe	Cr	Cr	Fe	Fe
Z	Cr	Fe	Ni	Fe	Ni	Ni	Fe	Ni	Ni	Ni
C_{min}^{XYZ}	1.800	2.000	2.000	2.000	2.000	2.000	2.000	1.400	1.400	2.000
C_{min}^{XZY}	2.000	2.000	2.000	1.800	1.800	2.000	1.400	1.400	2.000	2.000
C_{min}^{YXZ}	2.000	2.000	1.400	2.000	2.000	1.400	2.000	2.000	2.000	2.000
C_{max}^{XYZ}	3.800	4.000	4.000	4.000	4.000	4.000	3.850	3.400	3.400	3.850
C_{max}^{XZY}	4.000	4.000	4.000	3.800	3.800	4.000	3.400	3.400	3.850	3.850
C_{max}^{YXZ}	4.000	4.000	3.400	4.000	4.000	3.400	3.850	3.850	4.000	4.000

Table A4: The MEAM and DFT predictions of formation enthalpy and lattice parameter of the ordered AB ($L1_0$), AB_3 ($L1_2$) and A_3B ($L1_2$) phase for all element pairs. The AB ($L1_0$) phase was enforced to be in cubic lattice so that only one lattice parameter is given.

A	B	AB ($L1_0$)		AB_3 ($L1_2$)		A_3B ($L1_2$)	
		Enthalpy of formation in eV/atom					
		MEAM	DFT	MEAM	DFT	MEAM	DFT
Al	Co	−0.322	−0.363	−0.182	−0.178	−0.244	−0.214
Al	Cr	0.007	0.065	0.077	0.175	−0.019	−0.102
Al	Fe	−0.247	−0.267	−0.329	−0.201	−0.079	−0.115
Al	Ni	−0.550	−0.516	−0.528	−0.432	−0.293	−0.214
Co	Cr	0.036	0.048	0.036	0.194	0.024	0.069
Co	Fe	0.097	0.048	0.091	0.140	0.033	0.015
Co	Ni	0.015	0.010	0.014	0.014	0.005	0.006
Cr	Fe	0.017	0.130	0.011	0.048	0.035	0.257
Cr	Ni	−0.001	0.093	−0.008	−0.003	0.003	0.155
Fe	Ni	−0.095	−0.071	−0.183	−0.097	0.060	0.042
		Lattice parameter in Å					
		MEAM	DFT	MEAM	DFT	MEAM	DFT
Al	Co	3.551	3.642	3.492	3.577	3.773	3.794
Al	Cr	3.761	3.773	3.767	3.665	3.858	3.898
Al	Fe	3.661	3.694	3.619	3.652	3.822	3.802
Al	Ni	3.657	3.664	3.609	3.571	3.785	3.846
Co	Cr	3.547	3.510	3.605	3.556	3.524	3.478
Co	Fe	3.460	3.569	3.491	3.488	3.490	3.548
Co	Ni	3.533	3.522	3.526	3.524	3.541	3.522
Cr	Fe	3.543	3.529	3.552	3.565	3.581	3.652
Cr	Ni	3.637	3.534	3.591	3.555	3.682	3.564
Fe	Ni	3.553	3.576	3.578	3.556	3.517	3.575

BIBLIOGRAPHY

[1] B.S. Murty, J.W. Yeh, and S. Ranganathan. *High-Entropy Alloys*. Elsevier Science, 2014.

[2] J.-W. Yeh, S.-K. Chen, S.-J. Lin, J.-Y. Gan, T.-S. Chin, T.-T. Shun, C.-H. Tsau, and S.-Y. Chang. Nanostructured high-entropy alloys with multiple principal elements: Novel alloy design concepts and outcomes. *Advanced Engineering Materials*, 6(5):299–303, 2004.

[3] F. Otto, Y. Yang, H. Bei, and E.P. George. Relative effects of enthalpy and entropy on the phase stability of equiatomic high-entropy alloys. *Acta Materialia*, 61(7):2628 – 2638, 2013.

[4] Arthur H. Heuer, David B. Hovis, James L. Smialek, and Brian Gleeson. Alumina scale formation: A new perspective. *Journal of the American Ceramic Society*, 94:s146–s153, 2011.

[5] N. D. M. Hine, K. Frensch, W. M. C. Foulkes, and M. W. Finnis. Supercell size scaling of density functional theory formation energies of charged defects. *Phys. Rev. B*, 79:024112, Jan 2009.

[6] Patrick W. M. Jacobs and Eugene A. Kotomin. Modeling of point defets in corundum crystals. *Journal of the American Ceramic Society*, 77(10):2505–2508, 1994.

[7] U. Aschauer, P. Bowen, and S.C. Parker. Oxygen vacancy diffusion in alumina: New atomistic simulation methods applied to an old problem. *Acta Materialia*, 57(16):4765–4772, 2009.

[8] A.H. Heuer. Oxygen and aluminum diffusion in α-Al_2O_3: How much do we really understand? *Journal of the European Ceramic Society*, 28(7):1495 – 1507, 2008.

[9] M. S. Lucas, G. B. Wilks, L. Mauger, J. A. Muoz, O. N. Senkov, E. Michel, J. Horwath, S. L. Semiatin, M. B. Stone, D. L. Abernathy, and E. Karapetrova. Absence of long-range chemical ordering in equimolar FeCoCrNi. *Applied Physics Letters*, 100(25):251907, 2012.

[10] Yih-Farn Kao, Ting-Jie Chen, Swe-Kai Chen, and Jien-Wei Yeh. Microstructure and mechanical property of as-cast, -homogenized, and -deformed $Al_xCoCrFeNi$ ($0 \leq x \leq 2$) high-entropy alloys. *Journal of Alloys and Compounds*, 488(1):57–64, 2009.

[11] Woei-Ren Wang, Wei-Lin Wang, and Jien-Wei Yeh. Phases, microstructure and mechanical properties of $Al_xCoCrFeNi$ high-entropy alloys at elevated temperatures. *Journal of Alloys and Compounds*, 589:143–152, 2014.

[12] Fuyang Tian, Lorand Delczeg, Nanxian Chen, Lajos Karoly Varga, Jiang Shen, and Levente Vitos. Structural stability of $NiCoFeCrAl_x$ high-entropy alloy from ab initio theory. *Phys. Rev. B*, 88:085128, Aug 2013.

[13] Chuan Zhang, Fan Zhang, Shuanglin Chen, and Weisheng Cao. Computational thermodynamics aided high-entropy alloy design. *JOM*, 64(7):839–845, 2012.

[14] Zhi Tang, Oleg N. Senkov, Chuan Zhang, Fan Zhang, Carl D. Lundin, and Peter K. Liaw. Al-Co-Cr-Fe-Ni Phase Equilibria and Properties. In *TMS 2015 Supplemental Proceedings*. Wiley, 2015.

[15] Pasquale Pavone, Stefano Baroni, and Stefano de Gironcoli. $\alpha \leftrightarrow \beta$ phase transition in tin: A theoretical study based on density-functional perturbation theory. *Phys. Rev. B*, 57:10421–10423, May 1998.

[16] Jürgen Neuhaus, Michael Leitner, Karl Nicolaus, Winfried Petry, Bernard Hennion, and Arno Hiess. Role of vibrational entropy in the stabilization of the high-temperature phases of iron. *Phys. Rev. B*, 89:184302, May 2014.

[17] M. G. Ganchenkova and R. M. Nieminen. Nitrogen vacancies as major point defects in gallium nitride. *Phys. Rev. Lett.*, 96:196402, May 2006.

[18] Paul Erhart and Karsten Albe. Diffusion of zinc vacancies and interstitials in zinc oxide. *Applied Physics Letters*, 88(20):201918, 2006.

[19] Christoph Freysoldt, Blazej Grabowski, Tilmann Hickel, Jörg Neugebauer, Georg Kresse, Anderson Janotti, and Chris G. Van de Walle. First-principles calculations for point defects in solids. *Rev. Mod. Phys.*, 86:253–305, Mar 2014.

[20] F Bassani, G Iadonisi, and B Preziosi. Electronic impurity levels in semiconductors. *Reports on Progress in Physics*, 37(9):1099, 1974.

[21] Sokrates T. Pantelides. The electronic structure of impurities and other point defects in semiconductors. *Rev. Mod. Phys.*, 50:797–858, Oct 1978.

[22] C. Li, J.C. Li, M. Zhao, and Q. Jiang. Effect of aluminum contents on microstructure and properties of $Al_xCoCrFeNi$ alloys. *Journal of Alloys and Compounds*, 504, Supplement 1:S515–S518, 2010.

[23] Chun-Ming Lin and Hsien-Lung Tsai. Evolution of microstructure, hardness, and corrosion properties of high-entropy $Al_{0.5}$CoCrFeNi alloy. *Intermetallics*, 19(3):288–294, 2011.

[24] Woei-Ren Wang, Wei-Lin Wang, Shang-Chih Wang, Yi-Chia Tsai, Chun-Hui Lai, and Jien-Wei Yeh. Effects of al addition on the microstructure and mechanical property of Al_xCoCrFeNi high-entropy alloys. *Intermetallics*, 26:44–51, 2012.

[25] Zhi Tang, Michael C. Gao, Haoyan Diao, Tengfei Yang, Junpeng Liu, Tingting Zuo, Yong Zhang, Zhaoping Lu, Yongqiang Cheng, Yanwen Zhang, Karin A. Dahmen, Peter K. Liaw, and Takeshi Egami. Aluminum alloying effects on lattice types, microstructures, and mechanical behavior of high-entropy alloys systems. *JOM*, 65(12):1848–1858, 2013.

[26] A. van de Walle and G. Ceder. First-principles computation of the vibrational entropy of ordered and disordered Pd_3V. *Phys. Rev. B*, 61:5972–5978, Mar 2000.

[27] Yi Wang and Yunfeng Sun. First-principles thermodynamic calculations for δ-Pu and ε-Pu. *Journal of Physics: Condensed Matter*, 12(21):L311, 2000.

[28] Sven P. Rudin, M. D. Jones, and R. C. Albers. Thermal stabilization of the hcp phase in titanium. *Phys. Rev. B*, 69:094117, Mar 2004.

[29] L. Anthony, J. K. Okamoto, and B. Fultz. Vibrational entropy of ordered and disordered Ni_3Al. *Phys. Rev. Lett.*, 70:1128–1130, Feb 1993.

[30] X. Yang and Y. Zhang. Prediction of high-entropy stabilized solid-solution in multi-component alloys. *Materials Chemistry and Physics*, 132(23):233 – 238, 2012.

[31] Sheng Guo, Qiang Hu, Chun Ng, and C.T. Liu. More than entropy in high-entropy alloys: Forming solid solutions or amorphous phase. *Intermetallics*, 41:96 – 103, 2013.

[32] H. W. Sheng, W. K. Luo, F. M. Alamgir, J. M. Bai, and E. Ma. Atomic packing and short-to-medium-range order in metallic glasses. *Nature*, 439:419–425, 2006.

[33] W. K. Luo, H. W. Sheng, F. M. Alamgir, J. M. Bai, J. H. He, and E. Ma. Icosahedral short-range order in amorphous alloys. *Phys. Rev. Lett.*, 92:145502, Apr 2004.

[34] S. M. Dubiel and J. Cieslak. Short-range order in iron-rich Fe-Cr alloys as revealed by Mössbauer spectroscopy. *Phys. Rev. B*, 83:180202, May 2011.

[35] H. L. Hong, Q. Wang, C. Dong, and Peter K. Liaw. Understanding the Cu-Zn brass alloys using a short-range-order cluster model: significance of specific compositions of industrial alloys. *Sci. Rep.*, 4:7065, 2014.

[36] Y.F. Ye, Q. Wang, J. Lu, C.T. Liu, and Y. Yang. The generalized thermodynamic rule for phase selection in multicomponent alloys. *Intermetallics*, 59:75–80, 2015.

[37] Louis J. Santodonato, Yang Zhang, Mikhail Feygenson, Chad M. Parish, Michael C. Gao, Richard J.K. Weber, Joerg C Neuefeind, Zhi Tang, and Peter K Liaw. Deviation from high-entropy configurations in the atomic distributions of a multi-principal-element alloy. *Nat Commun*, 6:5964, 2013.

[38] W. Jones and N.H. March. *Theoretical Solid State Physics: Perfect lattices in equilibrium.* Dover Books on Physics Series. Dover Publications, 1973.

[39] H. Peng, C.L. Wang, J.C. Li, H.C. Wang, Y. Sun, and Q. Zheng. Elastic and vibrational properties of $Mg_2Si_{1-x}Sn_x$ alloy from first principles calculations. *Solid State Communications*, 152(9):821–824, 2012.

[40] Olle Eriksson, J. M. Wills, and Duane Wallace. Electronic, quasiharmonic, and anharmonic entropies of transition metals. *Phys. Rev. B*, 46:5221–5228, Sep 1992.

[41] P. Souvatzis and S. P. Rudin. Dynamical stabilization of cubic ZrO_2 by phonon-phonon interactions: *Ab initio* calculations. *Phys. Rev. B*, 78:184304, Nov 2008.

[42] Dario Alfè. Phon: A program to calculate phonons using the small displacement method. *Computer Physics Communications*, 180(12):2622–2633, 2009.

[43] D. Alfè, G. D. Price, and M. J. Gillan. Thermodynamics of hexagonal-close-packed iron under earth's core conditions. *Phys. Rev. B*, 64:045123, Jul 2001.

[44] R Oriani and W.K Murphy. Thermodynamics of ordering alloys-IV heats of formation of some alloys of transition metals. *Acta Metallurgica*, 10(9):879–885, 1962.

[45] A. V. Ruban, P. A. Korzhavyi, and B. Johansson. First-principles theory of magnetically driven anomalous ordering in bcc Fe-Cr alloys. *Phys. Rev. B*, 77:094436, Mar 2008.

[46] Zhenyu Liu, Yinkai Lei, Corinne Gray, and Guofeng Wang. Examination of solid-solution phase formation rules for high entropy alloys from atomistic monte carlo simulations. *JOM*, 67(10):2364–2374, 2015.

[47] Wei Guo, Wojciech Dmowski, Ji-Yong Noh, Philip Rack, Peter K. Liaw, and Takeshi Egami. Local atomic structure of a high-entropy alloy: An X-ray and neutron scattering study. *Metallurgical and Materials Transactions A*, 44(5):1994–1997, 2013.

[48] Akihiko Hirata, Pengfei Guan, Takeshi Fujita, Yoshihiko Hirotsu, Akihisa Inoue, Alain Reza Yavari, Toshio Sakurai, and Mingwei Chen. Direct observation of local atomic order in a metallic glass. *Nat Mater*, 10:28–33, 2011.

[49] M M J Treacy, J M Gibson, L Fan, D J Paterson, and I McNulty. Fluctuation microscopy: a probe of medium range order. *Reports on Progress in Physics*, 68(12):2899, 2005.

[50] C. G. Shull and Sidney Siegel. Neutron diffraction studies of order-disorder in alloys. *Phys. Rev.*, 75:1008–1010, Apr 1949.

[51] H. Okamoto, D.J. Chakrabarti, D.E. Laughlin, and T.B. Massalski. The Au-Cu (gold-copper) system. *Journal of Phase Equilibria*, 8(5):454–474, 1987.

[52] H. Okamoto. Al–Ni (aluminum-nickel). *Journal of Phase Equilibria*, 14(2):257–259, 1993.

[53] P. Nash and M.F. Singleton. The Ni–Pt (nickel-platinum) system. *Bulletin of Alloy Phase Diagrams*, 10(3):258–262, 1989.

[54] Brian A. Welk, Robert E.A. Williams, Gopal B. Viswanathan, Mark A. Gibson, Peter K. Liaw, and Hamish L. Fraser. Nature of the interfaces between the constituent phases in the high entropy alloy CoCrCuFeNiAl. *Ultramicroscopy*, 134:193–199, 2013.

[55] N. Mattern, U. Khn, H. Hermann, H. Ehrenberg, J. Neuefeind, and J. Eckert. Short-range order of $Zr_{62-x}Ti_xAl_10Cu_20Ni_8$ bulk metallic glasses. *Acta Materialia*, 50(2):305–314, 2002.

[56] N. A. Mauro, V. Wessels, J. C. Bendert, S. Klein, A. K. Gangopadhyay, M. J. Kramer, S. G. Hao, G. E. Rustan, A. Kreyssig, A. I. Goldman, and K. F. Kelton. Short- and medium-range order in $Zr_{80}Pt_{20}$ liquids. *Phys. Rev. B*, 83:184109, May 2011.

[57] W. Hoyer and R. Jdicke. Short-range and medium-range order in liquid Au–Ge alloys. *Journal of Non-Crystalline Solids*, 192193:102–105, 1995. Structure of Non-Crystalline Materials 6.

[58] S.C. Middleburgh, D.M. King, G.R. Lumpkin, M. Cortie, and L. Edwards. Segregation and migration of species in the CrCoFeNi high entropy alloy. *Journal of Alloys and Compounds*, 599:179–182, 2014.

[59] C. Niu, A. J. Zaddach, A. A. Oni, X. Sang, J. W. Hurt, J. M. LeBeau, C. C. Koch, and D. L. Irving. Spin-driven ordering of Cr in the equiatomic high entropy alloy NiFeCrCo. *Applied Physics Letters*, 106(16):161906, 2015.

[60] S. R. Elliott. Medium-range structural order in covalent amorphous solids. *Nature*, 354:445–452, 1991.

[61] Joongoo Kang, Junyi Zhu, Su-Huai Wei, Eric Schwegler, and Yong-Hyun Kim. Persistent medium-range order and anomalous liquid properties of $Al_{1\text{-}x}Cu_x$ alloys. *Phys. Rev. Lett.*, 108:115901, Mar 2012.

[62] Li Wang, Yuqing Wang, Chuanxiao Peng, and Yanning Zhang. Medium-range structural order in liquid Ni_20Al_80 alloy: Experimental and molecular dynamics studies. *Physics Letters A*, 350(56):405 – 409, 2006.

[63] UR Kattner and BP Burton. Al–Fe (aluminum-iron). *Phase Diagrams of Binary Iron Alloys*, pages 12–28, 1993.

[64] A.J. McAlister. The Al–Co (aluminum-cobalt) system. *Bulletin of Alloy Phase Diagrams*, 10(6):646–650, 1989.

[65] Y. Oishi and W. D. Kingery. Self-diffusion of oxygen in single crystal and polycrystalline aluminum oxide. *The Journal of Chemical Physics*, 33(2), 1960.

[66] A. E. Paladino and W. D. Kingery. Aluminum ion diffusion in aluminum oxide. *The Journal of Chemical Physics*, 37(5), 1962.

[67] DAVID J. REED and B. J. WUENSCH. Ion-probe measurement of oxygen self-diffusion in single-crystal Al_2O_3. *Journal of the American Ceramic Society*, 63(1-2):88–92, 1980.

[68] M. Le Gall, B. Lesage, and J. Bernardini. Self-diffusion in α-Al_2O_3 i. aluminium diffusion in single crystals. *Philosophical Magazine A*, 70(5):761–773, 1994.

[69] D. Clemens, K. Bongartz, W.J. Quadakkers, H. Nickel, H. Holzbrecher, and J.-S. Becker. Determination of lattice and grain boundary diffusion coefficients in protective alumina scales on high temperature alloys using SEM, TEM and SIMS. *Fresenius Journal of Analytical Chemistry*, 353(3-4):267–270, 1995.

[70] D. Prot and C. Monty. Self-diffusion in α-Al_2O_3. ii. oxygen diffusion in undoped single crystals. *Philosophical Magazine A*, 73(4):899–917, 1996.

[71] A.H. Heuer and K.P.D. Lagerlof. Oxygen self-diffusion in corundum (α-Al_2O_3): A conundrum. *Philosophical Magazine Letters*, 79(8):619–627, 1999.

[72] Tsubasa NAKAGAWA, Atsutomo NAKAMURA, Isao SAKAGUCHI, Naoya SHIBATA, K. Peter. D. LAGERLOF, Takahisa YAMAMOTO, Hajime HANEDA, and Yuichi IKUHARA. Oxygen pipe diffusion in sapphire basal dislocation. *Journal of the Ceramic Society of Japan*, 114(1335):1013–1017, 2006.

[73] Tsubasa Nakagawa, Isao Sakaguchi, Naoya Shibata, Katsuyuki Matsunaga, Teruyasu Mizoguchi, Takahisa Yamamoto, Hajime Haneda, and Yuichi Ikuhara. Yttrium doping effect on oxygen grain boundary diffusion in α-Al_2O_3. *Acta Materialia*, 55(19):6627–6633, 2007.

[74] P. Fielitz, G. Borchardt, S. Ganschow, R. Bertram, and A. Markwitz. ^{26}Al tracer diffusion in titanium doped single crystalline α-Al_2O_3. *Solid State Ionics*, 179(1112):373–379, 2008.

[75] Tsubasa Nakagawa, Hitoshi Nishimura, Isao Sakaguchi, Naoya Shibata, Katsuyuki Matsunaga, Takahisa Yamamoto, and Yuichi Ikuhara. Grain boundary character dependence of oxygen grain boundary diffusion in α-Al_2O_3 bicrystals. *Scripta Materialia*, 65(6):544–547, 2011.

[76] J. H. Harding and D. J. Harris. Simulation of grain-boundary diffusion in ceramics by kinetic Monte Carlo. *Phys. Rev. B*, 63:094102, Jan 2001.

[77] J. Carrasco, N. Lopez, and F. Illas. First principles analysis of the stability and diffusion of oxygen vacancies in metal oxides. *Phys. Rev. Lett.*, 93:225502, Nov 2004.

[78] Ivan Milas, Berit Hinnemann, and Emily A. Carter. Diffusion of Al, O, Pt, Hf, and y atoms on α-Al_2O_3(0001): implications for the role of alloying elements in thermal barrier coatings. *J. Mater. Chem.*, 21:1447–1456, 2011.

[79] R. Prescott and M.J. Graham. The formation of aluminum oxide scales on high-temperature alloys. *Oxidation of Metals*, 38(3-4):233–254, 1992.

[80] Moon Young Yang, Katsumasa Kamiya, Blanka Magyari-Kpe, Masaaki Niwa, Yoshio Nishi, and Kenji Shiraishi. Charge-dependent oxygen vacancy diffusion in Al_2O_3-based resistive-random-access-memories. *Applied Physics Letters*, 103(9):–, 2013.

[81] Jerry B. Torrance, Philippe Lacorre, Chinnarong Asavaroengchai, and Robert M. Metzger. Why are some oxides metallic, while most are insulating? *Physica C: Superconductivity*, 182(46):351 – 364, 1991.

[82] M Landmann, E Rauls, and W G Schmidt. The electronic structure and optical response of rutile, anatase and brookite TiO_2. *Journal of Physics: Condensed Matter*, 24(19):195503, 2012.

[83] T.V. Perevalov, A.V. Shaposhnikov, V.A. Gritsenko, H. Wong, J.H. Han, and C.W. Kim. Electronic structure of α-Al_2O_3: Ab initio simulations and comparison with experiment. *JETP Letters*, 85(3):165–168, 2007.

[84] M. Vernica Ganduglia-Pirovano, Alexander Hofmann, and Joachim Sauer. Oxygen vacancies in transition metal and rare earth oxides: Current state of understanding and remaining challenges. *Surface Science Reports*, 62(6):219 – 270, 2007.

[85] Ulrike Diebold. The surface science of titanium dioxide. *Surface Science Reports*, 48(58):53 – 229, 2003.

[86] S Lettieri, L Santamaria Amato, P Maddalena, E Comini, C Baratto, and S Todros. Recombination dynamics of deep defect states in zinc oxide nanowires. *Nanotechnology*, 20(17):175706, 2009.

[87] Anderson Janotti and Chris G Van de Walle. Fundamentals of zinc oxide as a semiconductor. *Reports on Progress in Physics*, 72(12):126501, 2009.

[88] W. M. C. Foulkes, L. Mitas, R. J. Needs, and G. Rajagopal. Quantum monte carlo simulations of solids. *Rev. Mod. Phys.*, 73:33–83, Jan 2001.

[89] Jens K. Norskov, Frank Abild-Pedersen, Felix Studt, and Thomas Bligaard. Density functional theory in surface chemistry and catalysis. *Proceedings of the National Academy of Sciences*, 108(3):937–943, 2011.

[90] R. Devanathan, L.R. Corrales, W.J. Weber, A. Chartier, and C. Meis. Molecular dynamics simulation of defect production in collision cascades in zircon. *Nuclear Instruments and Methods in Physics Research Section B: Beam Interactions with Materials and Atoms*, 228(14):299–303, 2005.

[91] L. Van Brutzel, M. Rarivomanantsoa, and D. Ghaleb. Displacement cascade initiated with the realistic energy of the recoil nucleus in UO_2 matrix by molecular dynamics simulation. *Journal of Nuclear Materials*, 354(13):28 – 35, 2006.

[92] P. Hohenberg and W. Kohn. Inhomogeneous electron gas. *Phys. Rev.*, 136:B864–B871, Nov 1964.

[93] W. Kohn and L. J. Sham. Self-consistent equations including exchange and correlation effects. *Phys. Rev.*, 140:A1133–A1138, Nov 1965.

[94] Charlotte Froese Fischer. General hartree-fock program. *Computer Physics Communications*, 43(3):355 – 365, 1987.

[95] Stefano Curtarolo, Wahyu Setyawan, Shidong Wang, Junkai Xue, Kesong Yang, Richard H. Taylor, Lance J. Nelson, Gus L.W. Hart, Stefano Sanvito, Marco Buongiorno-Nardelli, Natalio Mingo, and Ohad Levy. Aflowlib.org: A distributed materials properties repository from high-throughput ab initio calculations. *Computational Materials Science*, 58:227 – 235, 2012.

[96] Yinkai Lei, Huijun Liu, and Wei Xiao. First principles study of the size effect of TiO_2 anatase nanoparticles in dye-sensitized solar cell. *Modelling and Simulation in Materials Science and Engineering*, 18(2):025004, 2010.

[97] Hongyan Lv, Yinkai Lei, Aditi Datta, and Guofeng Wang. Influence of surface segregation on magnetic properties of FePt nanoparticles. *Applied Physics Letters*, 103(13):132405, 2013.

[98] M. I. Baskes. Modified embedded-atom potentials for cubic materials and impurities. *Phys. Rev. B*, 46:2727–2742, Aug 1992.

[99] Adri C. T. van Duin, Siddharth Dasgupta, Francois Lorant, and William A. Goddard III. Reaxff: a reactive force field for hydrocarbons. *The Journal of Physical Chemistry A*, 105(41):9396–9409, 2001.

[100] D. Frenkel and B. Smit. *Understanding Molecular Simulation: From Algorithms to Applications*. Computational science series. Elsevier Science, 2001.

[101] Jakob Schiøtz and Karsten W. Jacobsen. A maximum in the strength of nanocrystalline copper. *Science*, 301(5638):1357–1359, 2003.

[102] Jonathan Schäfer and Karsten Albe. Influence of solutes on the competition between mesoscopic grain boundary sliding and coupled grain boundary motion. *Scripta Materialia*, 66(5):315–317, 2012.

[103] T. Frolov and Y. Mishin. Molecular dynamics modeling of self-diffusion along a triple junction. *Phys. Rev. B*, 79:174110, May 2009.

[104] V. Yamakov, D. Wolf, S.R. Phillpot, and H. Gleiter. Grain-boundary diffusion creep in nanocrystalline palladium by molecular-dynamics simulation. *Acta Materialia*, 50(1):61–73, 2002.

[105] David E. Shaw, Paul Maragakis, Kresten Lindorff-Larsen, Stefano Piana, Ron O. Dror, Michael P. Eastwood, Joseph A. Bank, John M. Jumper, John K. Salmon, Yibing Shan, and Willy Wriggers. Atomic-level characterization of the structural dynamics of proteins. *Science*, 330(6002):341–346, 2010.

[106] Kresten Lindorff-Larsen, Stefano Piana, Ron O. Dror, and David E. Shaw. How fast-folding proteins fold. *Science*, 334(6055):517–520, 2011.

[107] D.P. Landau and K. Binder. *A Guide to Monte Carlo Simulations in Statistical Physics*. Cambridge University Press, 2009.

[108] Nicholas Metropolis, Arianna W. Rosenbluth, Marshall N. Rosenbluth, Augusta H. Teller, and Edward Teller. Equation of state calculations by fast computing machines. *The Journal of Chemical Physics*, 21(6), 1953.

[109] Fugao Wang and D. P. Landau. Efficient, multiple-range random walk algorithm to calculate the density of states. *Phys. Rev. Lett.*, 86:2050–2053, Mar 2001.

[110] Daan Frenkel and Anthony J. C. Ladd. New Monte Carlo method to compute the free energy of arbitrary solids. application to the fcc and hcp phases of hard spheres. *The Journal of Chemical Physics*, 81(7):3188–3193, 1984.

[111] Zhiyao Duan, Jun Zhong, and Guofeng Wang. Modeling surface segregation phenomena in the (111) surface of ordered Pt_3Ti crystal. *The Journal of Chemical Physics*, 133(11):114701, 2010.

[112] A van de Walle and M Asta. Self-driven lattice-model Monte Carlo simulations of alloy thermodynamic properties and phase diagrams. *Modelling and Simulation in Materials Science and Engineering*, 10(5):521, 2002.

[113] Sivakumar R. Challa, David S. Sholl, and J. Karl Johnson. Adsorption and separation of hydrogen isotopes in carbon nanotubes: Multicomponent grand canonical Monte Carlo simulations. *The Journal of Chemical Physics*, 116(2), 2002.

[114] Byeong-Joo Lee and M. I. Baskes. Second nearest-neighbor modified embedded-atom-method potential. *Phys. Rev. B*, 62:8564–8567, Oct 2000.

[115] M. de Koning and A. Antonelli. Einstein crystal as a reference system in free energy estimation using adiabatic switching. *Phys. Rev. E*, 53:465–474, Jan 1996.

[116] James H. Rose, John R. Smith, Francisco Guinea, and John Ferrante. Universal features of the equation of state of metals. *Phys. Rev. B*, 29:2963–2969, Mar 1984.

[117] Byeong-Joo Lee, M.I. Baskes, Hanchul Kim, and Yang Koo Cho. Second nearest-neighbor modified embedded atom method potentials for bcc transition metals. *Phys. Rev. B*, 64:184102, Oct 2001.

[118] M.I. Baskes. Determination of modified embedded atom method parameters for nickel. *Materials Chemistry and Physics*, 50(2):152 – 158, 1997.

[119] M I Baskes and R A Johnson. Modified embedded atom potentials for hcp metals. *Modelling and Simulation in Materials Science and Engineering*, 2(1):147, 1994.

[120] B. Jelinek, S. Groh, M. F. Horstemeyer, J. Houze, S. G. Kim, G. J. Wagner, A. Moitra, and M. I. Baskes. Modified embedded atom method potential for Al, Si, Mg, Cu, and Fe alloys. *Phys. Rev. B*, 85:245102, Jun 2012.

[121] G. Kresse and J. Hafner. *Ab initio* molecular dynamics for liquid metals. *Phys. Rev. B*, 47:558–561, Jan 1993.

[122] G. Kresse and J. Furthmüller. Efficient iterative schemes for *ab initio* total-energy calculations using a plane-wave basis set. *Phys. Rev. B*, 54:11169–11186, Oct 1996.

[123] G. Kresse and D. Joubert. From ultrasoft pseudopotentials to the projector augmented-wave method. *Phys. Rev. B*, 59:1758–1775, Jan 1999.

[124] John P. Perdew, Kieron Burke, and Matthias Ernzerhof. Generalized gradient approximation made simple. *Phys. Rev. Lett.*, 77:3865–3868, Oct 1996.

[125] Hendrik J. Monkhorst and James D. Pack. Special points for brillouin-zone integrations. *Phys. Rev. B*, 13:5188–5192, Jun 1976.

[126] Charles Kittel. *Introduction to Solid State Physics.* John Wiley & Sons, Inc., New York, 6th edition, 1986.

[127] R.M. Martin. *Electronic Structure: Basic Theory and Practical Methods.* Cambridge University Press, 2004.

[128] D. R. Hamann, M. Schlüter, and C. Chiang. Norm-conserving pseudopotentials. *Phys. Rev. Lett.*, 43:1494–1497, Nov 1979.

[129] D. R. Hamann. Generalized norm-conserving pseudopotentials. *Phys. Rev. B*, 40:2980–2987, Aug 1989.

[130] David Vanderbilt. Soft self-consistent pseudopotentials in a generalized eigenvalue formalism. *Phys. Rev. B*, 41:7892–7895, Apr 1990.

[131] Kari Laasonen, Roberto Car, Changyol Lee, and David Vanderbilt. Implementation of ultrasoft pseudopotentials in *ab initio* molecular dynamics. *Phys. Rev. B*, 43:6796–6799, Mar 1991.

[132] Kari Laasonen, Alfredo Pasquarello, Roberto Car, Changyol Lee, and David Vanderbilt. Car-parrinello molecular dynamics with vanderbilt ultrasoft pseudopotentials. *Phys. Rev. B*, 47:10142–10153, Apr 1993.

[133] P. E. Blöchl. Projector augmented-wave method. *Phys. Rev. B*, 50:17953–17979, Dec 1994.

[134] G. Kresse and D. Joubert. From ultrasoft pseudopotentials to the projector augmented-wave method. *Phys. Rev. B*, 59:1758–1775, Jan 1999.

[135] G Kresse and J Hafner. Norm-conserving and ultrasoft pseudopotentials for first-row and transition elements. *Journal of Physics: Condensed Matter*, 6(40):8245, 1994.

[136] J. P. Perdew and Alex Zunger. Self-interaction correction to density-functional approximations for many-electron systems. *Phys. Rev. B*, 23:5048–5079, May 1981.

[137] W. Kohn. Nobel lecture: Electronic structure of matter–wave functions and density functionals. *Rev. Mod. Phys.*, 71:1253–1266, Oct 1999.

[138] A. D. Becke. Density-functional exchange-energy approximation with correct asymptotic behavior. *Phys. Rev. A*, 38:3098–3100, Sep 1988.

[139] Chengteh Lee, Weitao Yang, and Robert G. Parr. Development of the Colle–Salvetti correlation-energy formula into a functional of the electron density. *Phys. Rev. B*, 37:785–789, Jan 1988.

[140] John P. Perdew, J. A. Chevary, S. H. Vosko, Koblar A. Jackson, Mark R. Pederson, D. J. Singh, and Carlos Fiolhais. Atoms, molecules, solids, and surfaces: Applications of the generalized gradient approximation for exchange and correlation. *Phys. Rev. B*, 46:6671–6687, Sep 1992.

[141] Jörg Neugebauer and Tilmann Hickel. Density functional theory in materials science. *Wiley Interdisciplinary Reviews: Computational Molecular Science*, 3(5):438–448, 2013.

[142] Paula Mori-Sánchez, Aron J. Cohen, and Weitao Yang. Localization and delocalization errors in density functional theory and implications for band-gap prediction. *Phys. Rev. Lett.*, 100:146401, Apr 2008.

[143] Ilaria Ciofini, Carlo Adamo, and Henry Chermette. Self-interaction error in density functional theory: a mean-field correction for molecules and large systems. *Chemical Physics*, 309(1):67 – 76, 2005. Electronic Structure Calculations for Understanding Surfaces and Molecules. In Honor of Notker Roesch.

[144] John P. Perdew, Matthias Ernzerhof, and Kieron Burke. Rationale for mixing exact exchange with density functional approximations. *The Journal of Chemical Physics*, 105(22), 1996.

[145] Jochen Heyd, Gustavo E. Scuseria, and Matthias Ernzerhof. Hybrid functionals based on a screened coulomb potential. *The Journal of Chemical Physics*, 118(18), 2003.

[146] C. Franchini, R. Podloucky, J. Paier, M. Marsman, and G. Kresse. Ground-state properties of multivalent manganese oxides: Density functional and hybrid density functional calculations. *Phys. Rev. B*, 75:195128, May 2007.

[147] G. Makov and M. C. Payne. Periodic boundary conditions in ab initio calculations. *Phys. Rev. B*, 51:4014–4022, Feb 1995.

[148] Jörg Neugebauer and Matthias Scheffler. Adsorbate-substrate and adsorbate-adsorbate interactions of Na and K adlayers on Al(111). *Phys. Rev. B*, 46:16067–16080, Dec 1992.

[149] Seinosuke Onari, Toshihiro Arai, and Keiei Kudo. Infrared lattice vibrations and dielectric dispersion in α-Fe_2O_3. *Phys. Rev. B*, 16:1717–1721, Aug 1977.

[150] M.W. Finnis, A.Y. Lozovoi, and A. Alavi. The oxidation of NiAl: What can we learn from ab initio calculations? *Annual Review of Materials Research*, 35(1):167–207, 2005.

[151] R. C. Weast, M. J. Astle, and W. H. Beyer, editors. *CRC Handbook of Chemistry and Physics*. CRC Press, Inc., 69th edition, 1988-1989.

[152] Graeme Henkelman, Blas P. Uberuaga, and Hannes Jonsson. A climbing image nudged elastic band method for finding saddle points and minimum energy paths. *The Journal of Chemical Physics*, 113(22), 2000.

[153] R.R. Hultgren. *Selected values of thermodynamic properties of metals and alloys*. Wiley series on the science and technology of materials. Wiley, 1963.

[154] H. Okamoto. Al–Cr (aluminum-chromium). *Journal of Phase Equilibria and Diffusion*, 29(1):112–113, 2008.

[155] J. C. Boettger. High-precision, all-electron, full-potential calculation of the equation of state and elastic constants of corundum. *Phys. Rev. B*, 55:750–756, Jan 1997.

[156] H. d'Amour, D. Schiferl, W. Denner, Heinz Schulz, and W. B. Holzapfel. Highpressure singlecrystal structure determinations for ruby up to 90 kbar using an automatic diffractometer. *Journal of Applied Physics*, 49(8), 1978.

[157] A.H. Heuer, T. Nakagawa, M.Z. Azar, D.B. Hovis, J.L. Smialek, B. Gleeson, N.D.M. Hine, H. Guhl, H.-S. Lee, P. Tangney, W.M.C. Foulkes, and M.W. Finnis. On the growth of Al_2O_3 scales. *Acta Materialia*, 61(18):6670 – 6683, 2013.

[158] Roger H. French. Electronic band structure of Al_2O_3, with comparison to Alon and AIN. *Journal of the American Ceramic Society*, 73(3):477–489, 1990.

[159] E.T. Arakawa and M.W. Williams. Optical properties of aluminum oxide in the vacuum ultraviolet. *Journal of Physics and Chemistry of Solids*, 29(5):735 – 744, 1968.

[160] J. Olivier and R. Poirier. Electronic structure of Al_2O_3 from electron energy loss spectroscopy. *Surface Science*, 105(1):347 – 356, 1981.

[161] Daniel T. Gillespie. Stochastic simulation of chemical kinetics. *Annual Review of Physical Chemistry*, 58(1):35–55, 2007.

[162] K.J.W. Atkinson, Robin W. Grimes, Mark R. Levy, Zoe L. Coull, and Tim English. Accommodation of impurities in α-Al_2O_3, α-Cr_2O_3 and α-Fe_2O_3. *Journal of the European Ceramic Society*, 23(16):3059–3070, 2003.

[163] Thomas Höche, Philip R. Kenway, Hans-Joachim Kleebe, Michael W. Finnis, and Manfred Rhle. The structure of special grain boundaries in α-Al_2O_3. *Journal of Physics and Chemistry of Solids*, 55(10):1067–1082, 1994.

[164] Philip R. Kenway. Calculated structures and energies of grain boundaries in α-Al_2O_3. *Journal of the American Ceramic Society*, 77(2):349–355, 1994.

[165] I. Milas, B. Hinnermann, and E. A. Carter. Structure of and ion segregation to an alumina grain boundary: Implications for growth and creep. *Journal of Materials Research*, 23(5):1494–1508, 2008.